Electronic supporting information for:

Single and double deprotonation/dearomatization of N,S-donor pyridinophane ligand in ruthenium complexes

Hoan Minh Dinh,[a] Tatiana Gridneva,[a] Ayumu Karimata,[a] Alèria Garcia-Roca,[a] Jiratheep Pruchyathamkorn,[a] Pradnya H. Patil,[a] Andrey Petrov,[a] Abir Sarbajna,[a] Sébastien Lapointe,[a] Eugene Khaskin,[a] Robert R. Fayzullin,[b] and Julia R. Khusnutdinova*[a]

Table of Contents

1. Characterization of Ru complexes

$[Ru(N_2S_2)(MeCN)_2](OTf)_2$, 1

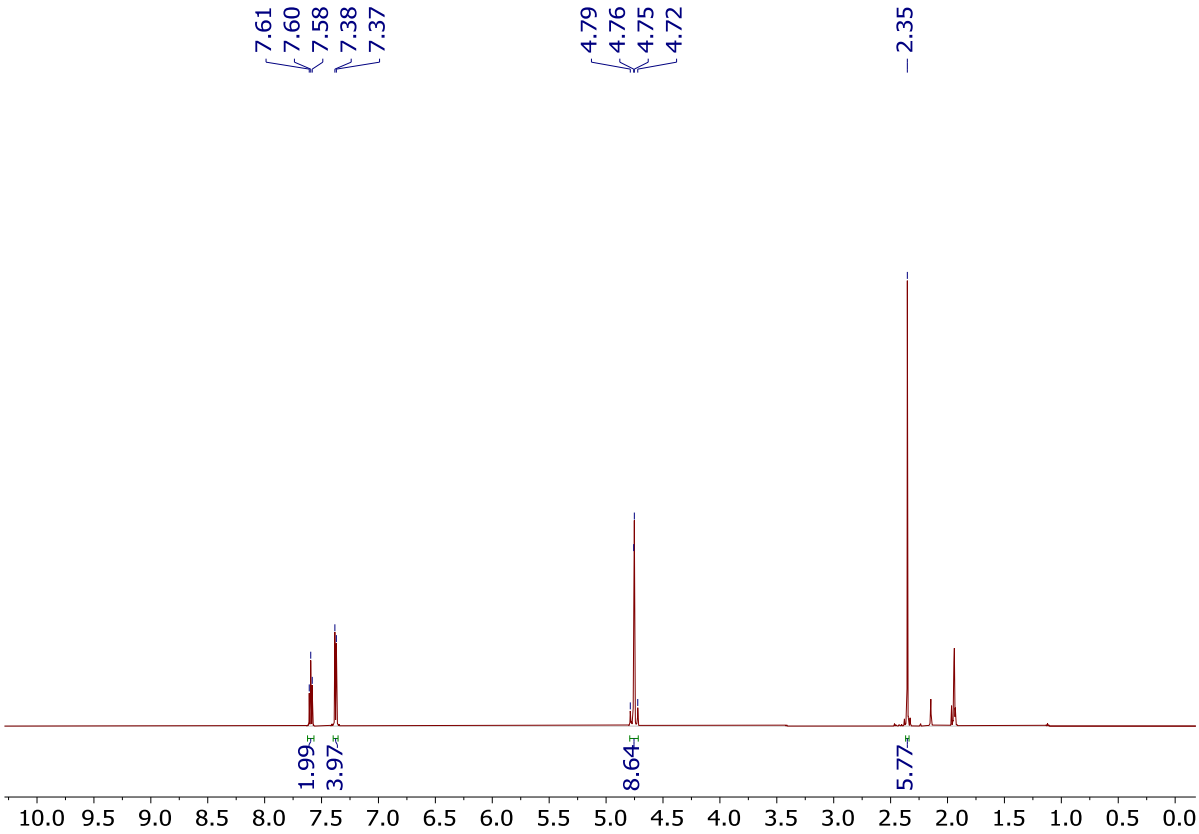

Figure S1. ^{1}H NMR spectrum of complex **1** in CD_3CN at 23 °C.

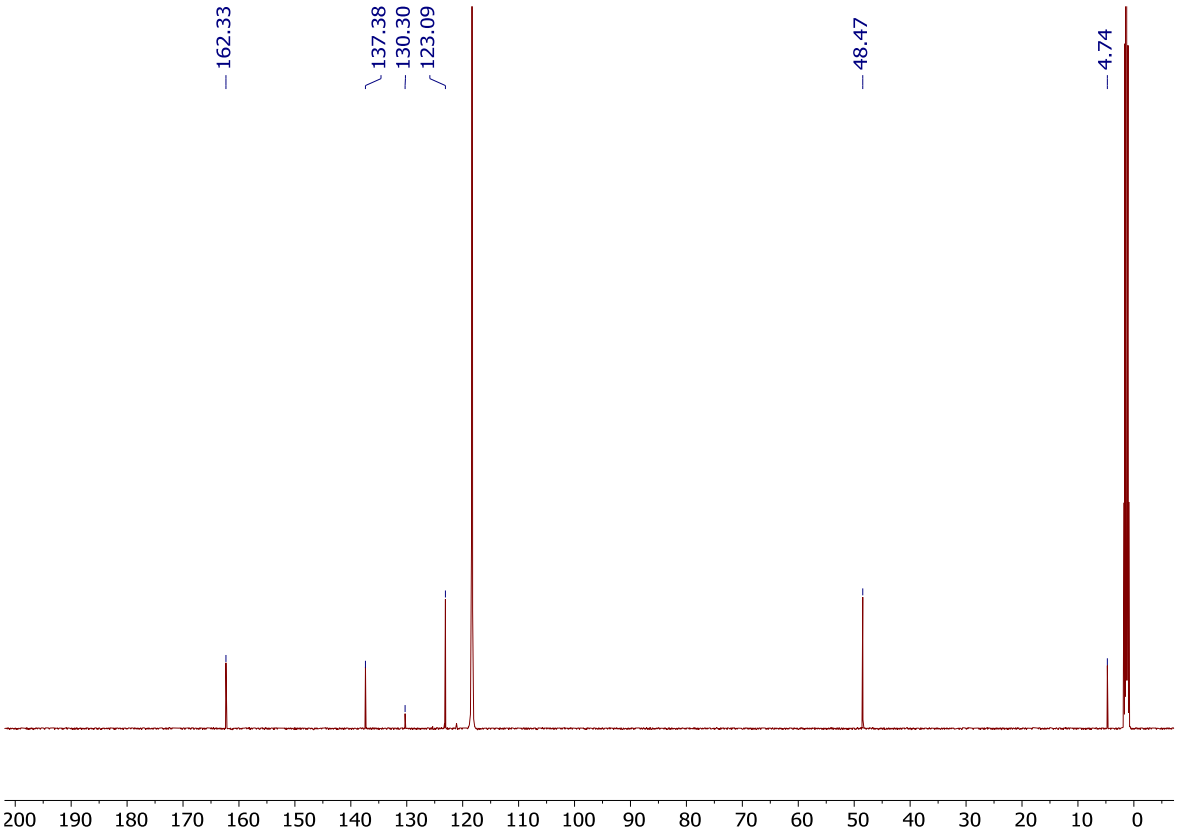

Figure S2. $^{13}C\{^{1}H\}$ NMR spectrum of complex **1** in CD_3CN at 23 °C.

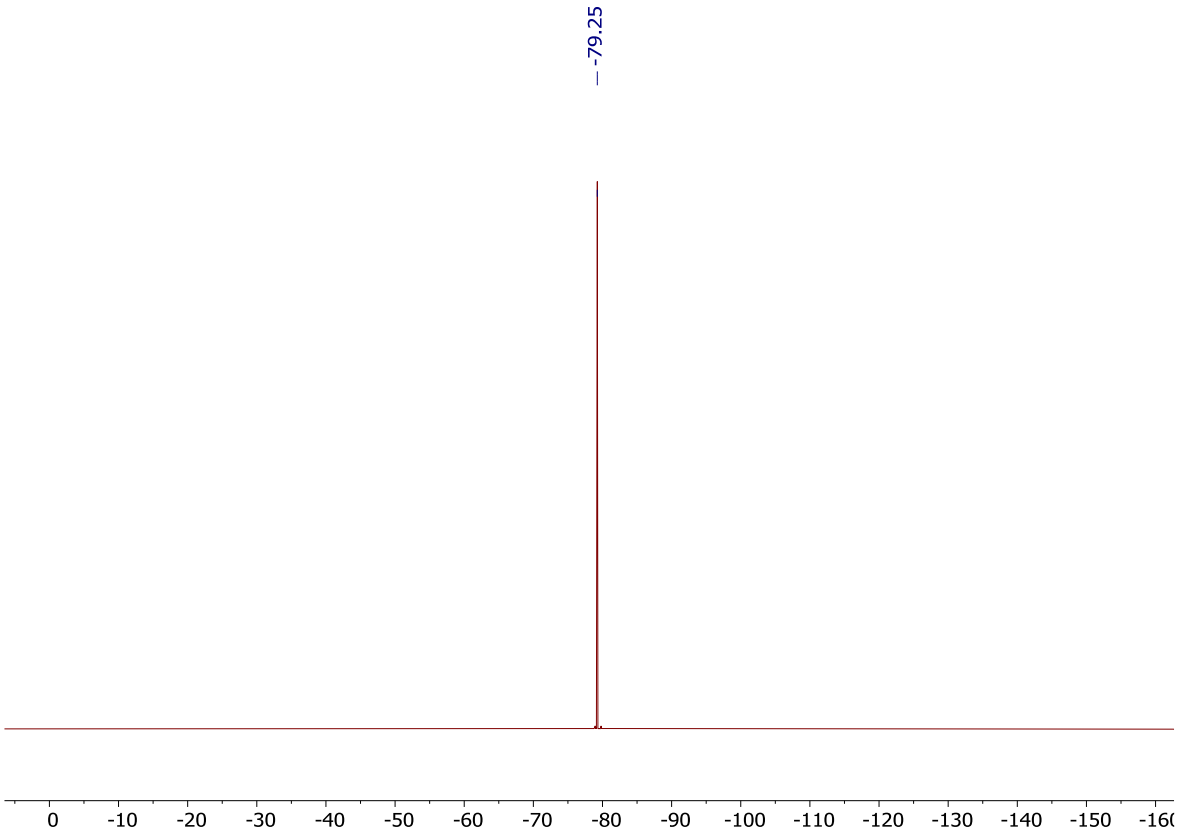

Figure S3. ^{19}F NMR spectrum of complex **1** in CD_3CN at 23 °C.

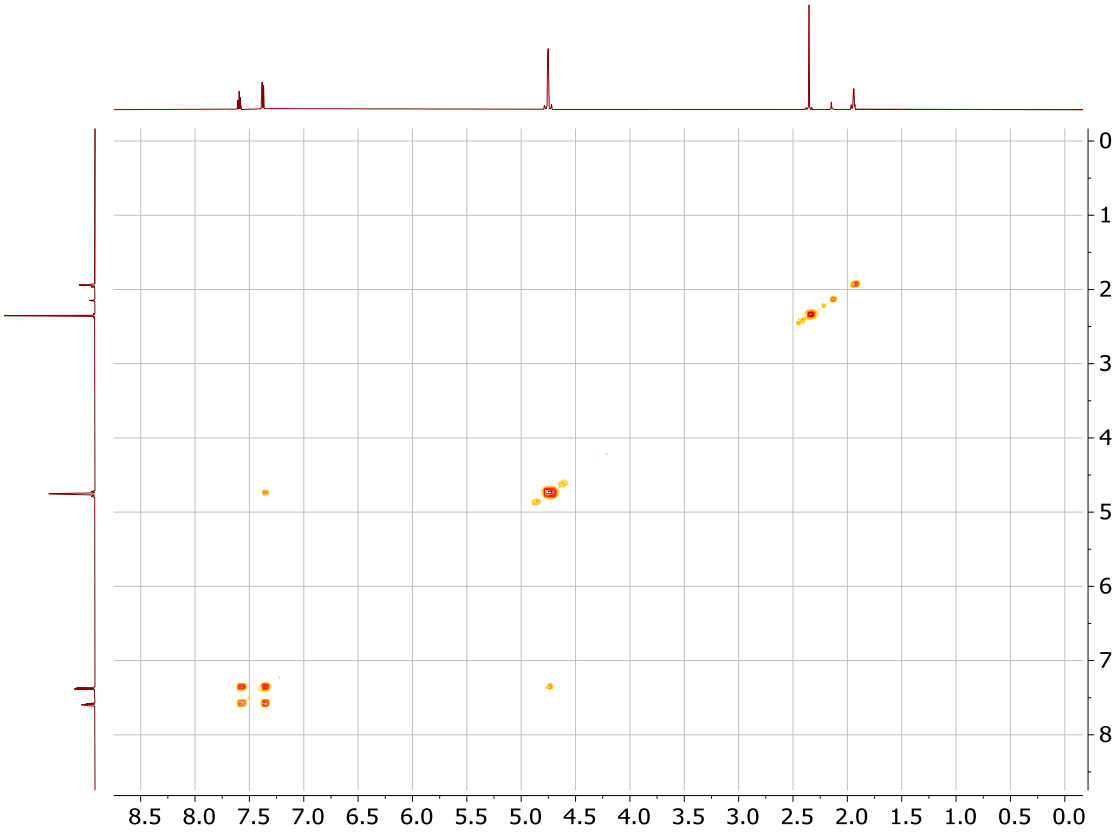

Figure S4. ^{1}H-^{1}H COSY spectrum of **1** in CD_3CN at 23 °C.

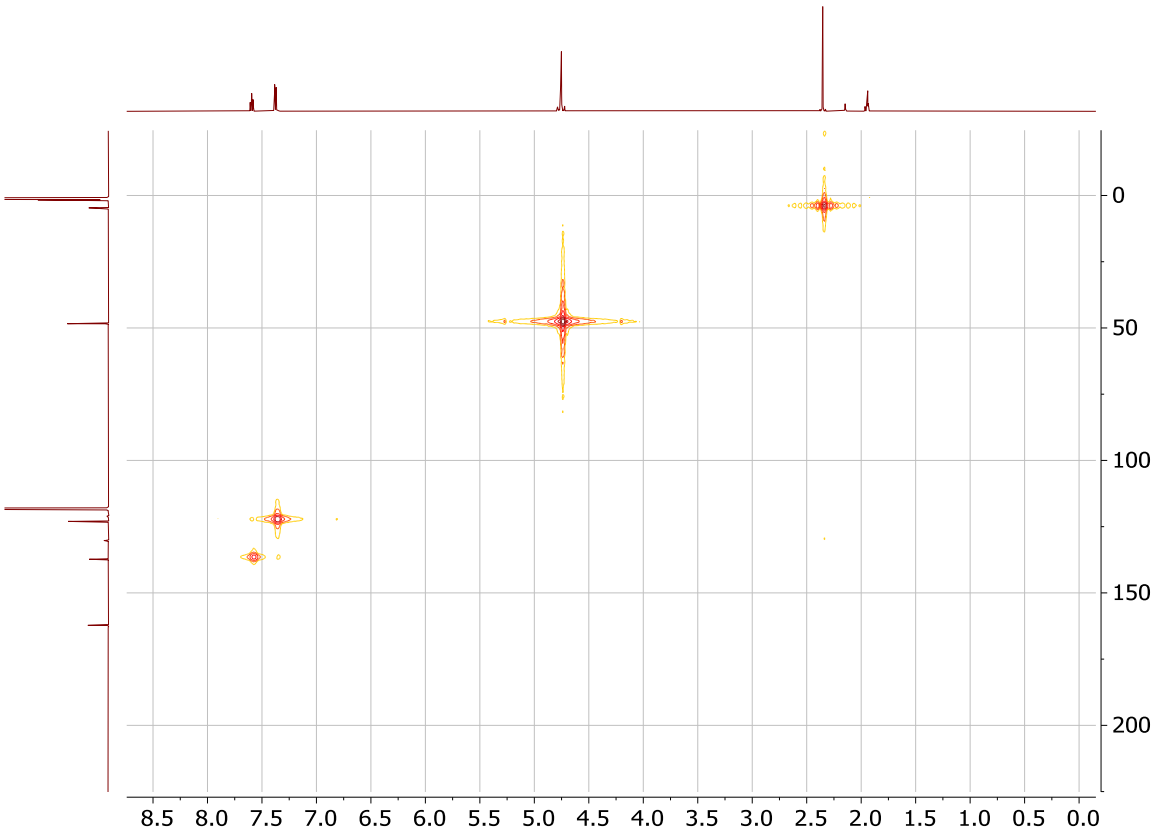

Figure S5: ^{1}H-^{13}C HMQC spectrum of **1** in CD_3CN at 23 °C.

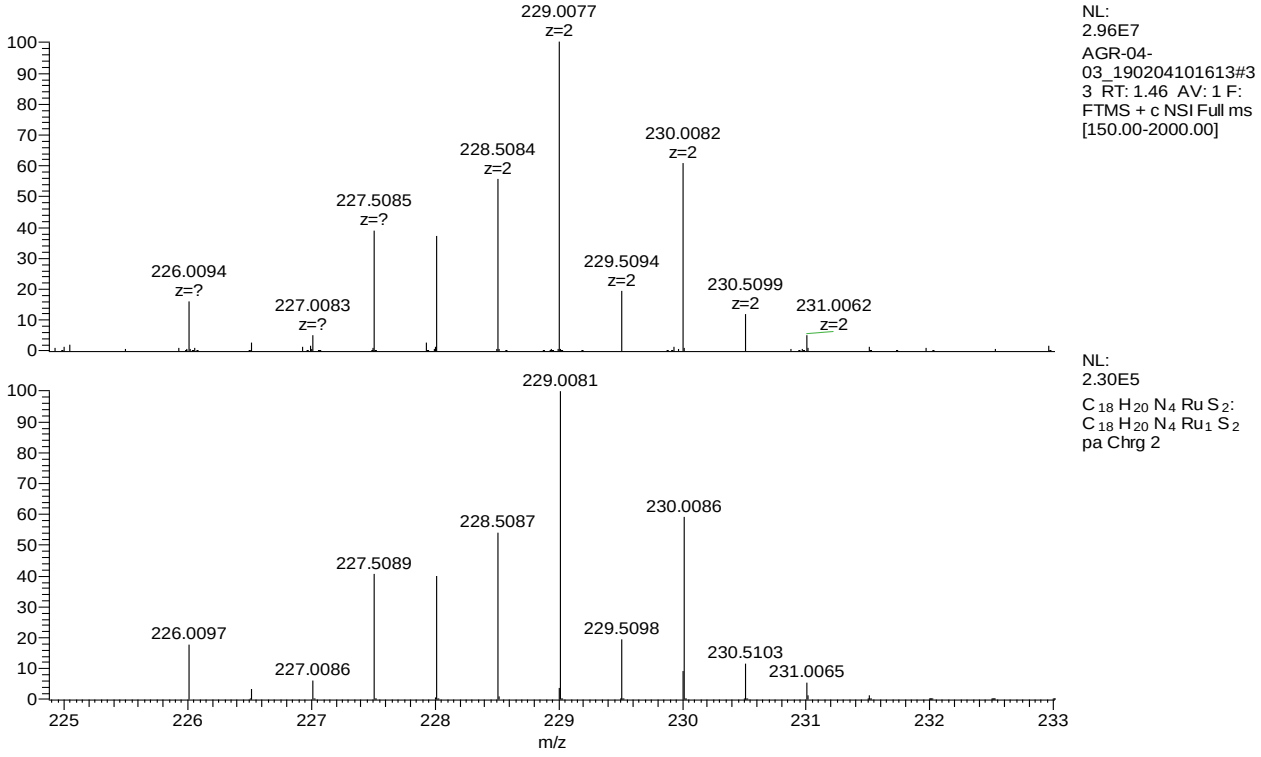

Figure S6. ESI-(HR)MS spectrum of **1** (top) and simulated spectrum of $C_{18}H_{20}N_4RuS_2^{2+}$: (bottom).

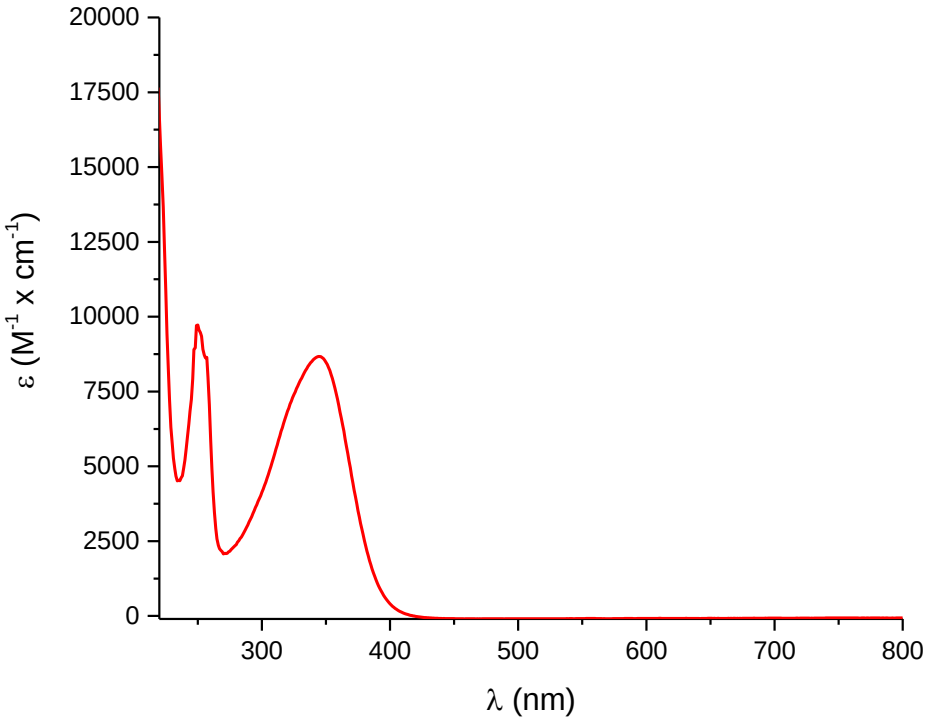

Figure S7. UV-vis absorbance spectrum of **1** in acetonitrile.

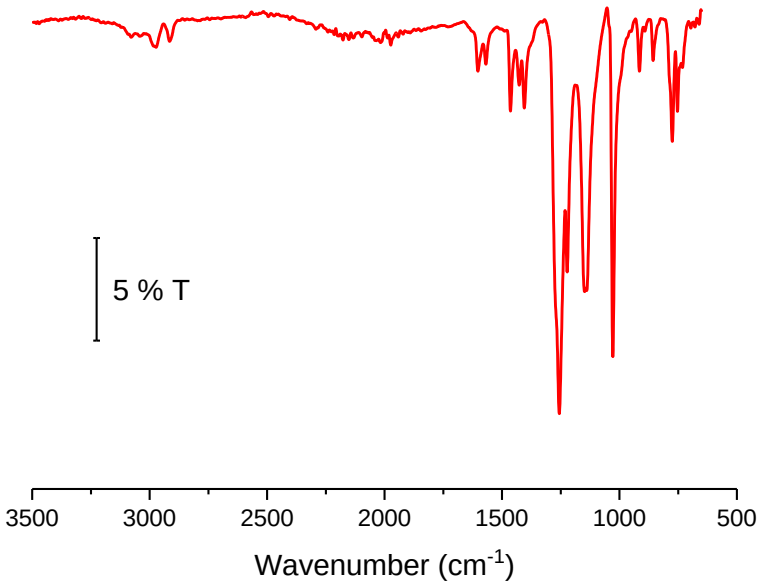

Figure S8. ATR FT-IR transmittance spectrum of **1**.

[Ru(N$_2$S$_2$)(PPh$_3$)Cl]Cl, 2

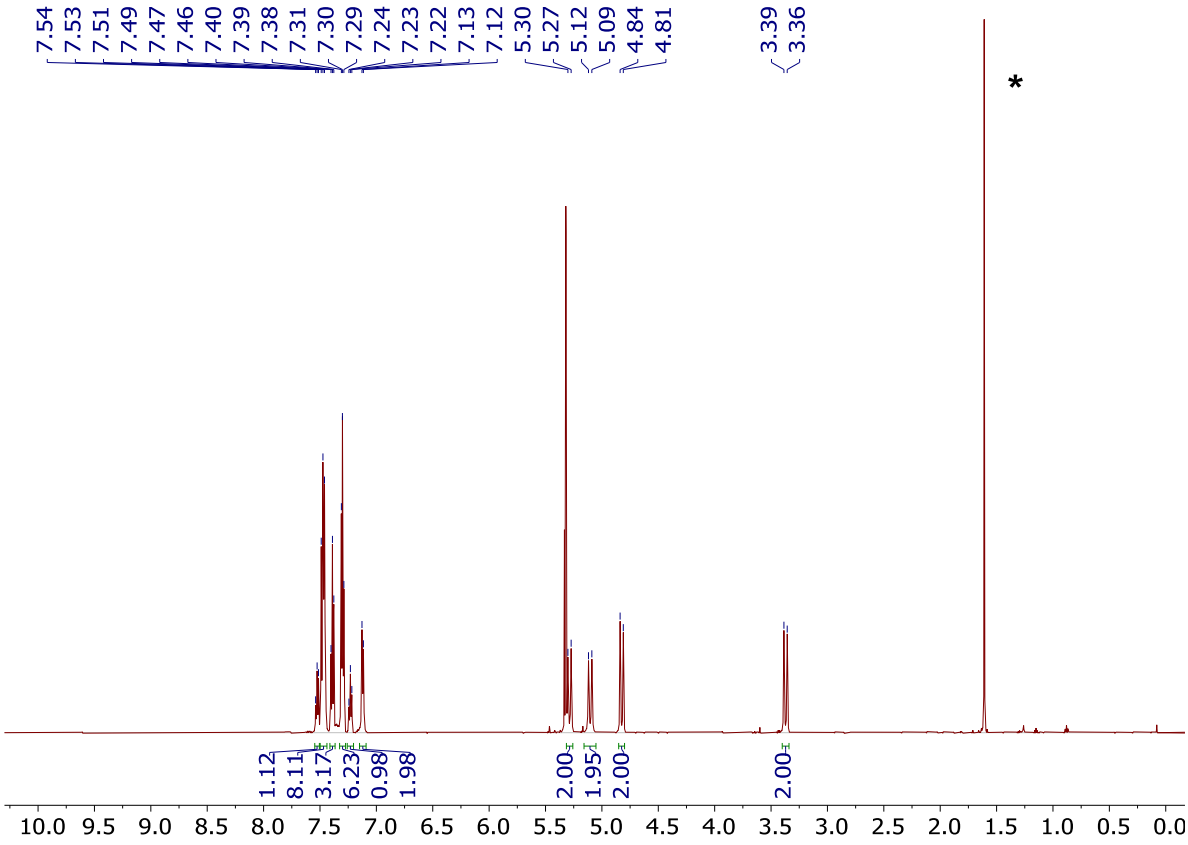

Figure S9. ^{1}H NMR spectrum of complex **2** in CD_2Cl_2 at 23 °C. Peak of residual water is marked with an asterisk.

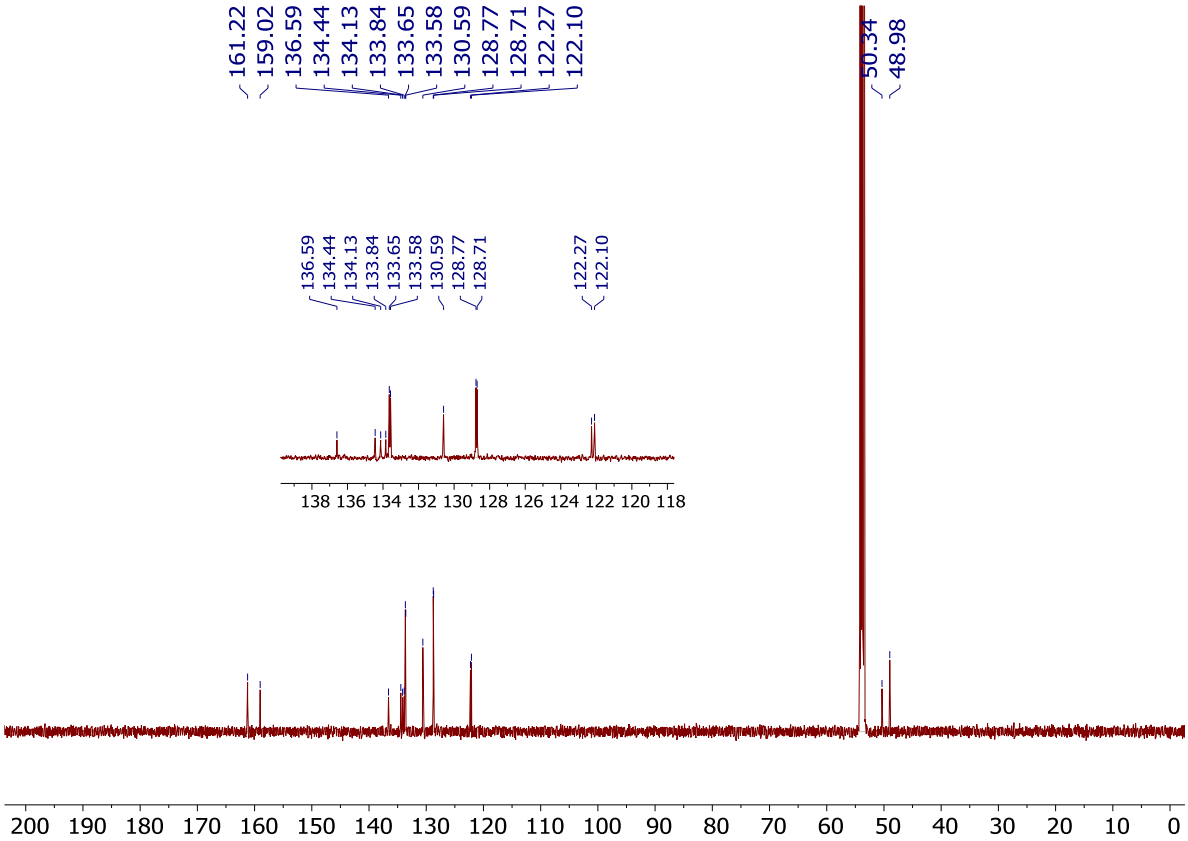

Figure S10. ^{13}C{^{1}H} NMR spectrum of complex **2** in CD_2Cl_2 at 23 °C.

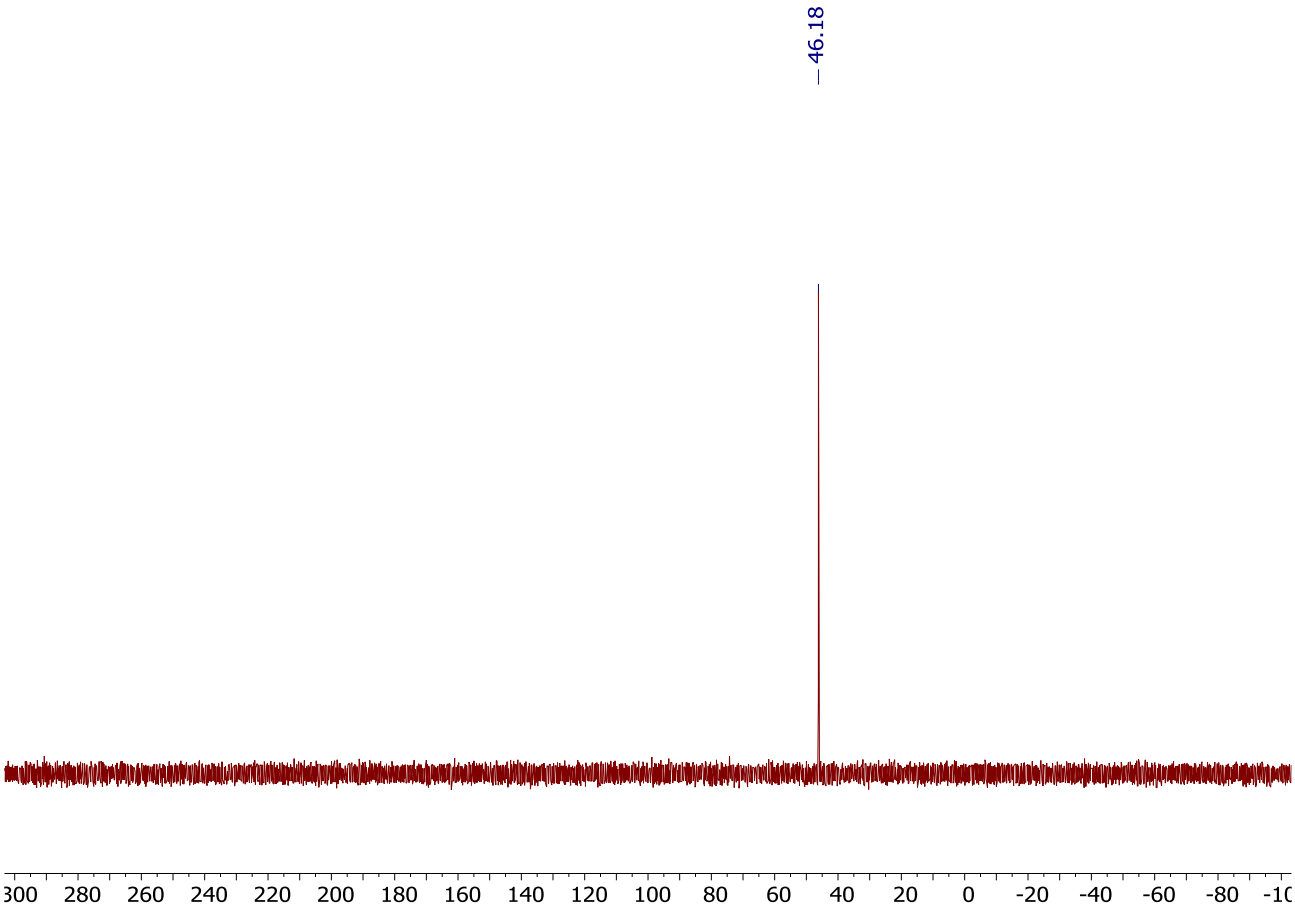

Figure S11. $^{31}P\{^{1}H\}$ NMR spectrum of complex **2** in CD_2Cl_2 at 23 °C.

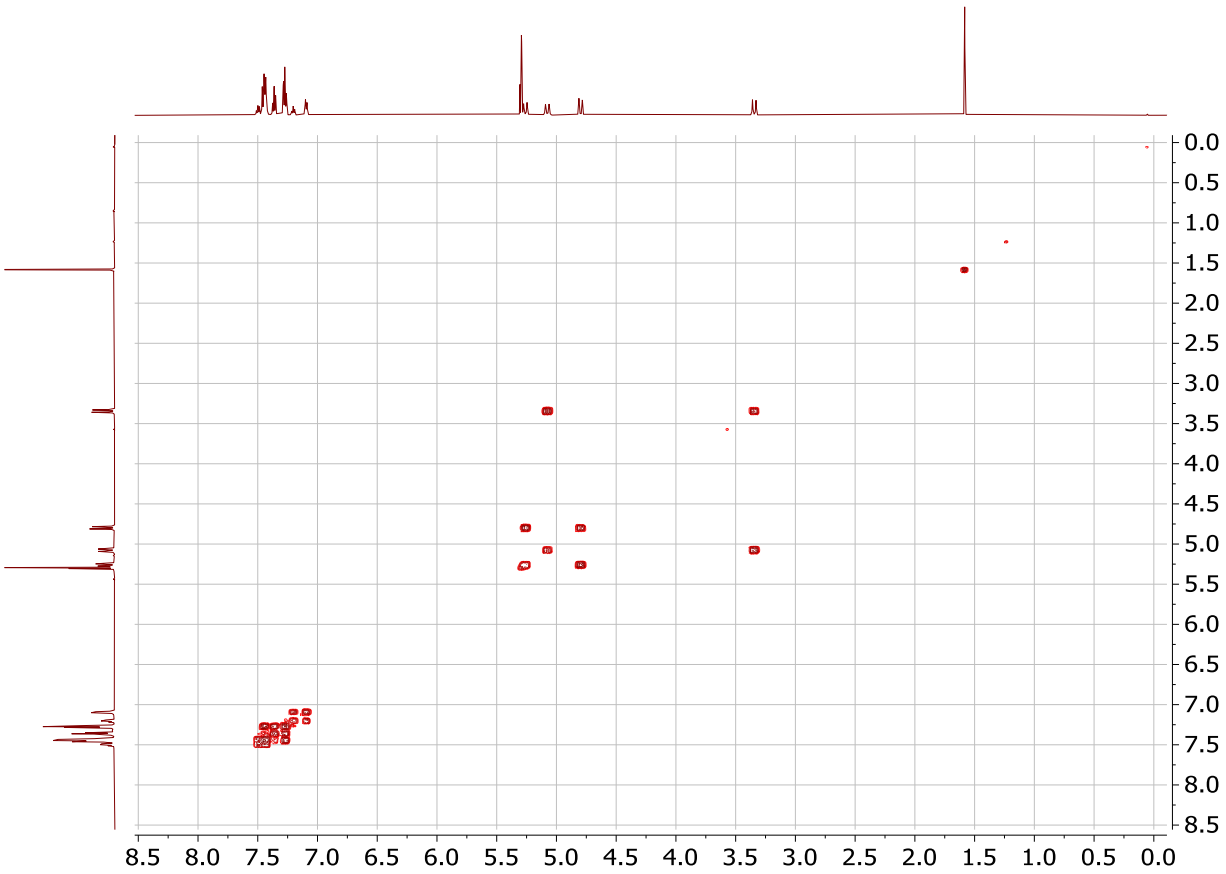

Figure S12. ^{1}H-^{1}H COSY spectrum of **2** in CD_2Cl_2 at 23 °C.

Figure S13. ^{1}H-^{13}C HMQC spectrum of **2** in CD_2Cl_2 at 23 °C.

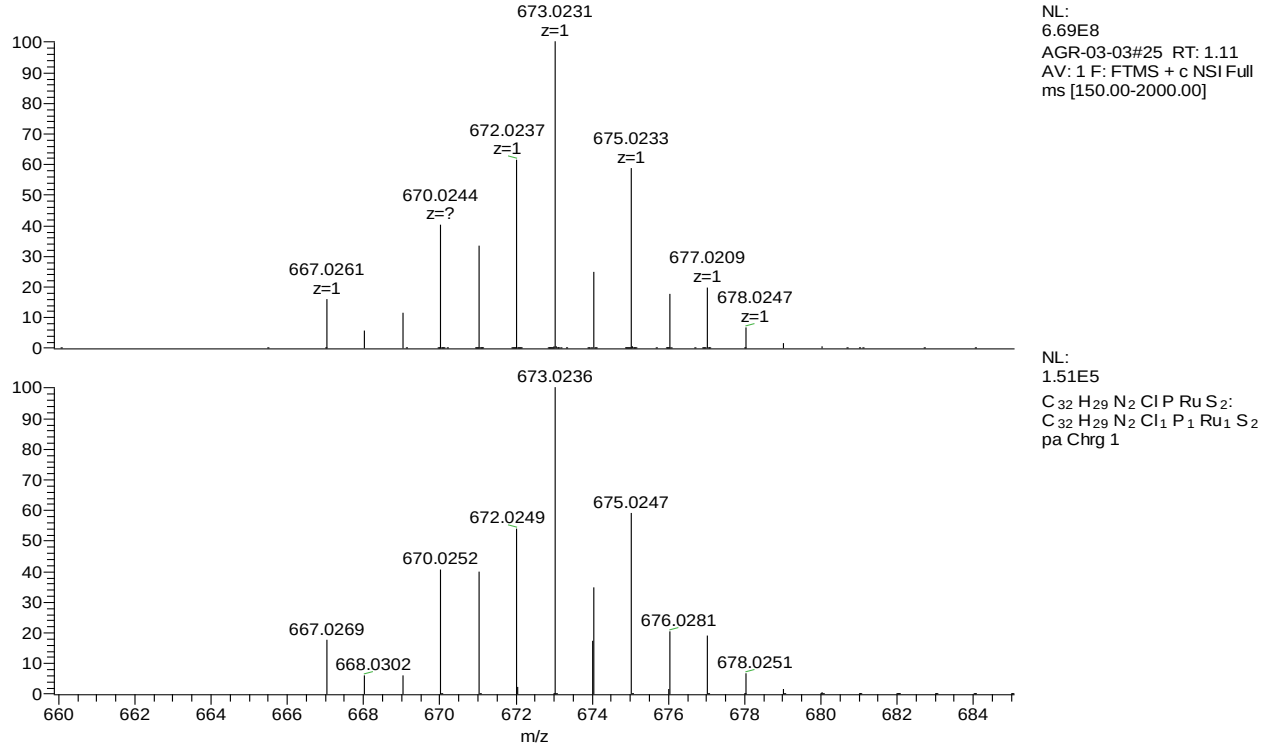

Figure S14. ESI-(HR)MS spectrum of **2** (top) and simulated spectrum of $C_{32}H_{29}N_2ClRuS_2^+$: (bottom).

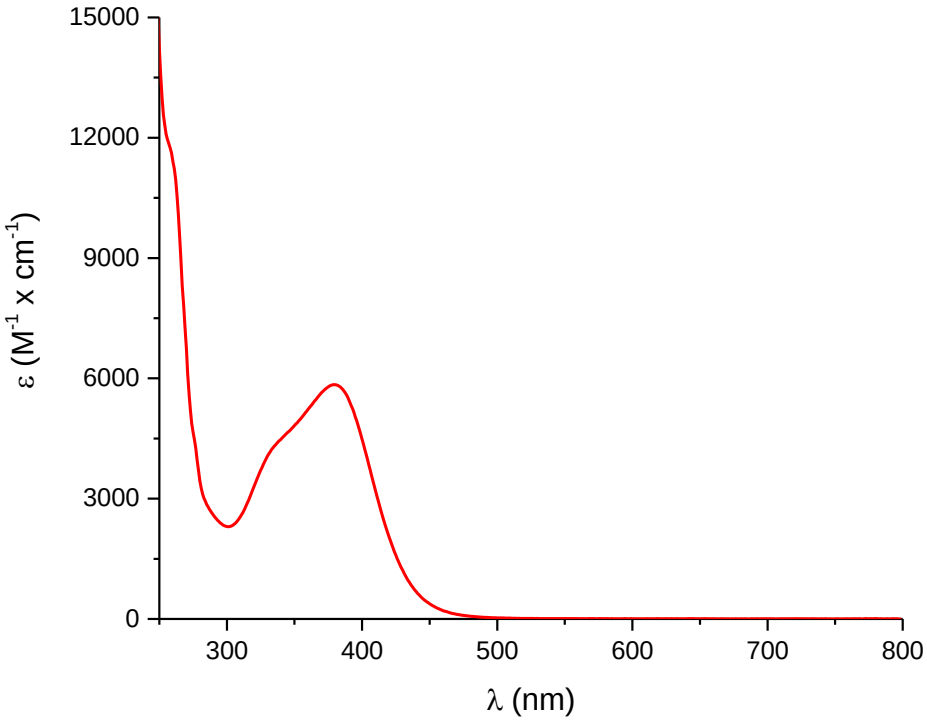

Figure S15. UV-Vis absorbance spectrum of complex **2** in dichloromethane.

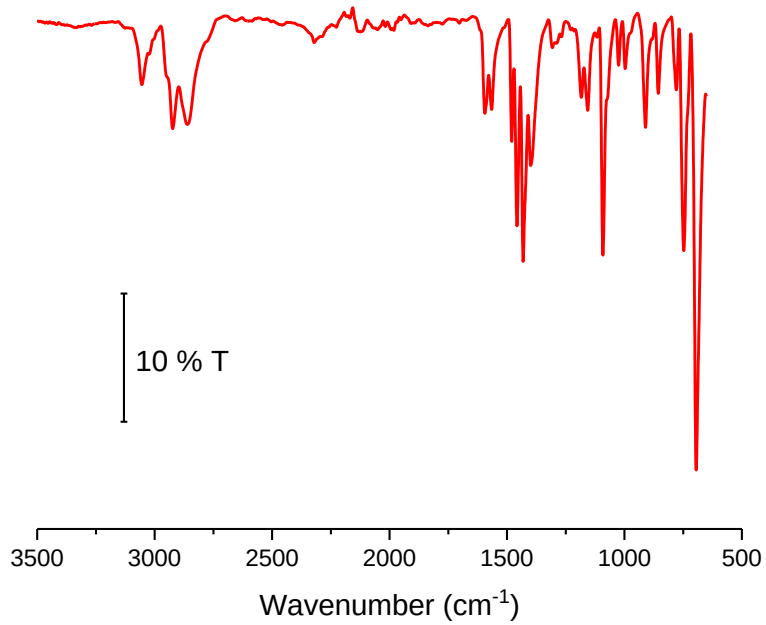

Figure S16. ATR FT-IR transmittance spectrum of **2**.

[Ru(N$_2$S$_2$)(DMSO)Cl]Cl, 3

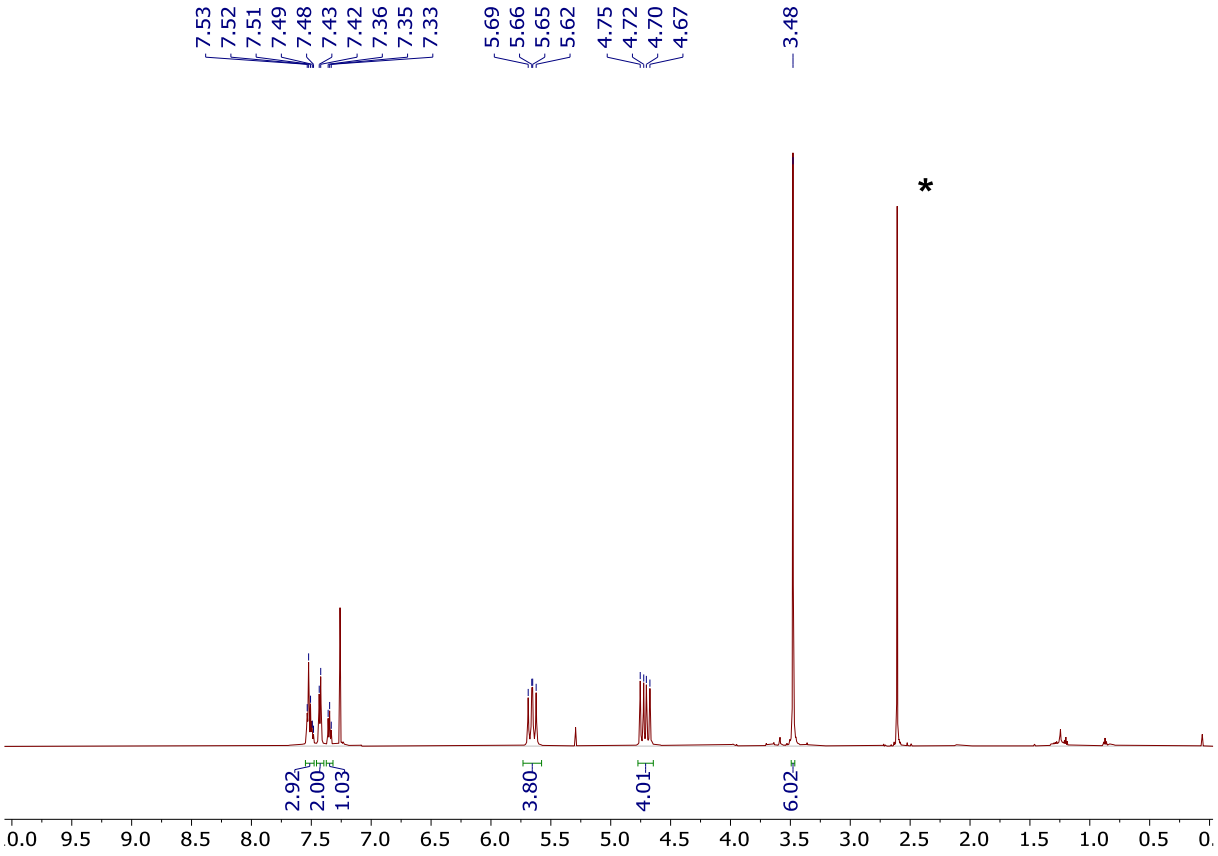

Figure S17. ^{1}H NMR spectrum of complex **3** in CD_3Cl at 23 °C. Peak of residual DMSO is marked with an asterisk.

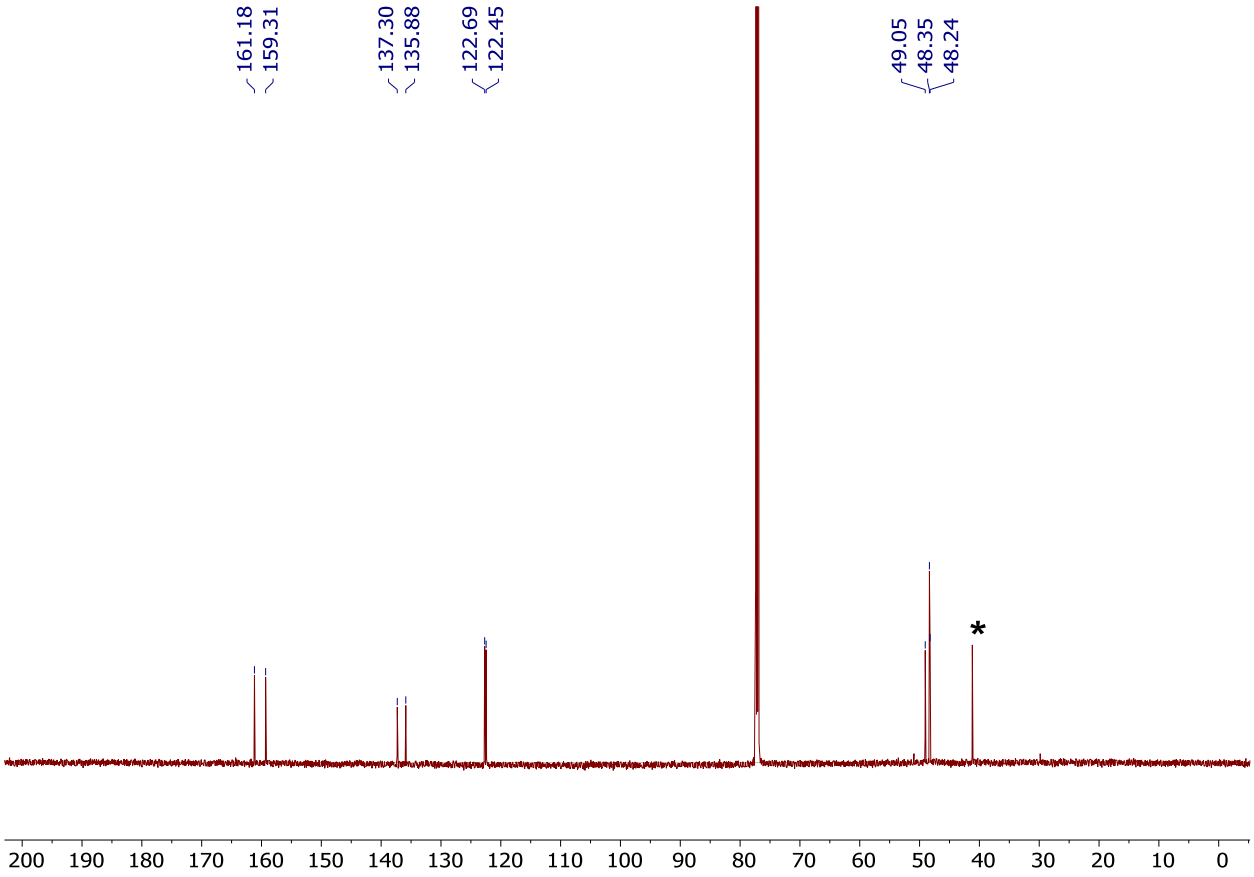

Figure S18. $^{13}C\{^{1}H\}$ NMR of complex **3** in CD_3Cl at 23 °C. Peak of residual DMSO is marked with an asterisk.

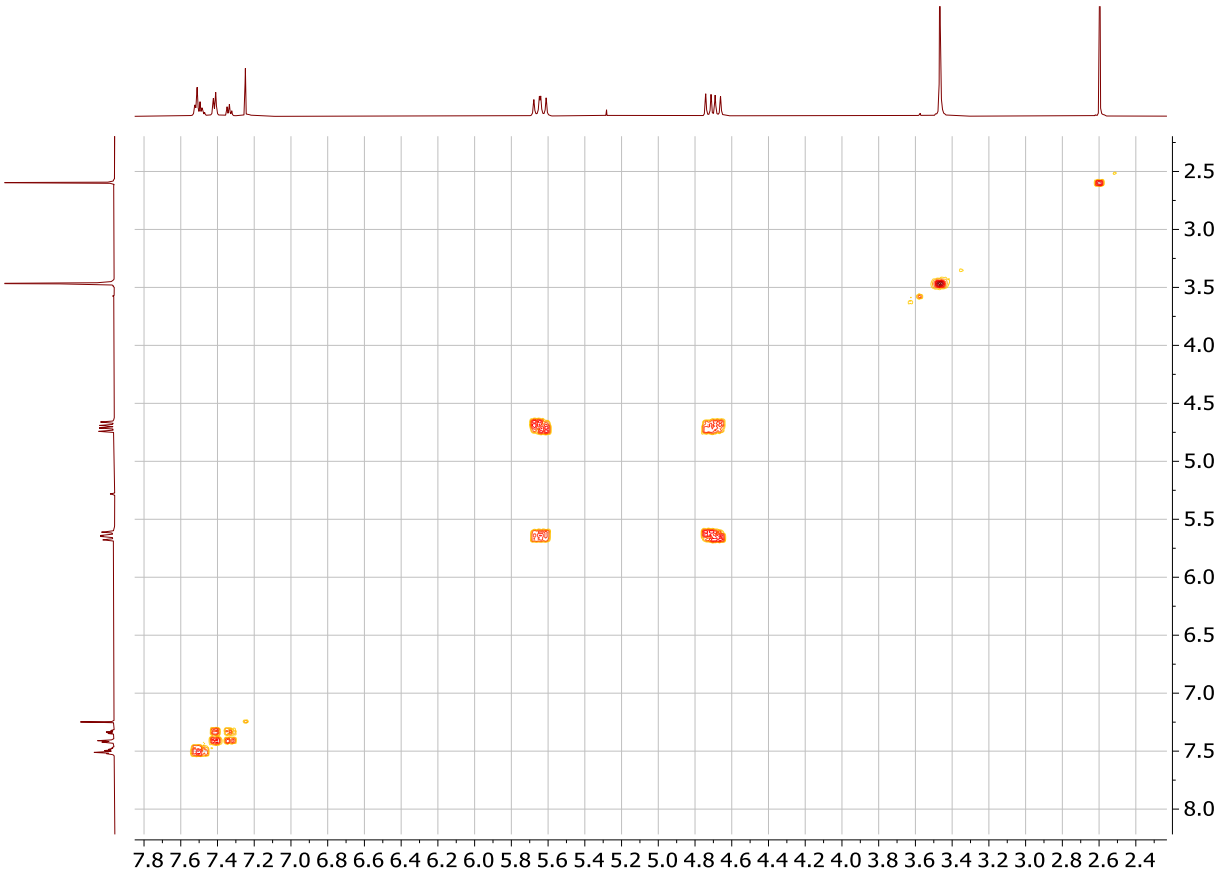

Figure S19. $^{1}H–^{1}H$ COSY spectrum of complex **3** in CD_3Cl at 23 °C

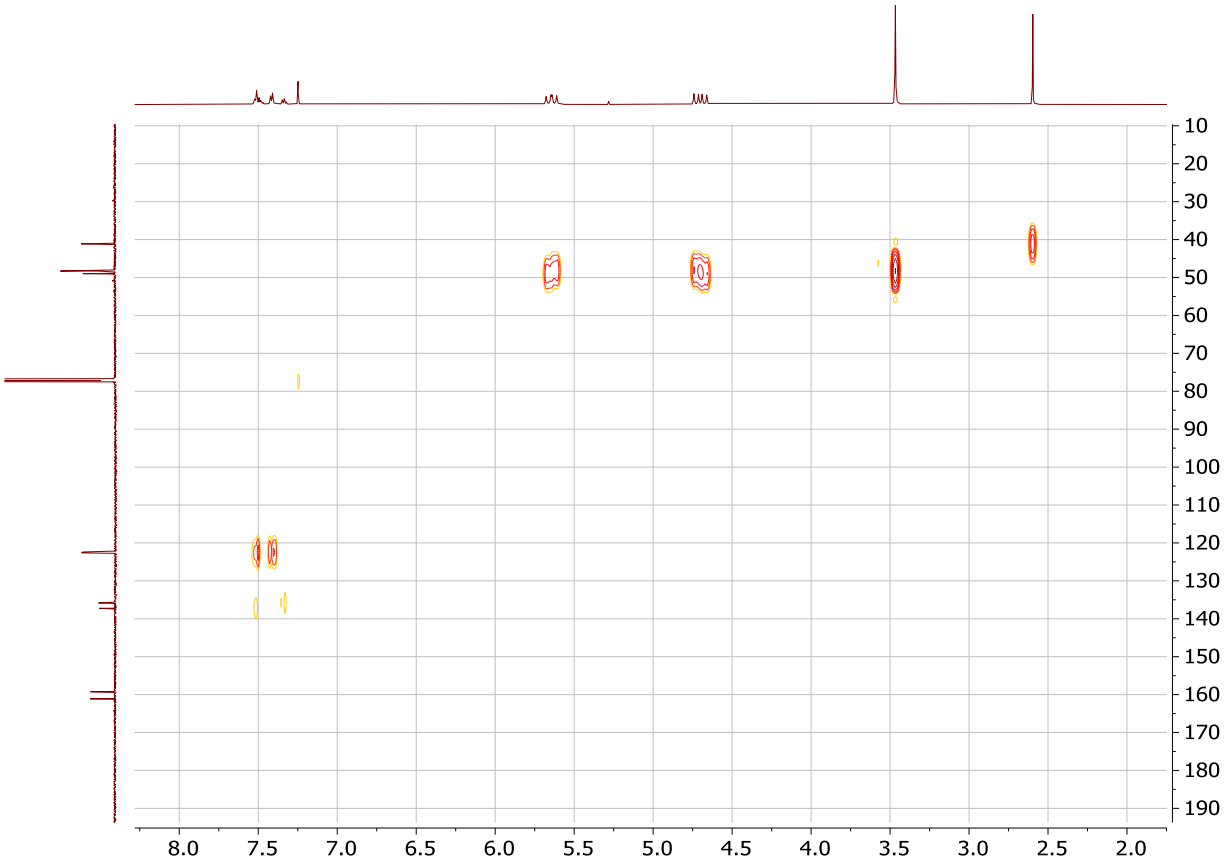

Figure S20. ^{1}H-^{13}C HMQC spectrum of complex **3** in CD_3Cl at 23 °C.

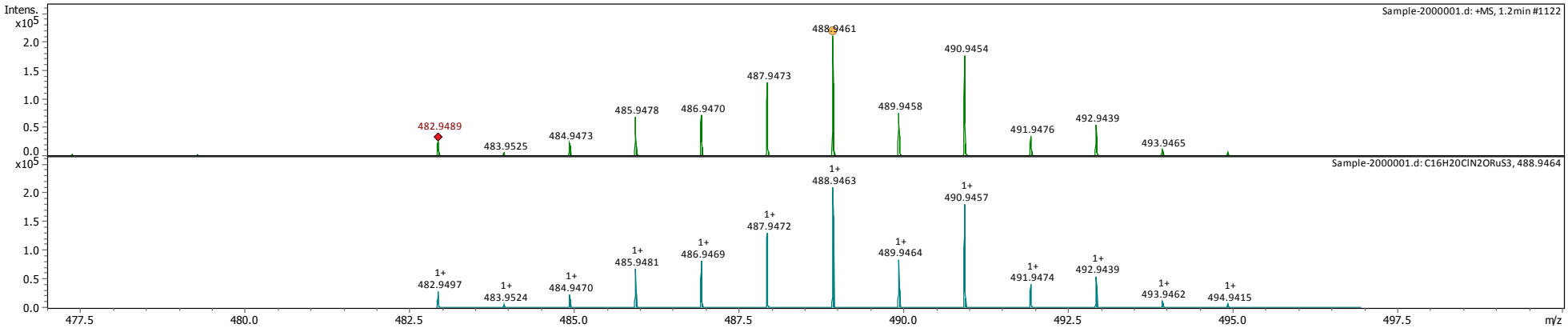

Figure S21. ESI-(HR)MS spectrum of **3** (top) and simulated spectrum of $C_{16}H_{20}ClN_2ORuS_3^+$ (bottom).

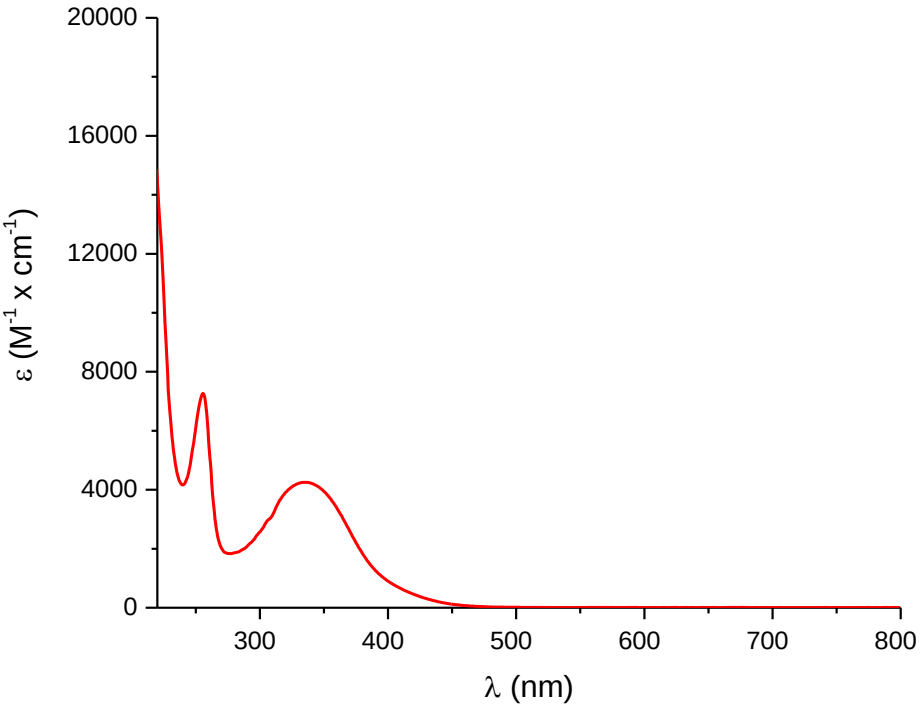

Figure S22. UV-Vis absorbance spectrum of complex **3** in methanol.

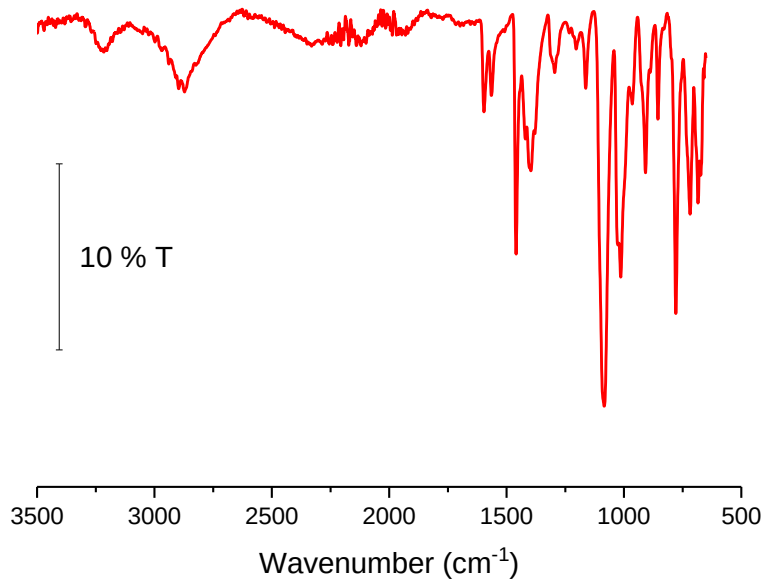

Figure S23. ATR-IR transmittance spectrum of **3**.

[Ru(N$_2$S$_2$)H(CO)(PPh$_3$)]Cl, 4

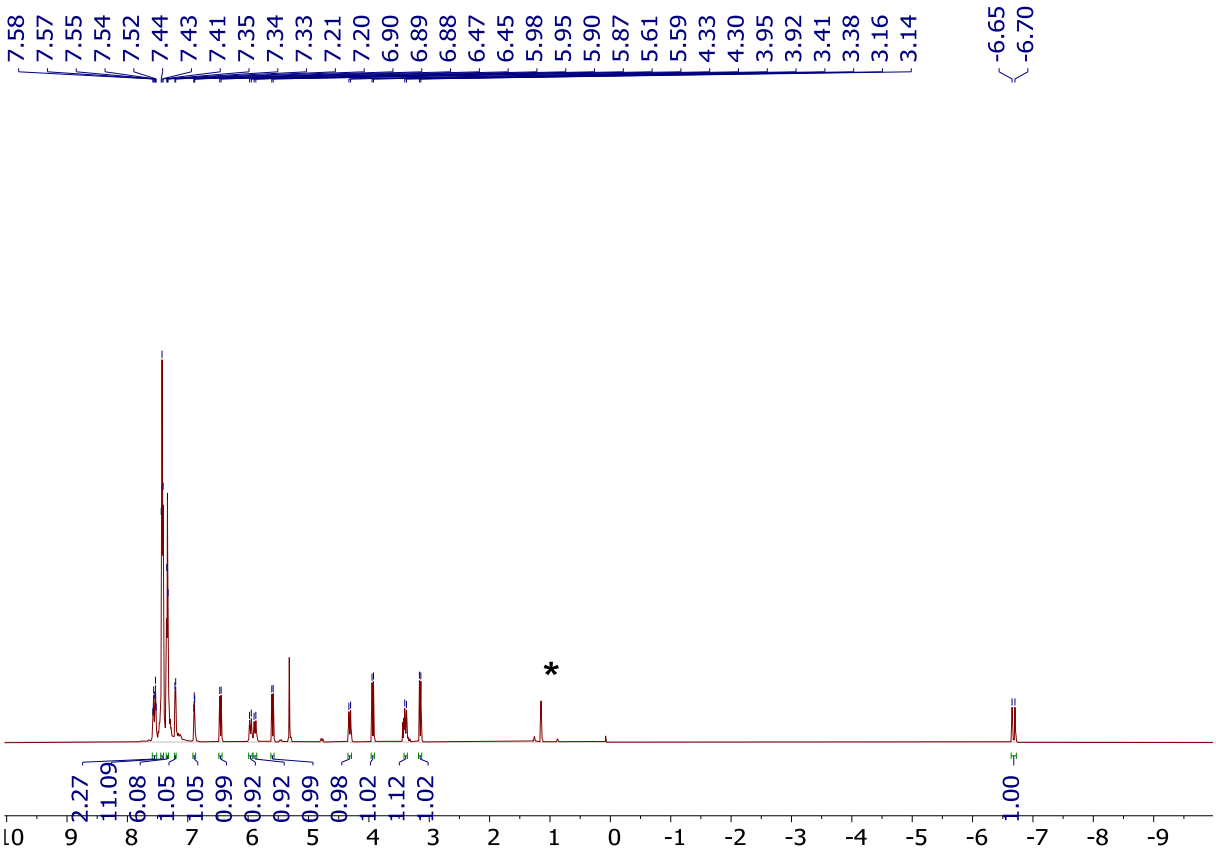

Figure S24. ^{1}H NMR spectrum of complex **4** in CD_2Cl_2 at 23 °C. Peak of residual diethyl ether is marked with an asterisk.

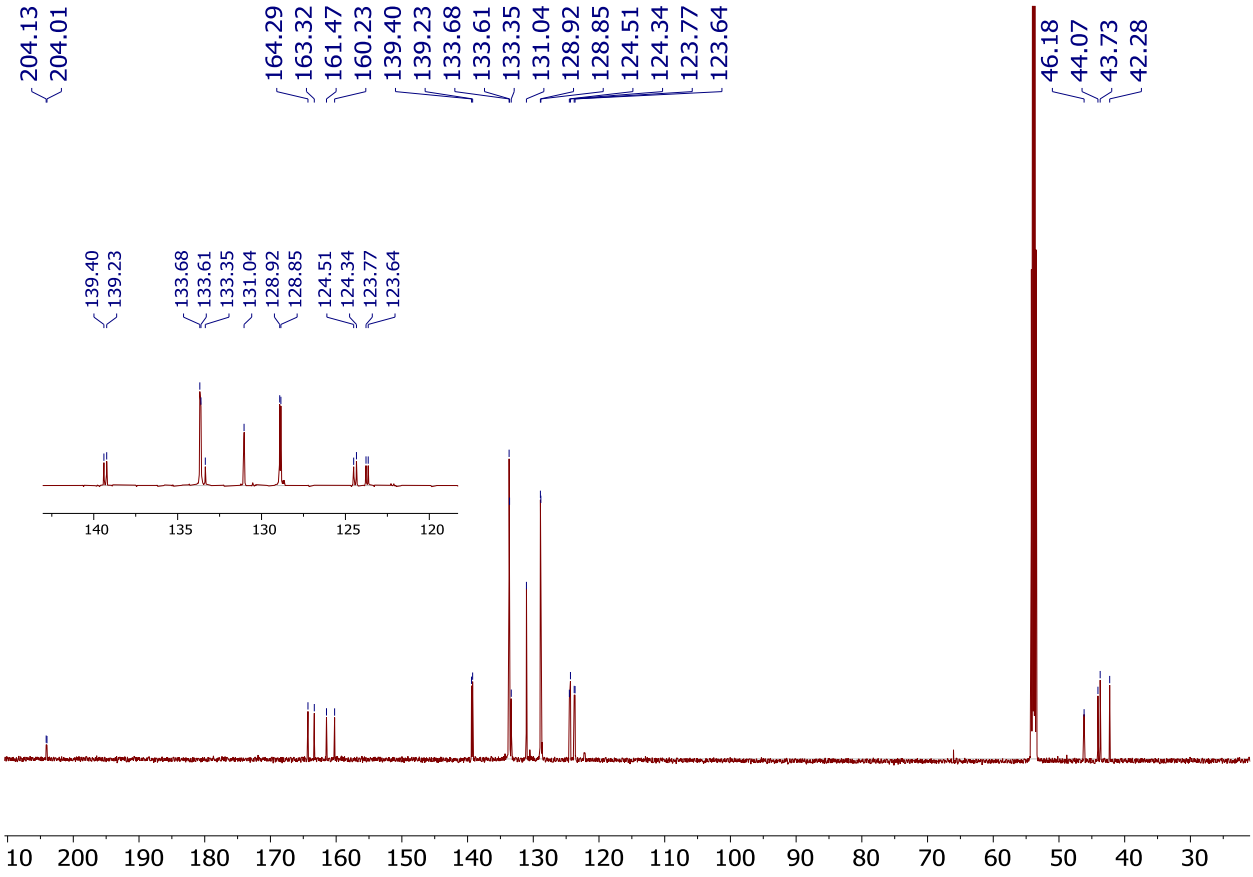

Figure S25. ^{13}C{^{1}H} NMR of complex **4** in CD_2Cl_2 at 23 °C.

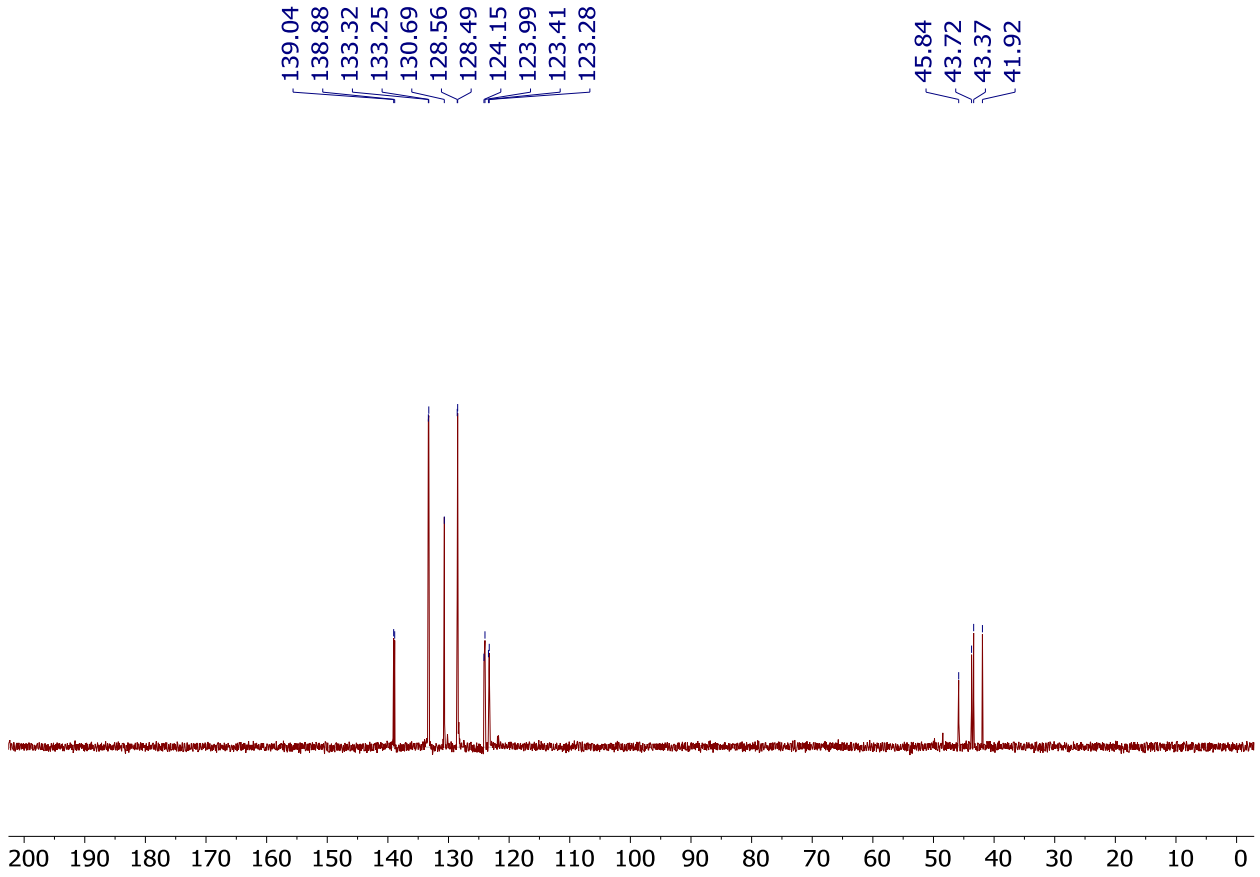

Figure S26. DEPT-135 spectrum of complex **4** in CD_2Cl_2 at 23 °C.

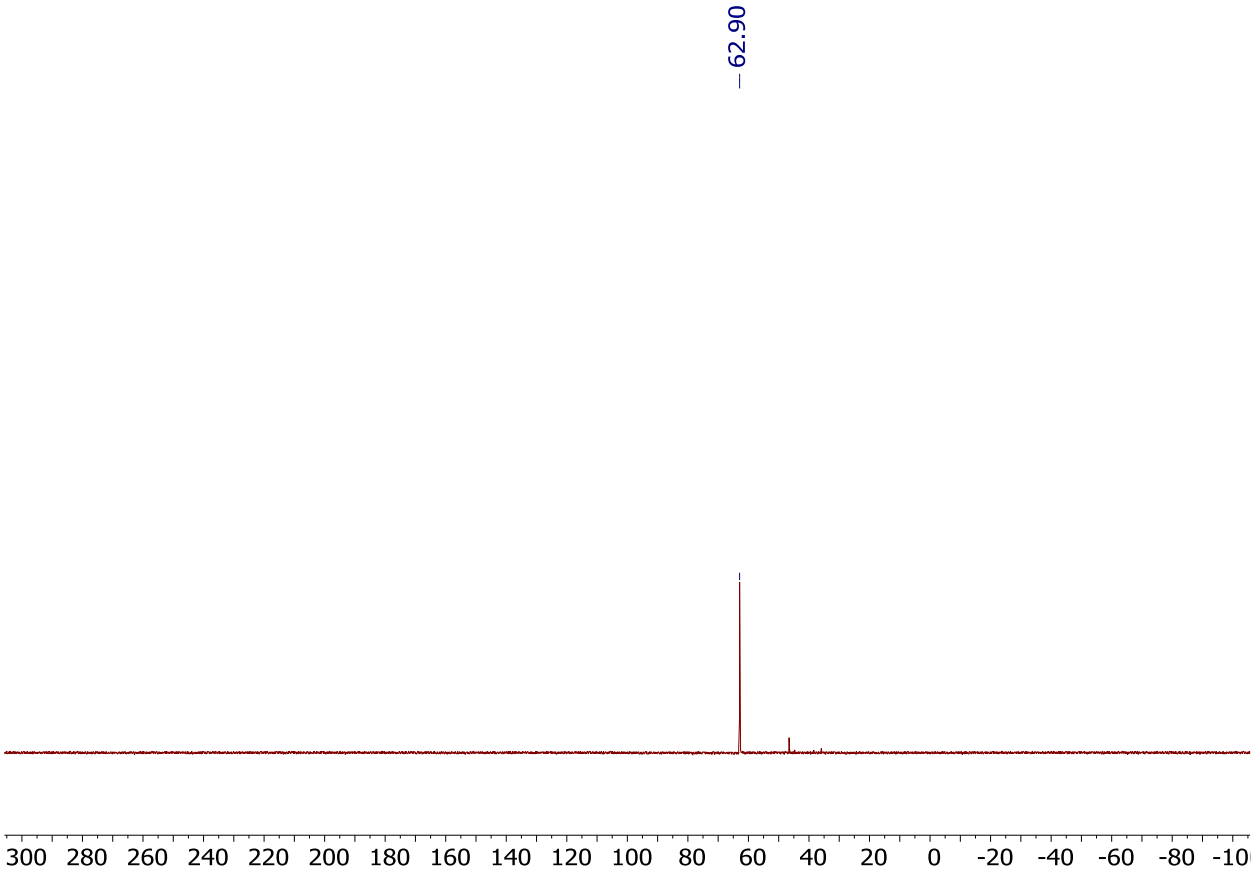

Figure S27. $^{31}P\{^{1}H\}$ NMR spectrum of complex **4** in CD_2Cl_2 at 23 °C.

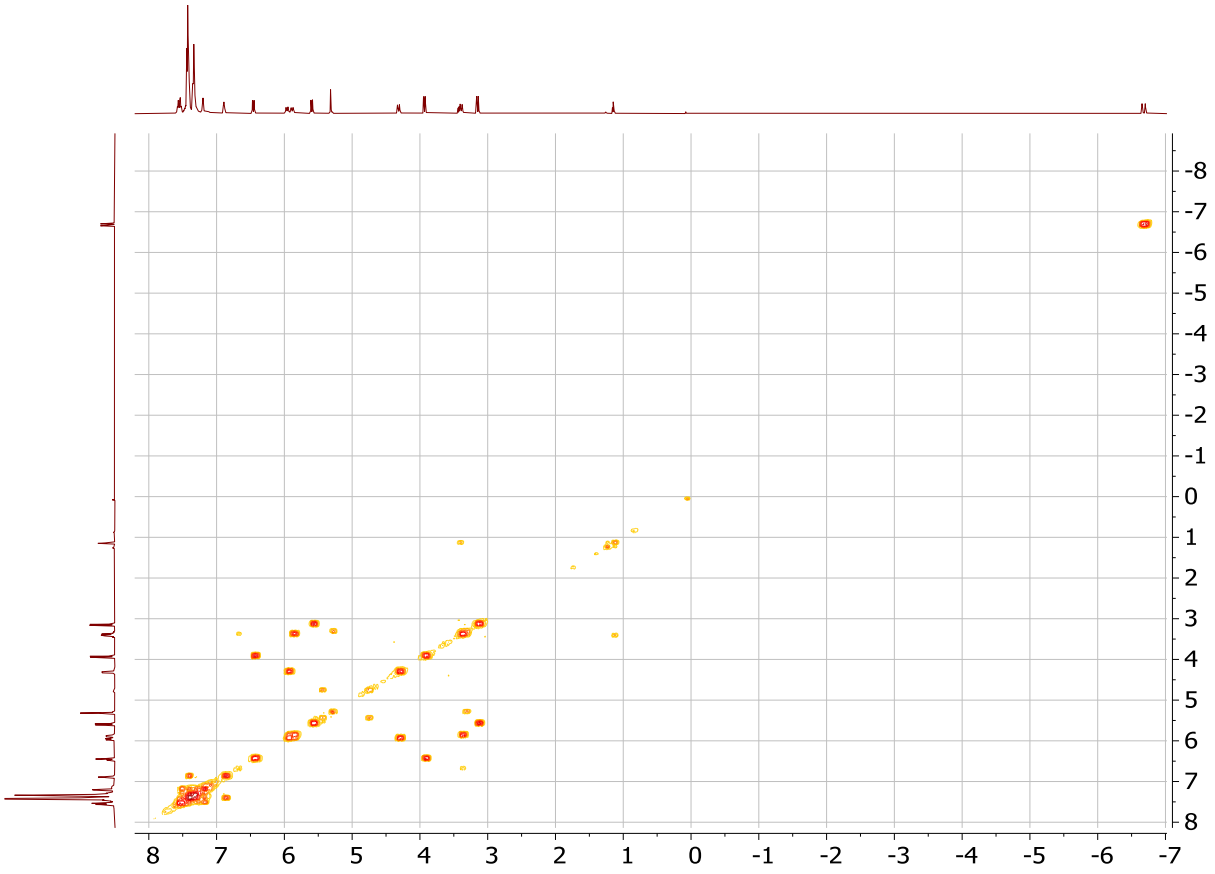

Figure S28. ^{1}H–^{1}H COSY spectrum of complex **4** in CD_3Cl at 23 °C.

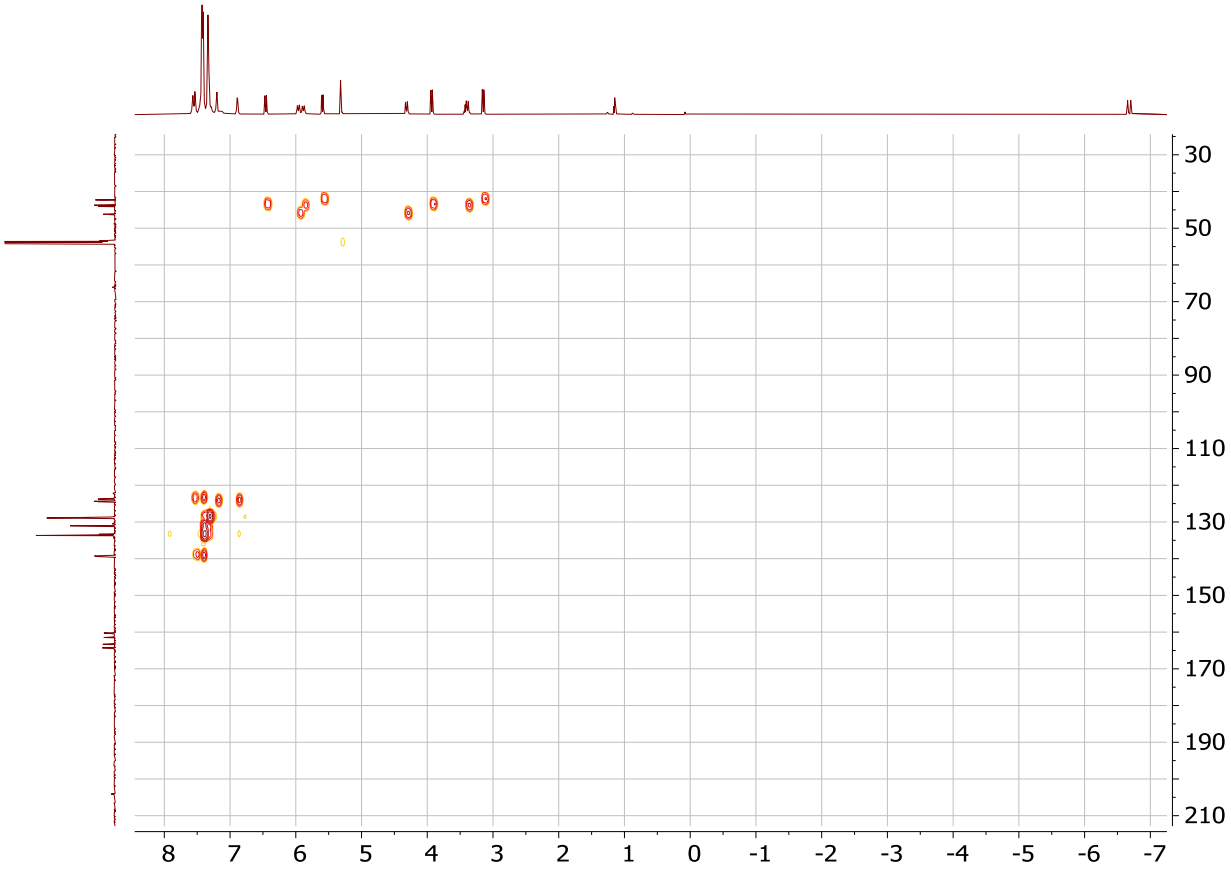

Figure S29. ^{1}H–^{13}C HMQC spectrum of complex **4** in CD_2Cl_2 at 23 °C.

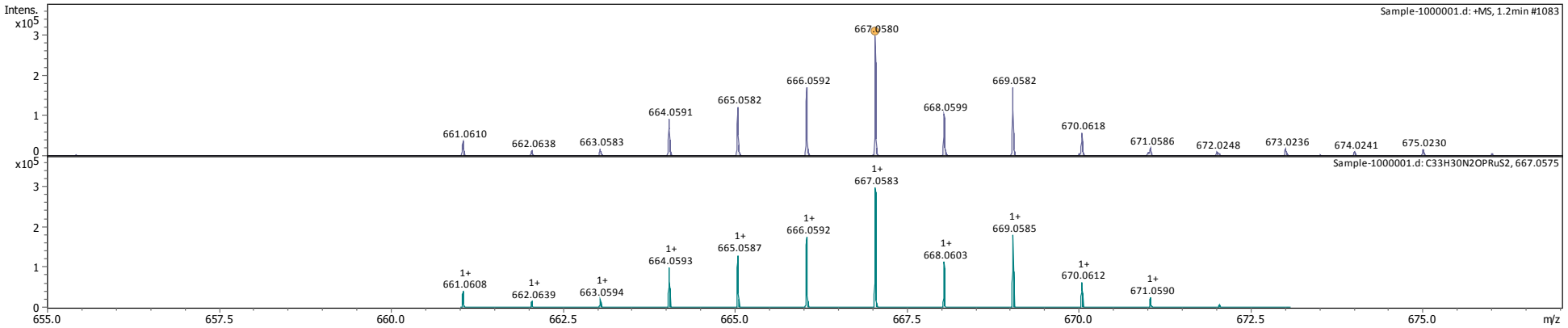

Figure S30. ESI-(HR)MS spectrum of **4** (top) and simulated spectrum of $C_{33}H_{30}N_2OPRuS_2^+$ (bottom).

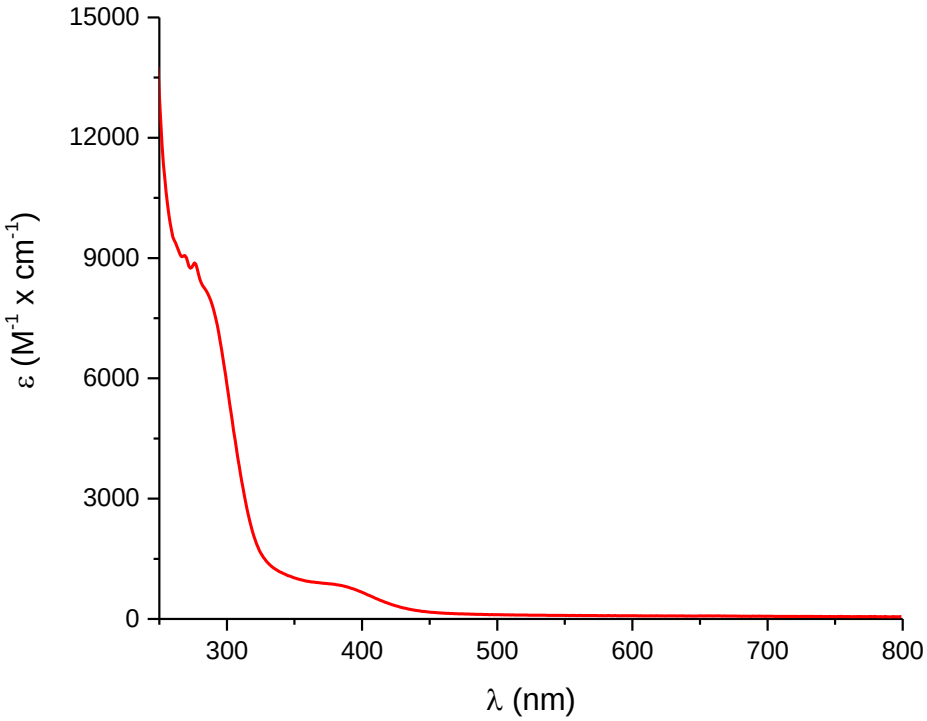

Figure S31. UV-vis absorbance spectrum of **4** in dichloromethane**.**

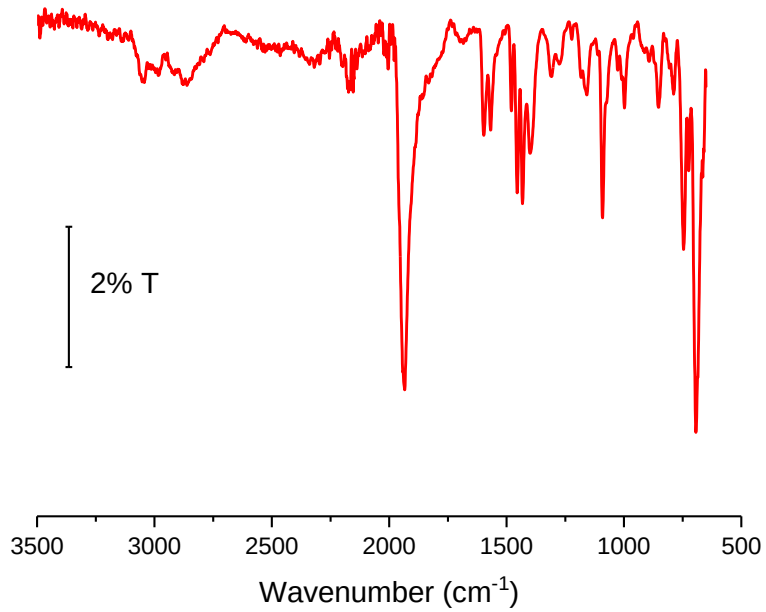

Figure S32. ATR-IR transmittance spectrum of **4**.

2. Deprotonation of (N_2S_2)Ru(II) complexes

Deprotonation of 1

Formation of monodeprotionated species 1a

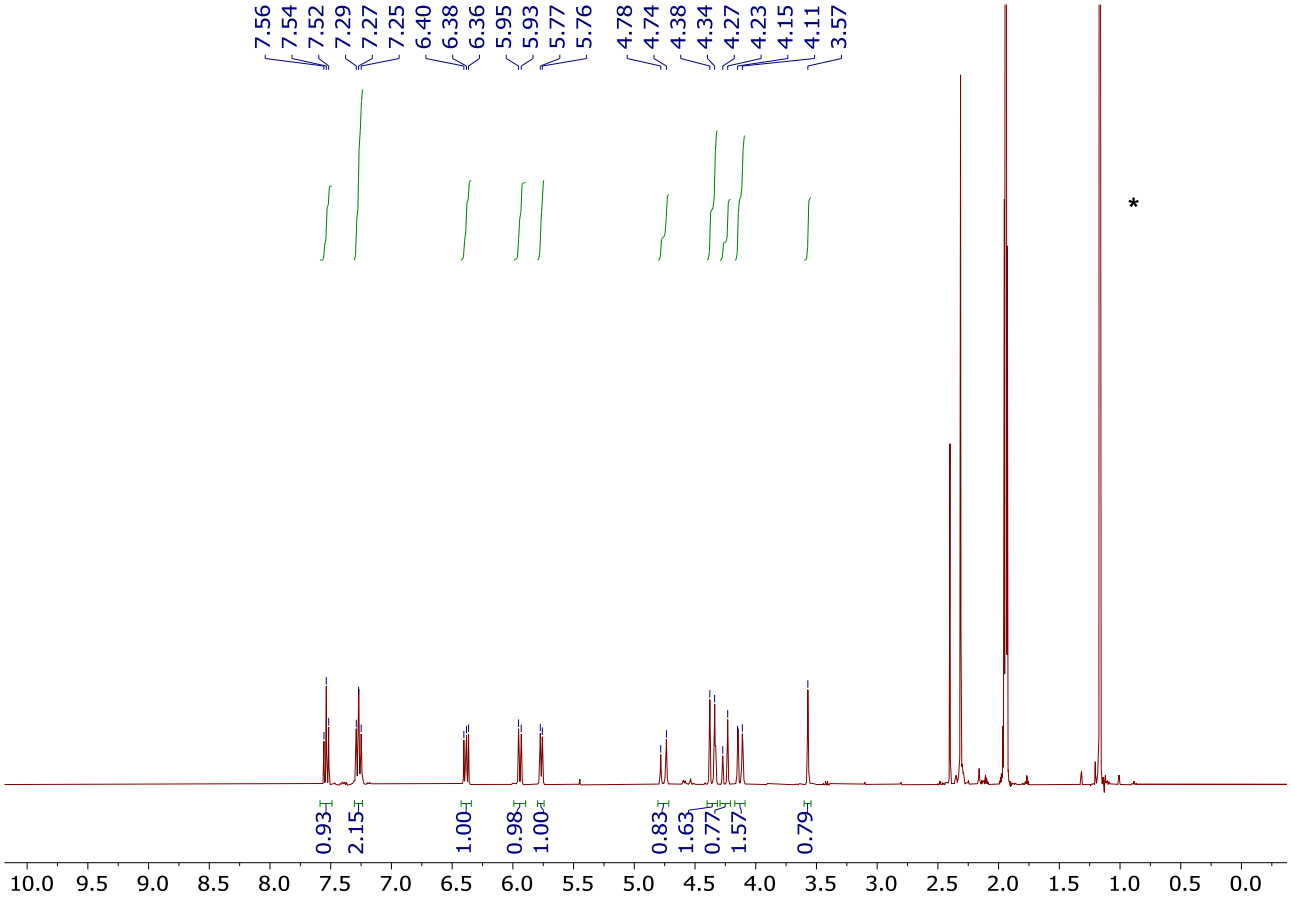

Figure S33. ^{1}H NMR spectrum of **1a** in acetonitrile-d_3 at 23 ^{o}C. Peak of residue ^{t}BuOH is marked as an asterisk. The integration of CH_2 and CH group relative to aromatic protons remains essentially unchanged during the course of 16 h at room temperature. Relaxation delay of 20 s was used to ensure correct integration in ^{1}H NMR.

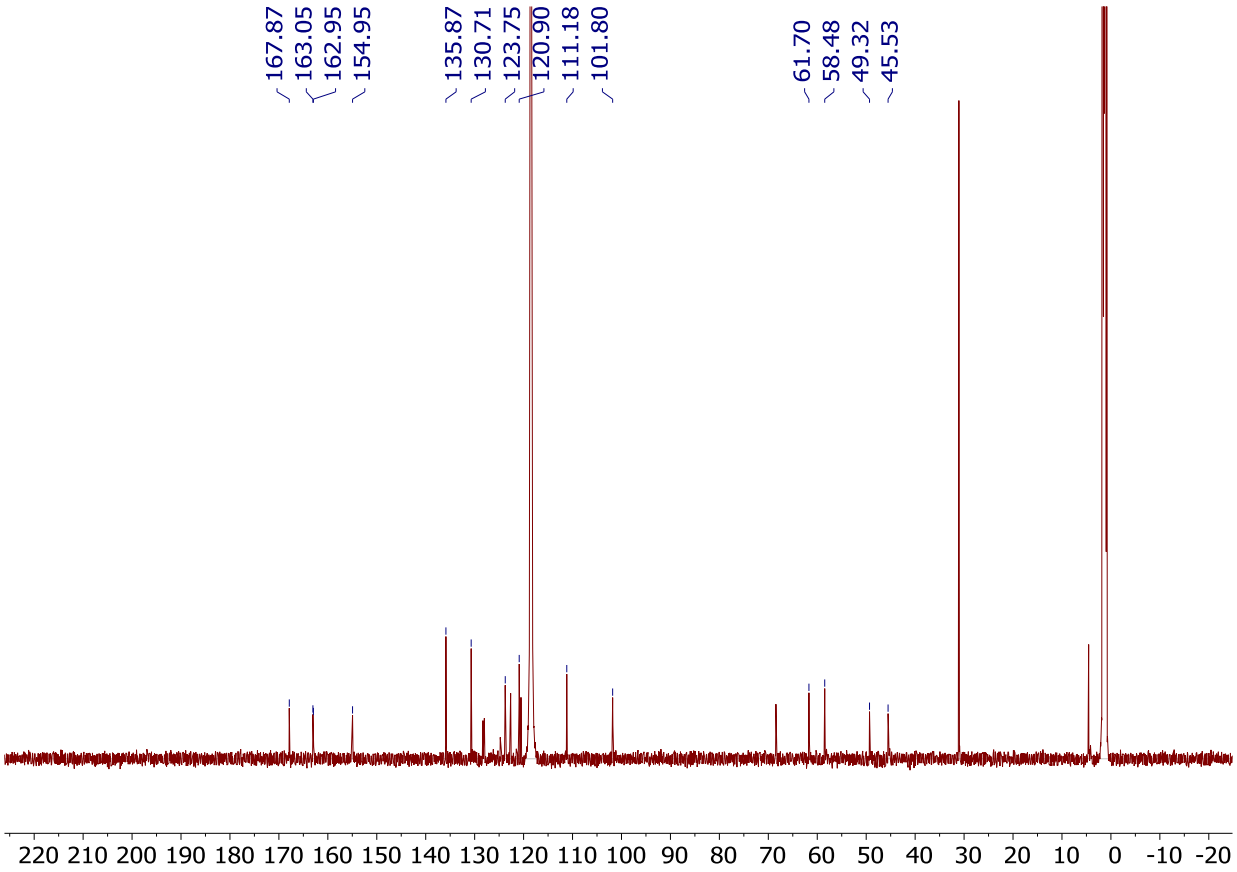

Figure S34. $^{13}C\{^{1}H\}$ NMR spectrum of **1a** in acetonitrile-d_3 at -30 °C.

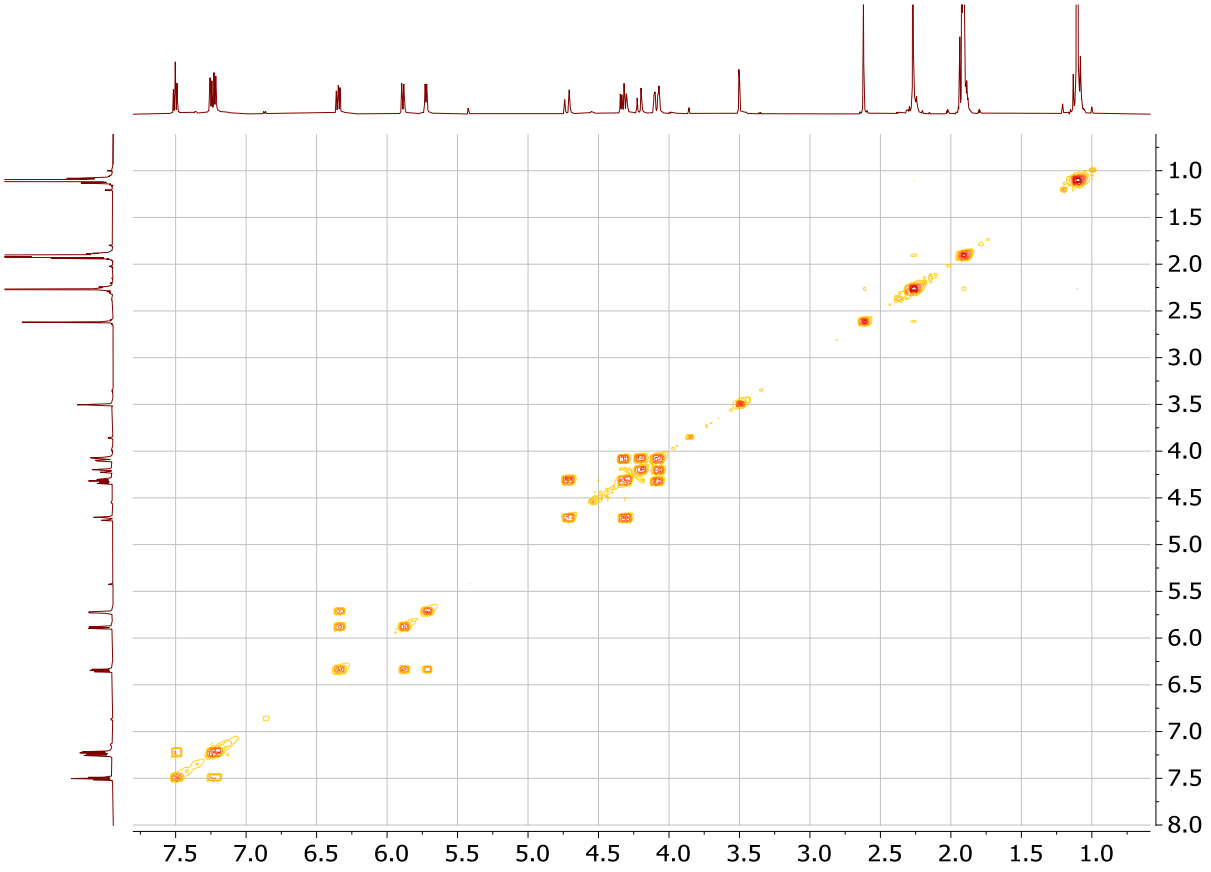

Figure S35. ^{1}H-^{1}H COSY spectrum of **1a** in acetonitrile-d_3 at -30 °C.

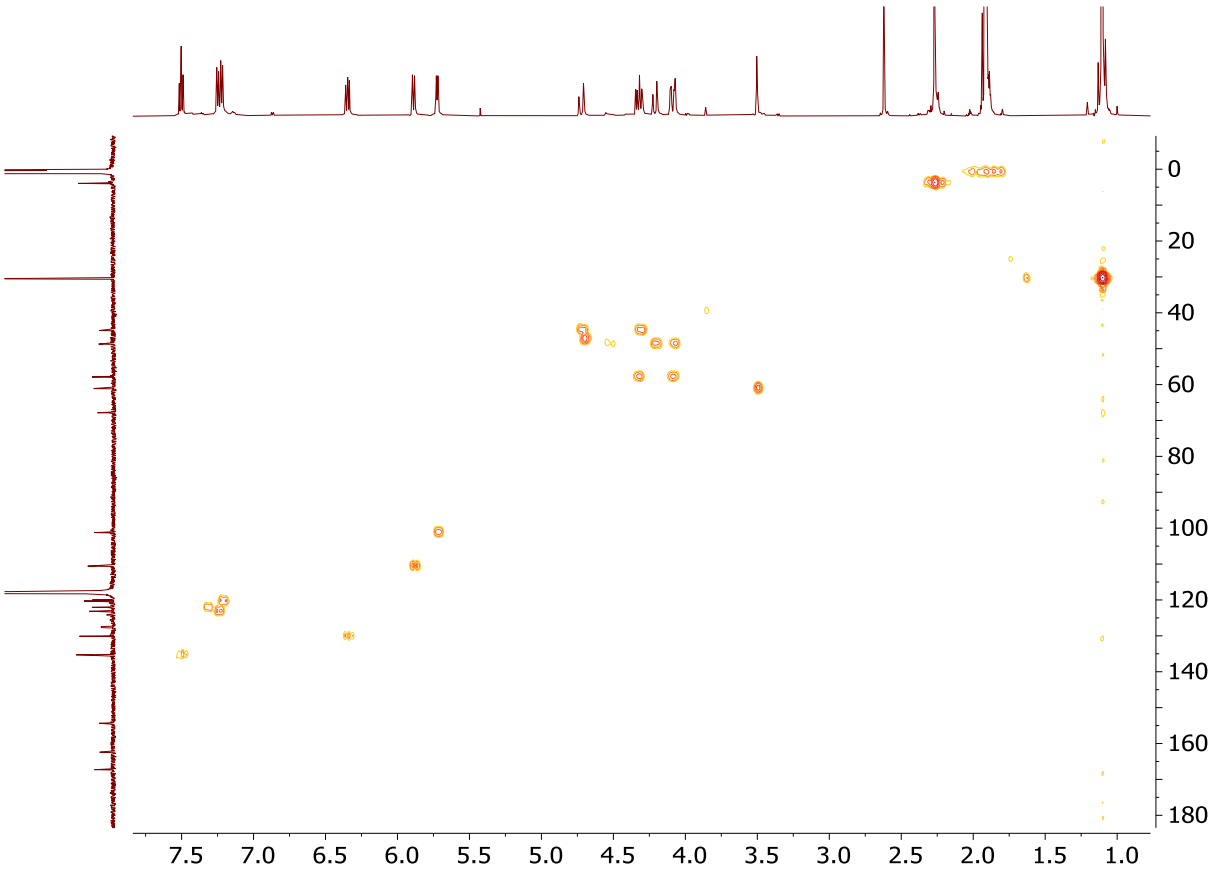

Figure S36. ^{1}H-^{13}C HMQC spectrum of **1a** in acetonitrile-d_3 at -30 °C.

NMR yield determination of 1a

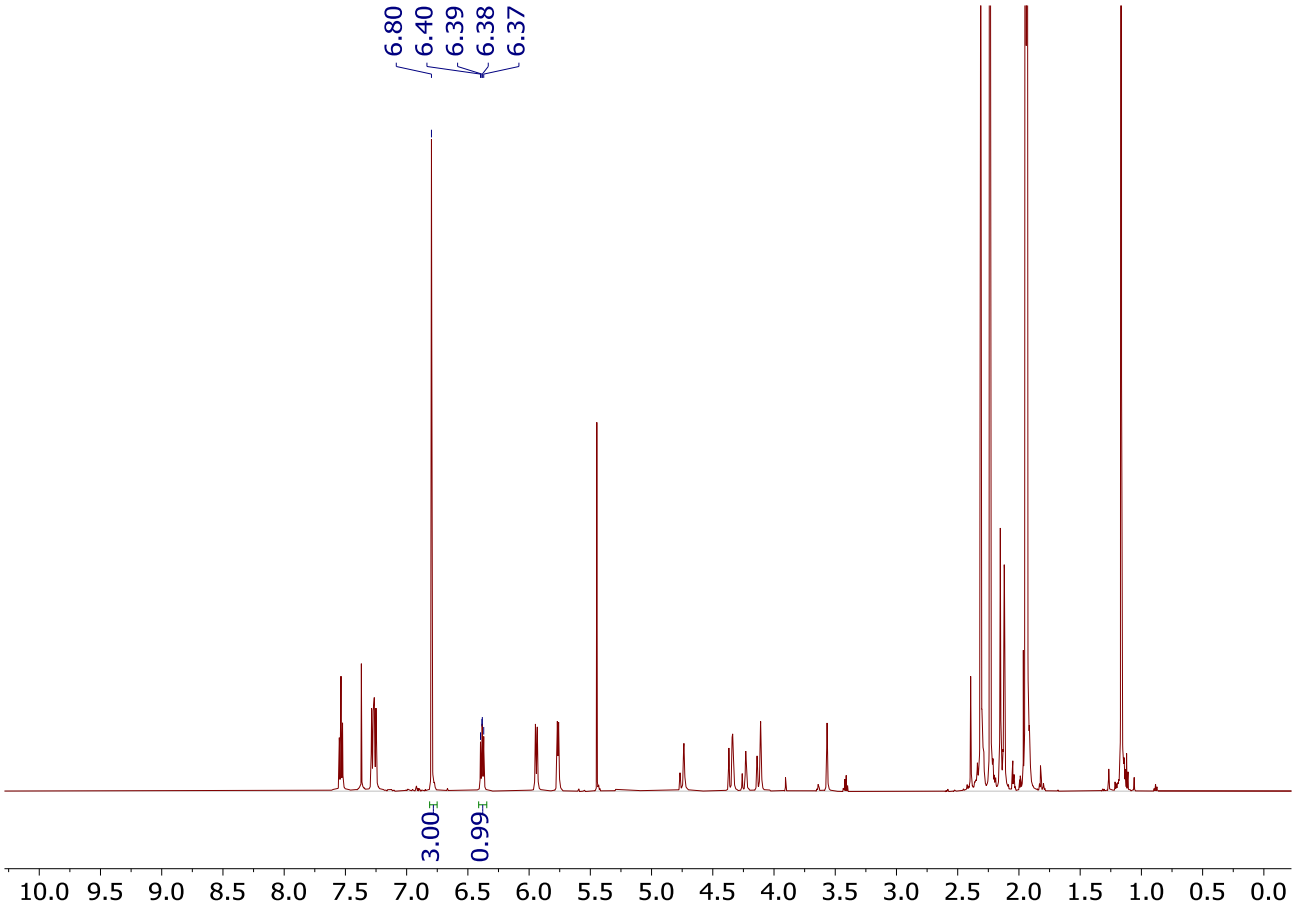

Figure S37. NMR yield determination of **1a** by integration against internal standard, mesitylene, in acetonitrile-d_3. Complex **1a** was obtained by deprotonation of **1** with 1.1 equiv of KO^{t}Bu.

Protonation of 1a

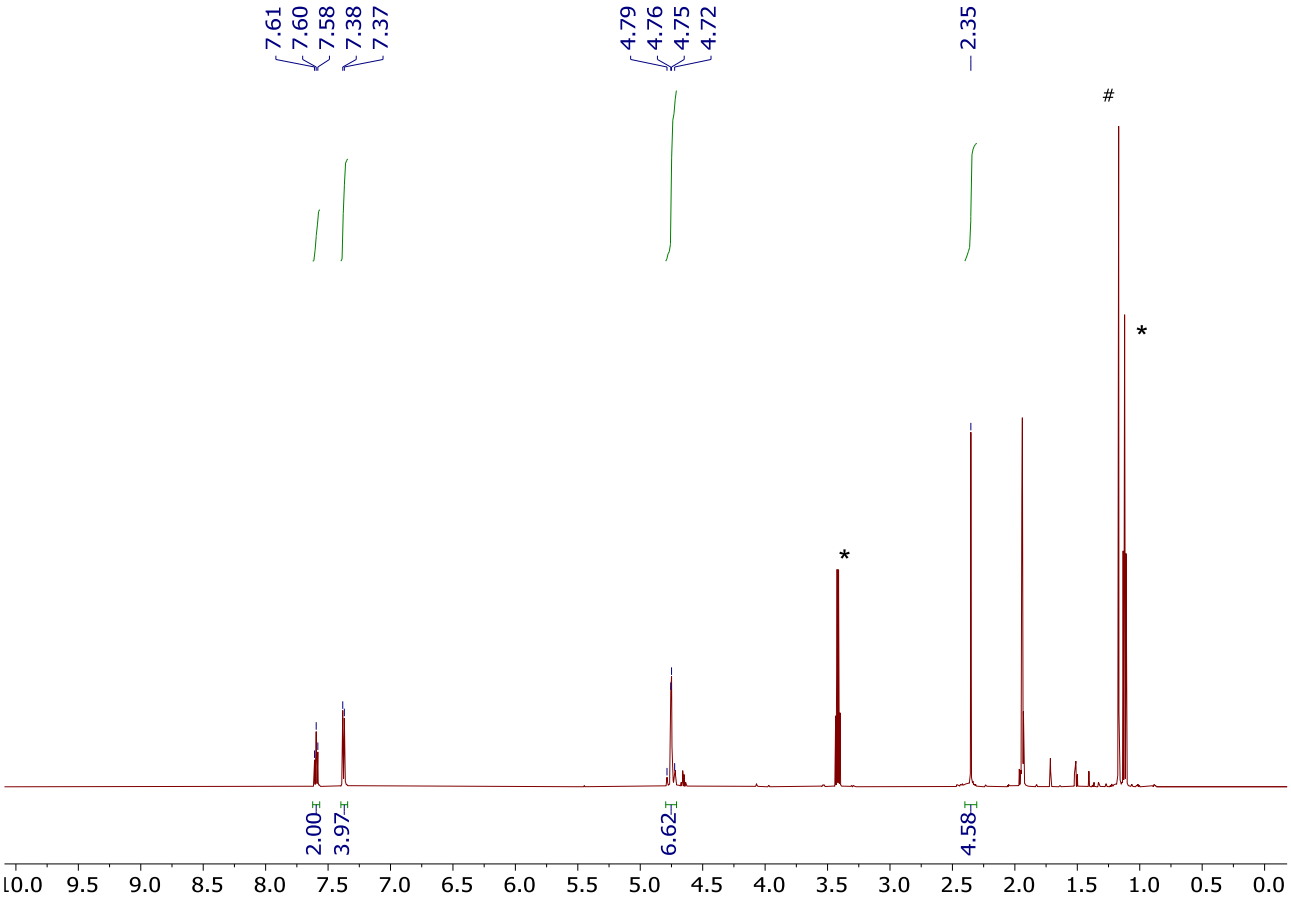

Figure S38. ^{1}H NMR spectrum of the product of protonation of **1a** with 1.1 equiv. of HBF_4*Et_2O. Peak of residual Et_2O and ^{t}BuOH are marked with an asterisk and a hash, respectively.

Formation of 1b

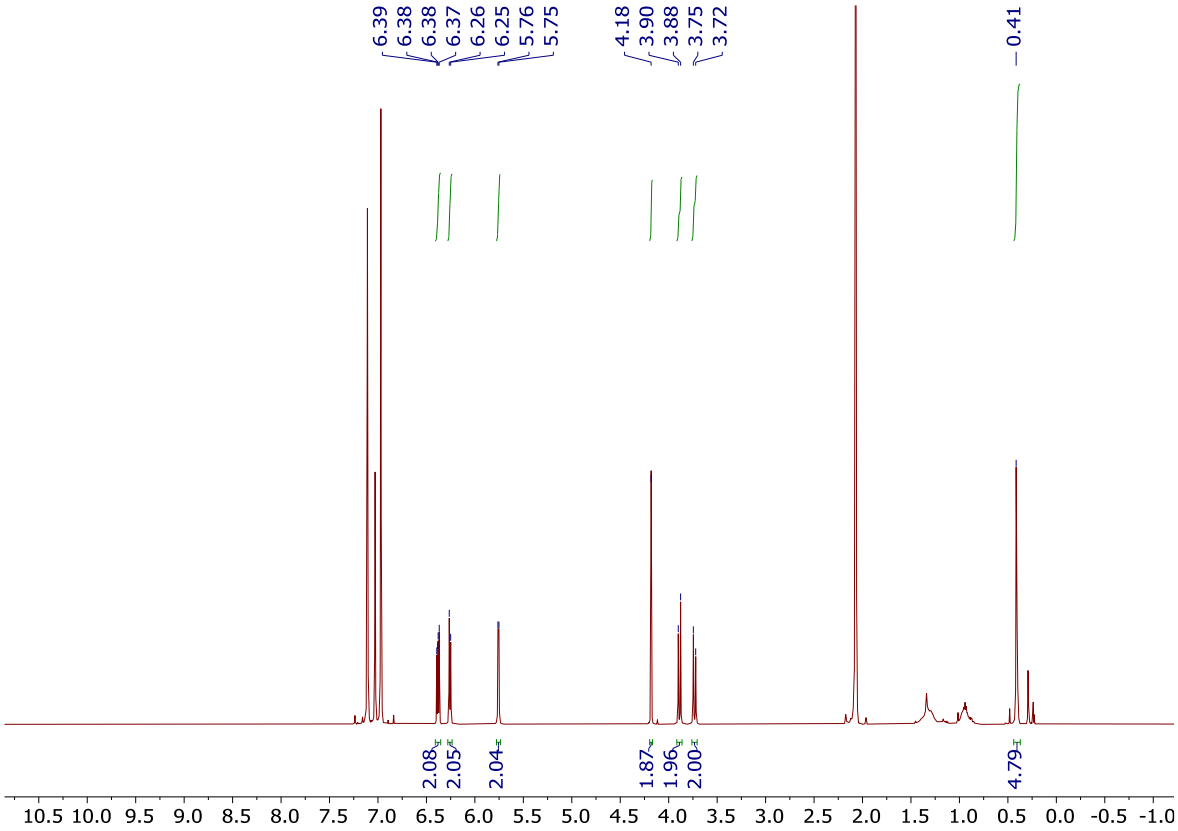

Figure S39. ^{1}H NMR spectrum of **1b** in toluene-d_8 at -25 ^{o}C.

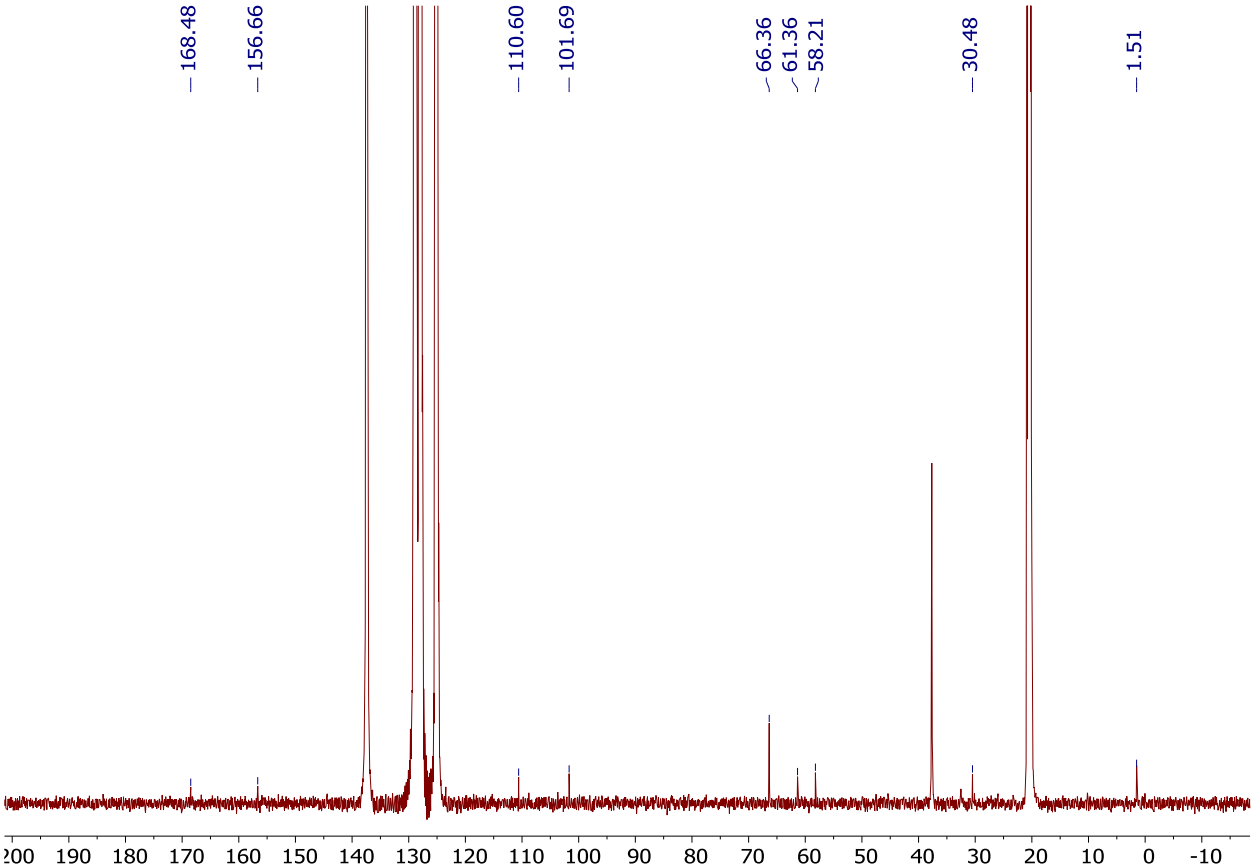

Figure S40. ^{13}C{^{1}H} NMR spectrum of **1b** in toluene-d_8 at -30 ^{o}C.

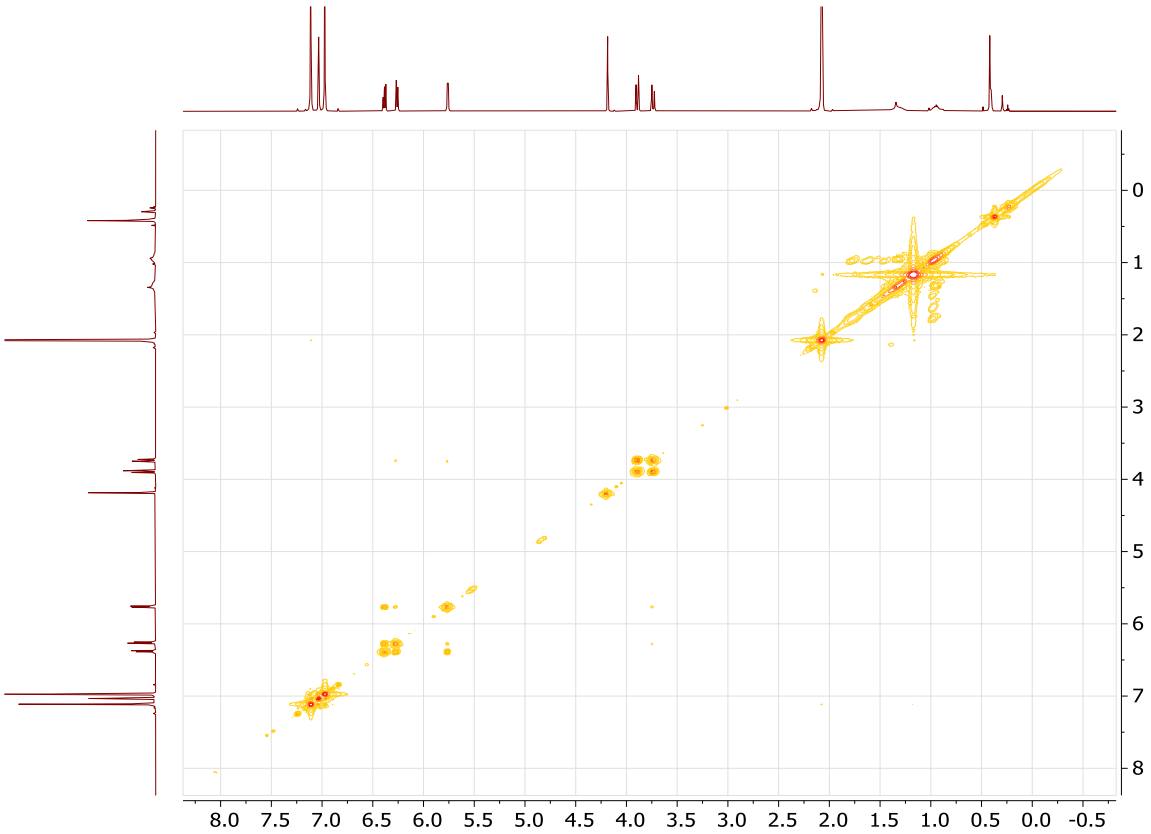

Figure S41. ^{1}H-^{1}H COSY spectrum of **1b** in C_7D_8 at -30 °C.

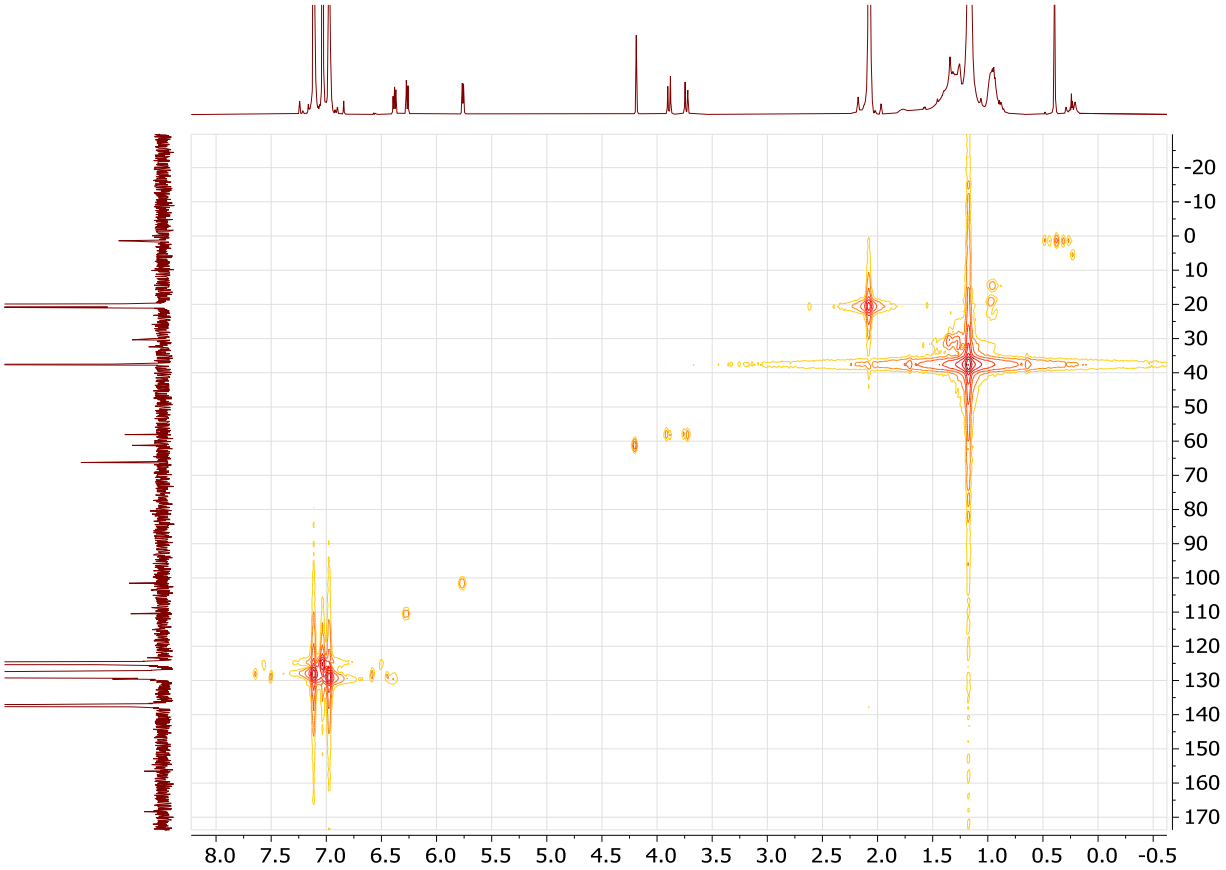

Figure S42. ^{1}H-^{13}C HMQC spectrum of **1b** in C_7D_8 at -30 °C.

Formation of 1b in toluene-d_8 in the presence of internal standard

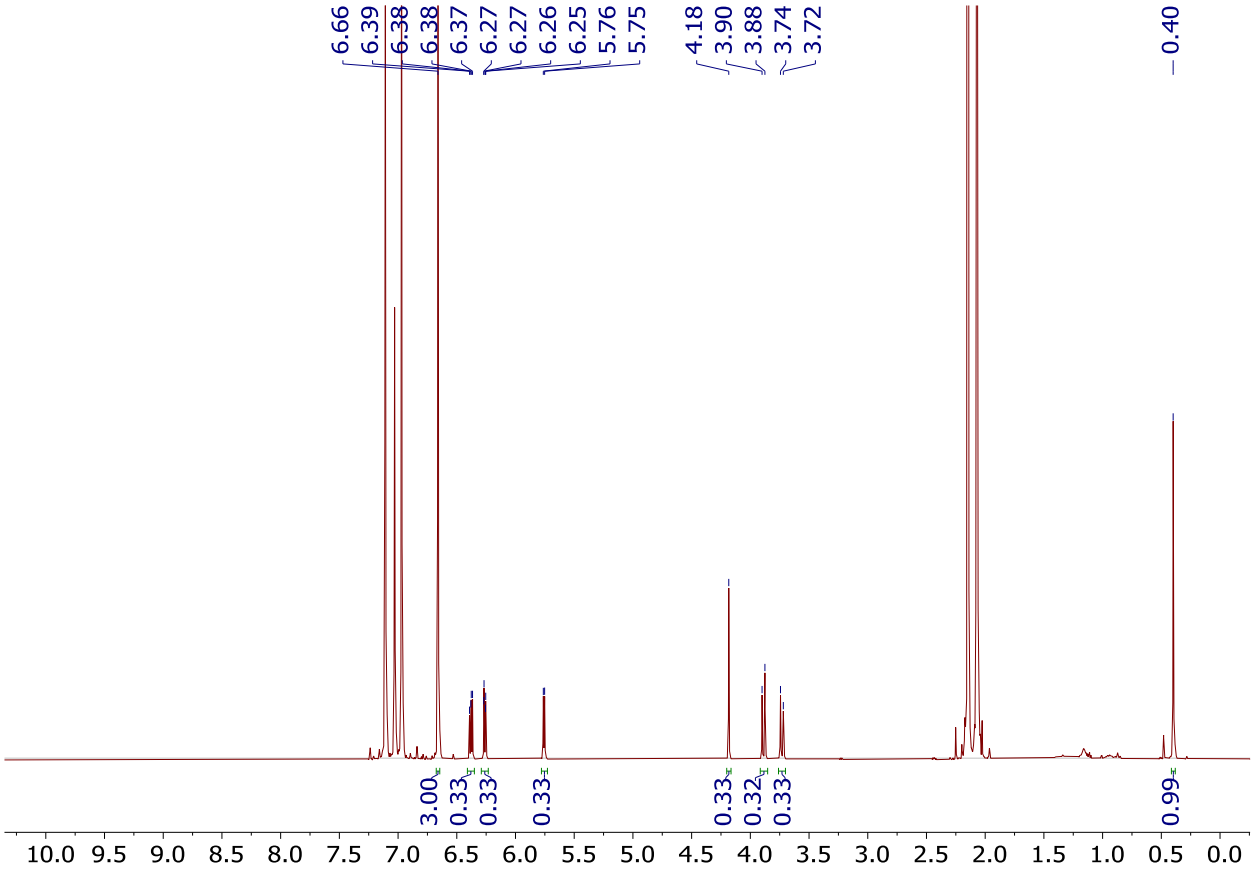

Figure S43. ^{1}H NMR spectrum of **1b** in the presence of mesitylene internal standard and 2 equiv. of KO^{t}Bu in toluene-d_8 after stirring for 3 min.

Formation of 1b in acetonitrile

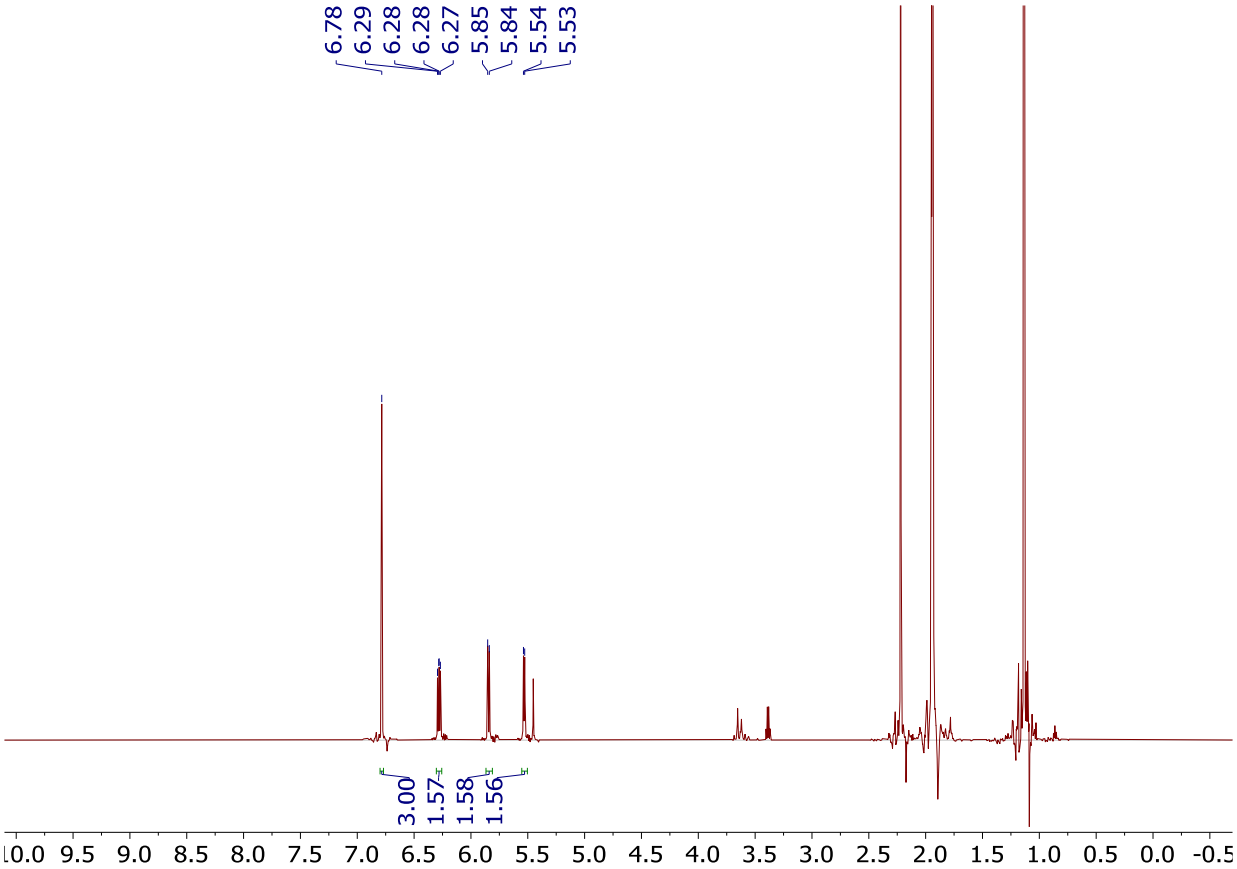

Figure S44. ^{1}H NMR spectrum of **1b** formed from **1** and 2.2 equiv of KO^{t}Bu in acetonitrile-d_3 at -30 ^{o}C. Methylene and methine peaks appear at diminished intensity due to H/D exchange with CD_3CN.

Protonation of 1b

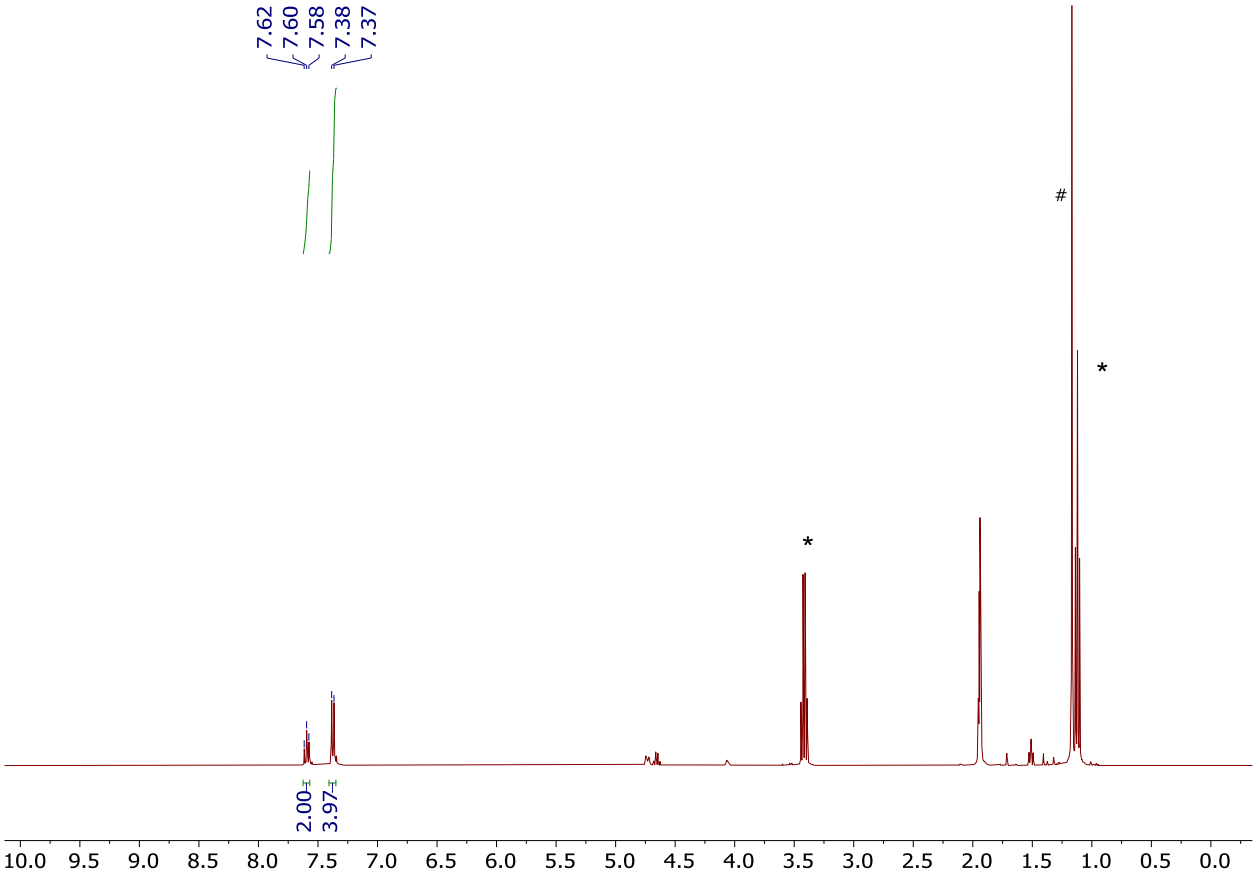

Figure S45. ^{1}H NMR spectrum of the product of protonation of **1b** with 2.5 equiv. of HBF_4*Et_2O. Peaks of residual Et_2O and ^{t}BuOH are marked with an asterisk and a hash, respectively.

Deprotonation of 2

Formation of 2a in benzene-d_6

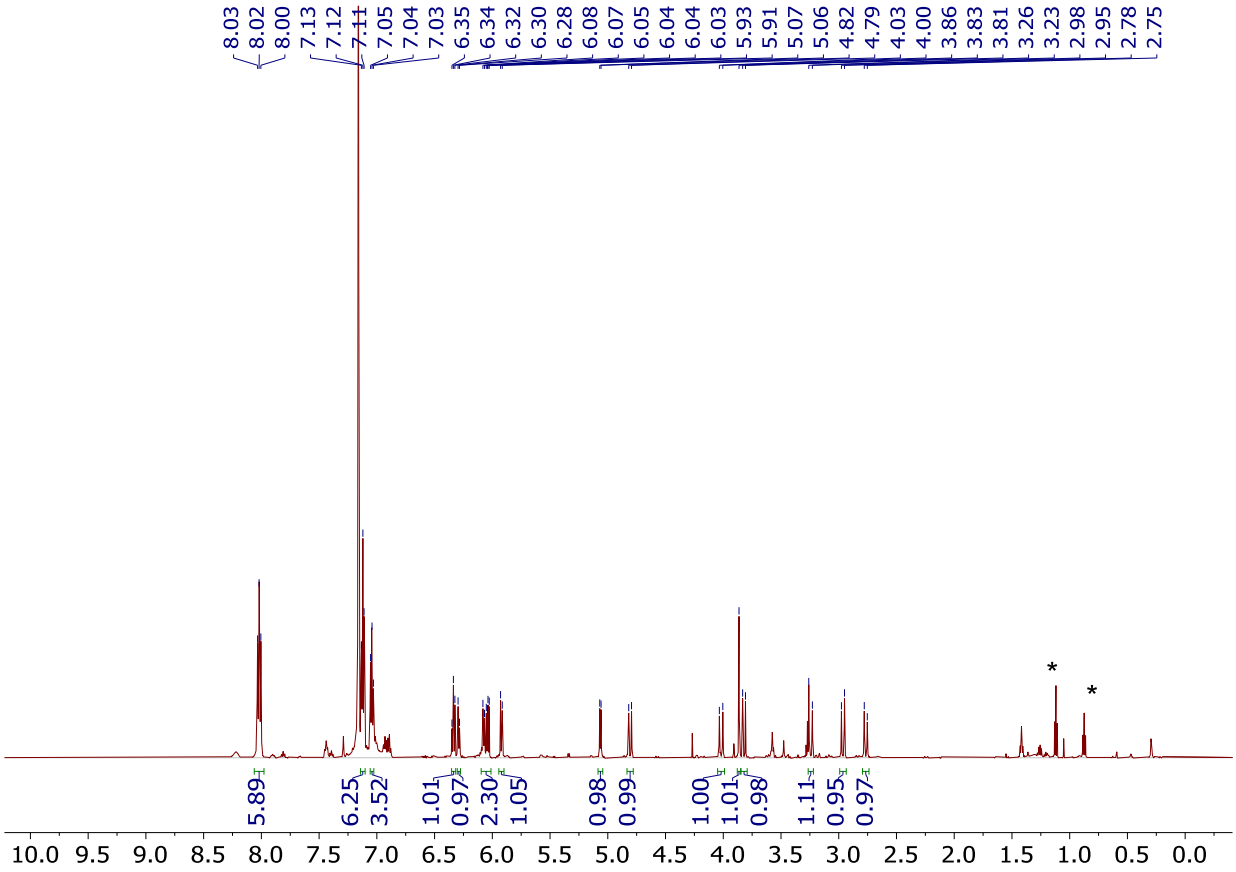

Figure S46. ^{1}H NMR spectrum of **2a** formed by deprotonation of **2** with 1.8 equiv of KO^{t}Bu in C_6D_6 at 23 °C. Peaks of residual pentane and diethyl ether are marked with an asterisk.

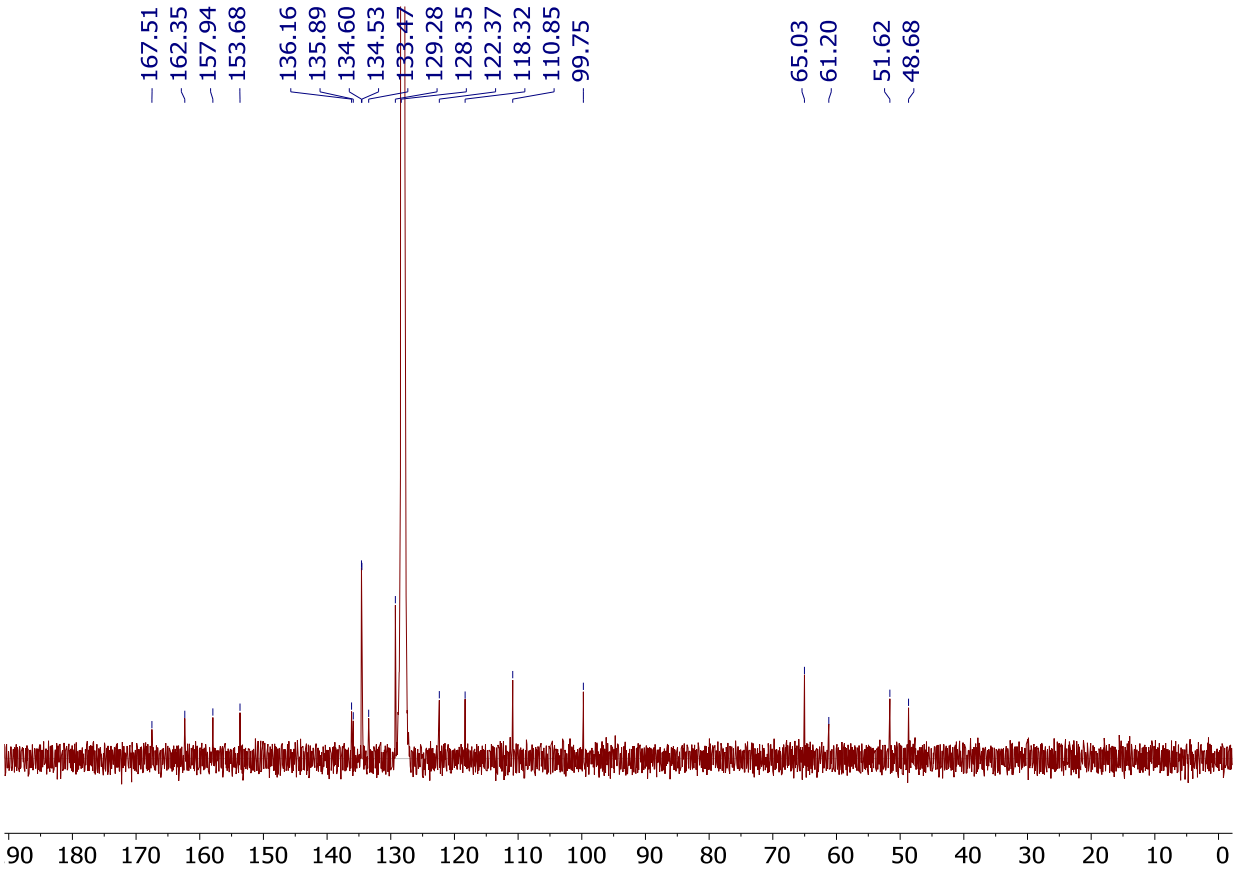

Figure S47. $^{13}C\{^{1}H\}$ NMR spectrum of **2a** formed by deprotonation of **2** with 1.1 equiv of KOtBu in C_6D_6 at 23 °C.

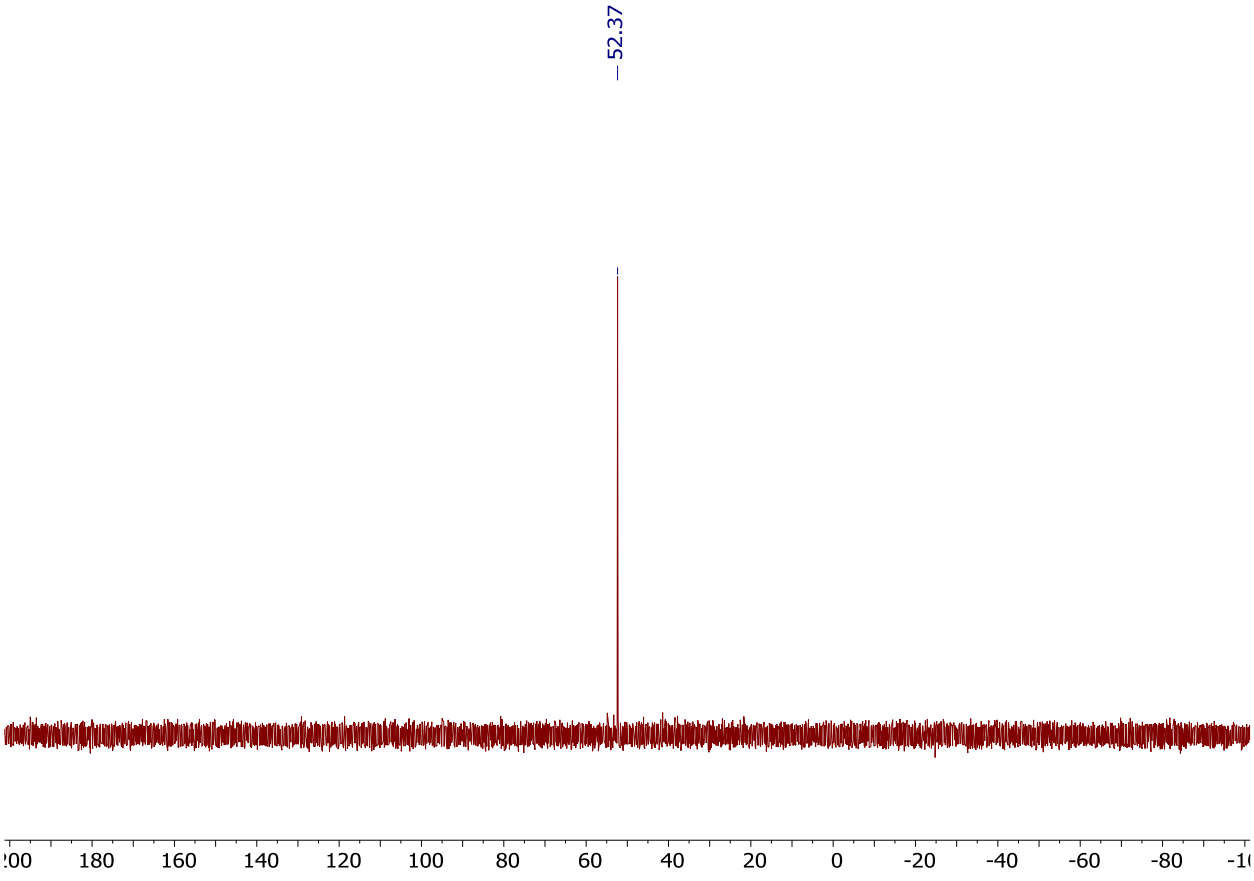

Figure S48. $^{31}P\{^{1}H\}$ NMR spectrum of **2a** in C_6D_6 at 23 °C.

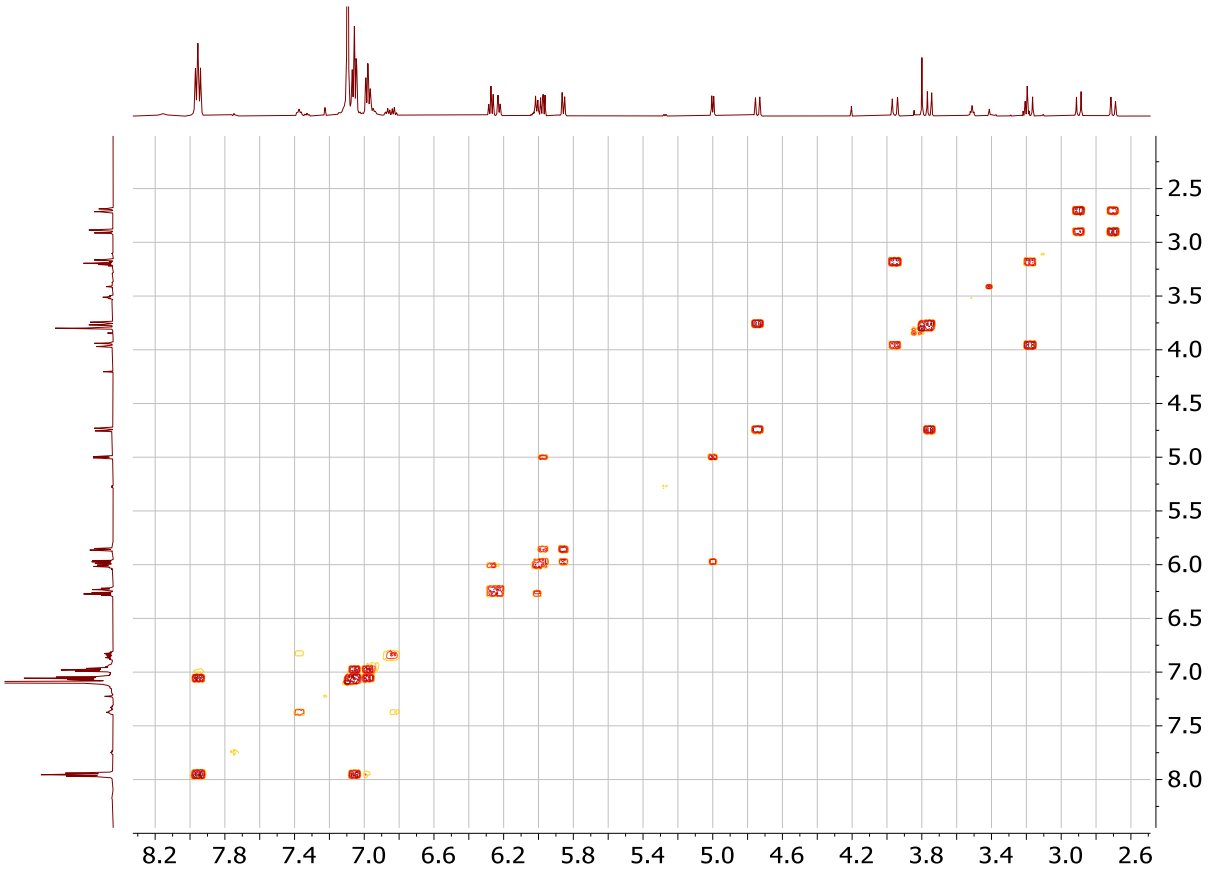

Figure S49. ^{1}H-^{1}H COSY spectrum of **2a** in C_6D_6 at 23 °C.

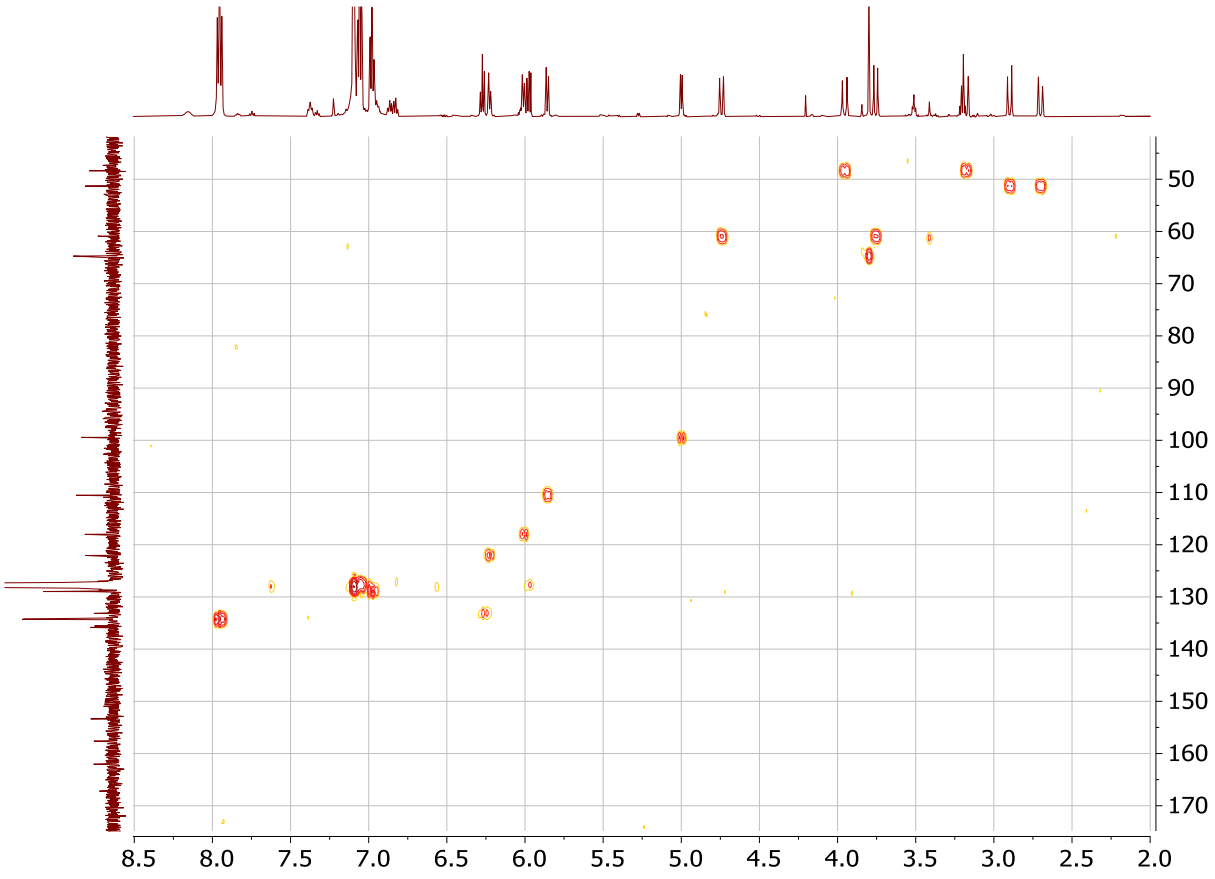

Figure S50. ^{1}H - ^{13}C HMQC spectrum of **2a** in C_6D_6 at 23 °C.

NMR yield determination of 2a

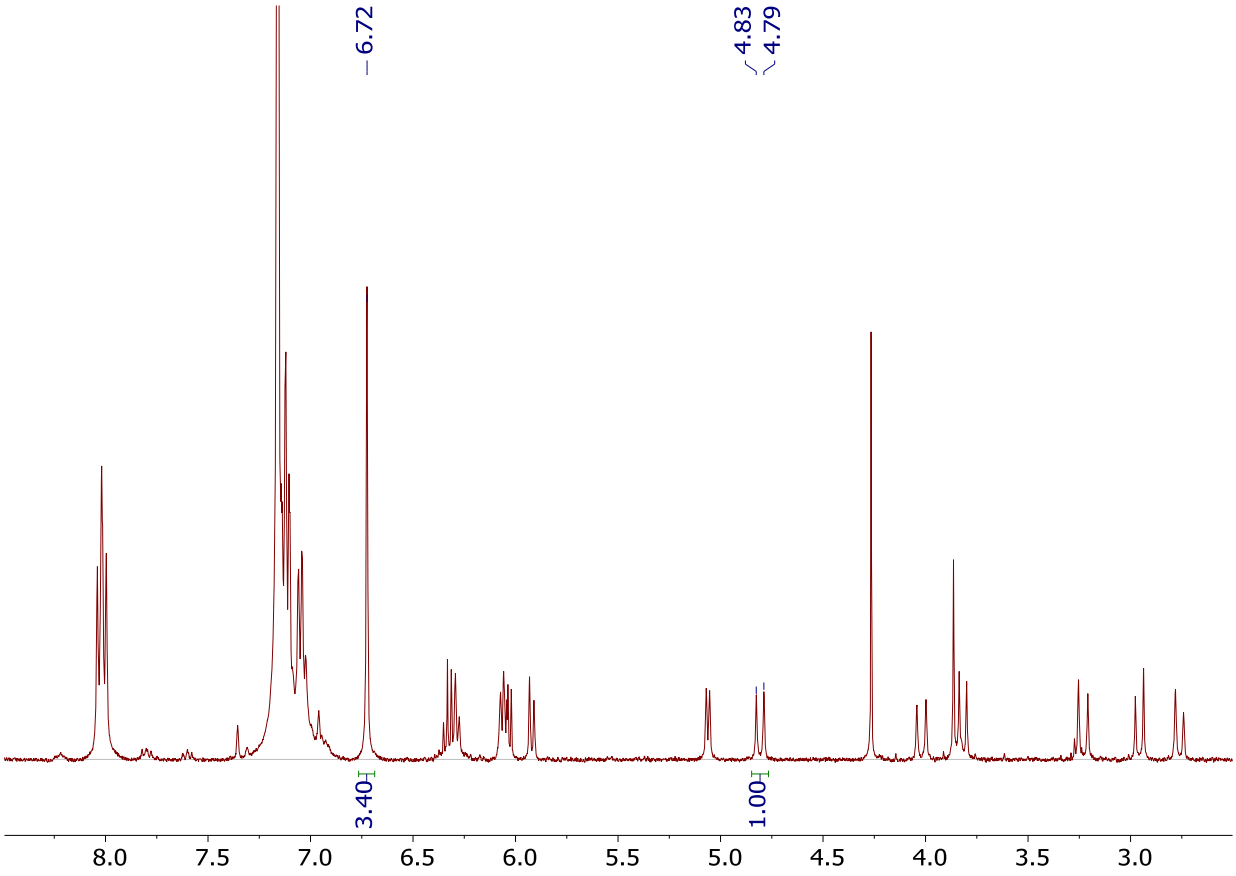

Figure S51. ^{1}H NMR spectrum of **2a** obtained by reacting **2** with 1.1 equivalents of KO^{t}Bu in benzene-d_6 after 60 min.

Protonation of 2a

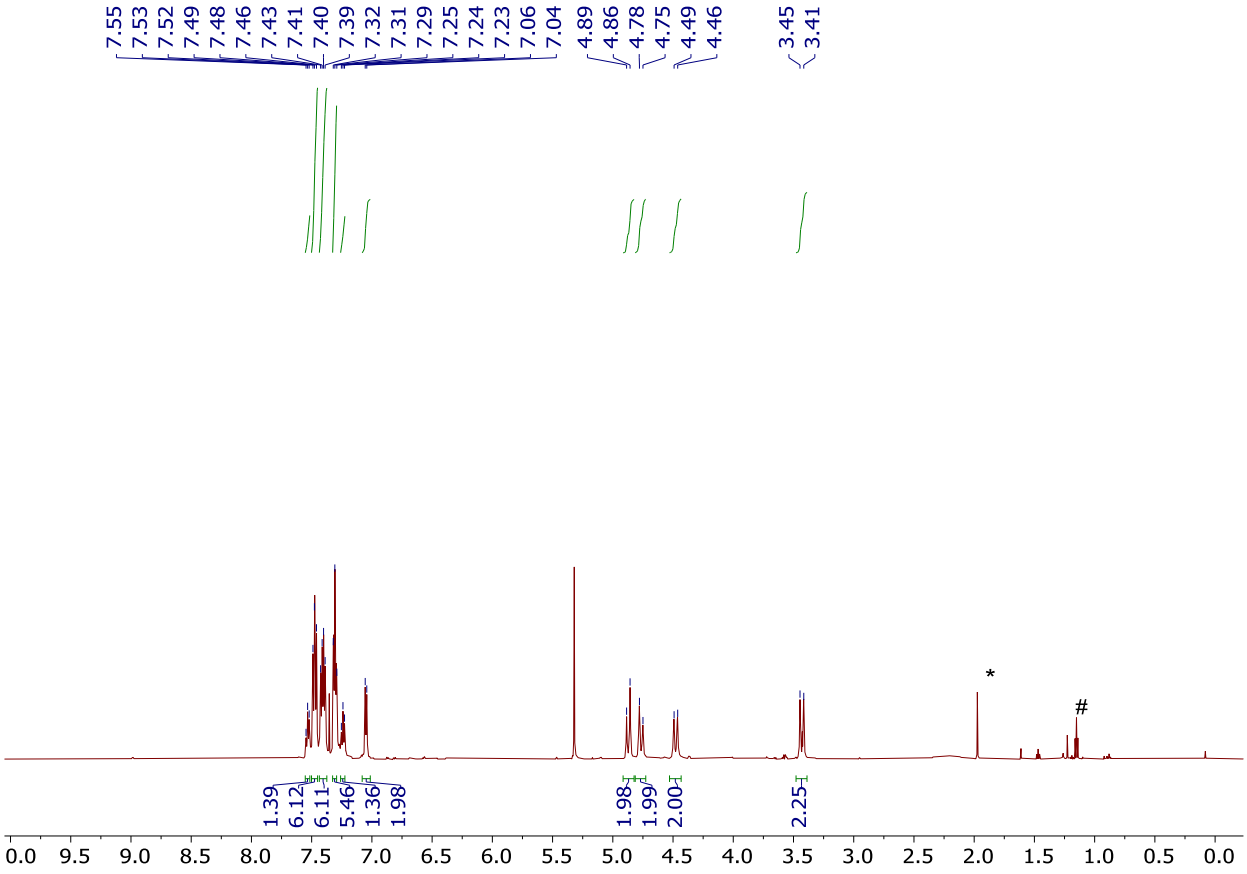

Figure S52. ^{1}H NMR spectrum of the product of protonation of **2a** with 1.1 equiv. of HBF_4*Et_2O. Peaks of residual acetonitrile and Et_2O are marked with an asterisk and a hash, respectively.

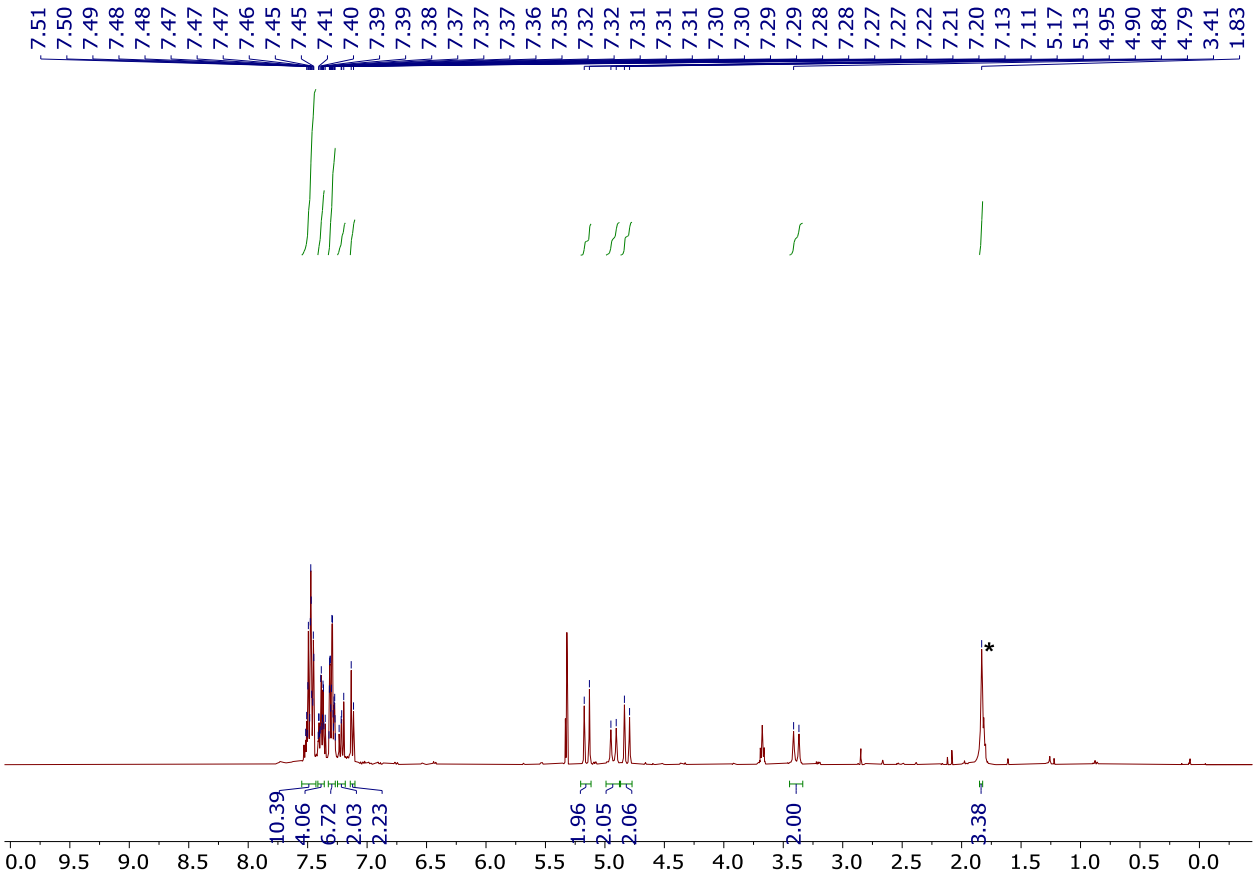

Figure S53. ^{1}H NMR spectrum of the product of protonation of **2a** with 1.1 equiv. of acetic acid. Peak of acetate counter anion is marked with an asterisk.

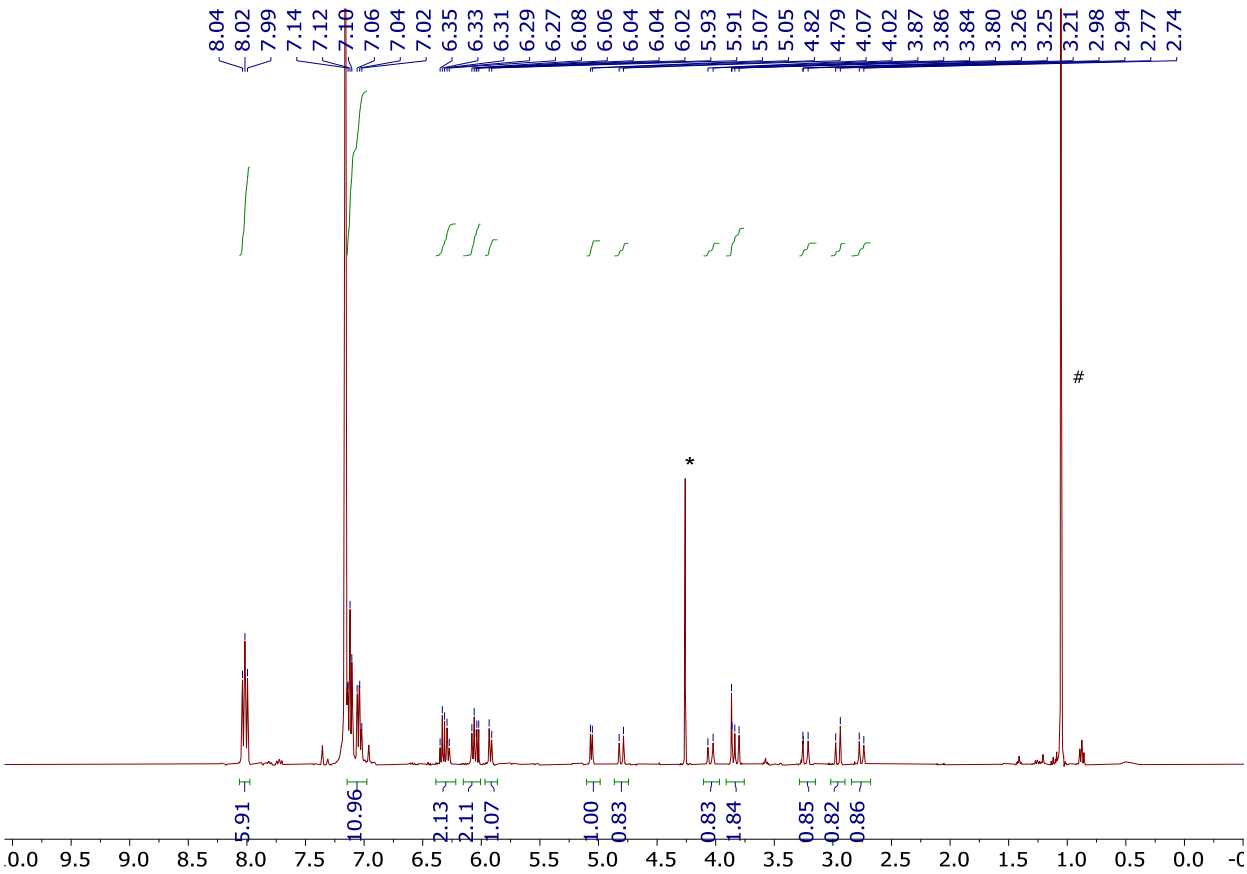

Figure S54. ^{1}H NMR spectrum of **2a** in benzene-d_6, with the presence of 1.1 equiv. of methanol-d_4. Peaks of residual dichloromethane and ^{t}BuOH are marked with an asterisk and a hash, respectively.

Deprotonation of complex 3

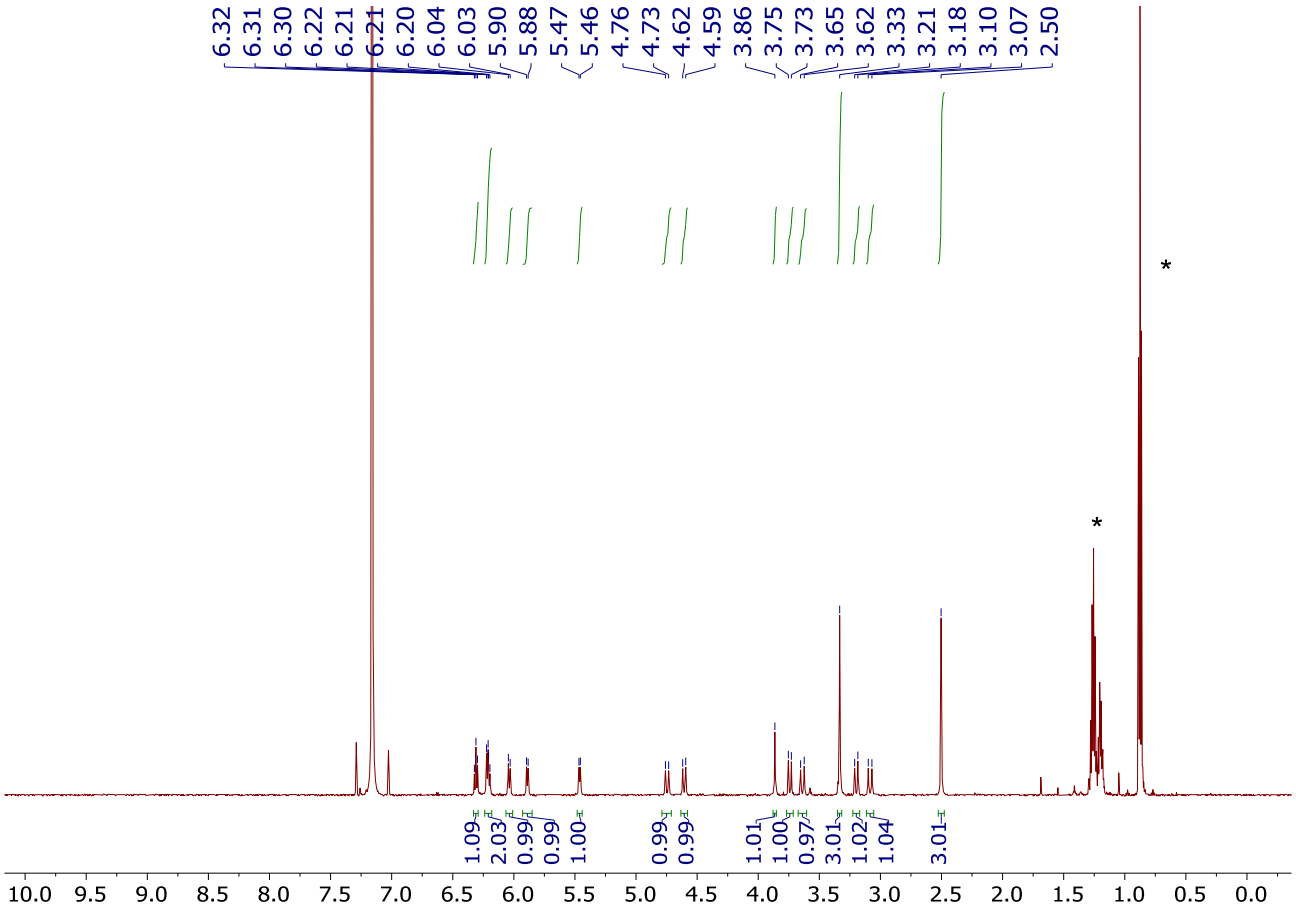

Figure S55. ^{1}H NMR spectrum of **3a** in benzene-d_6. Peaks of residual pentane are marked with an asterisk.

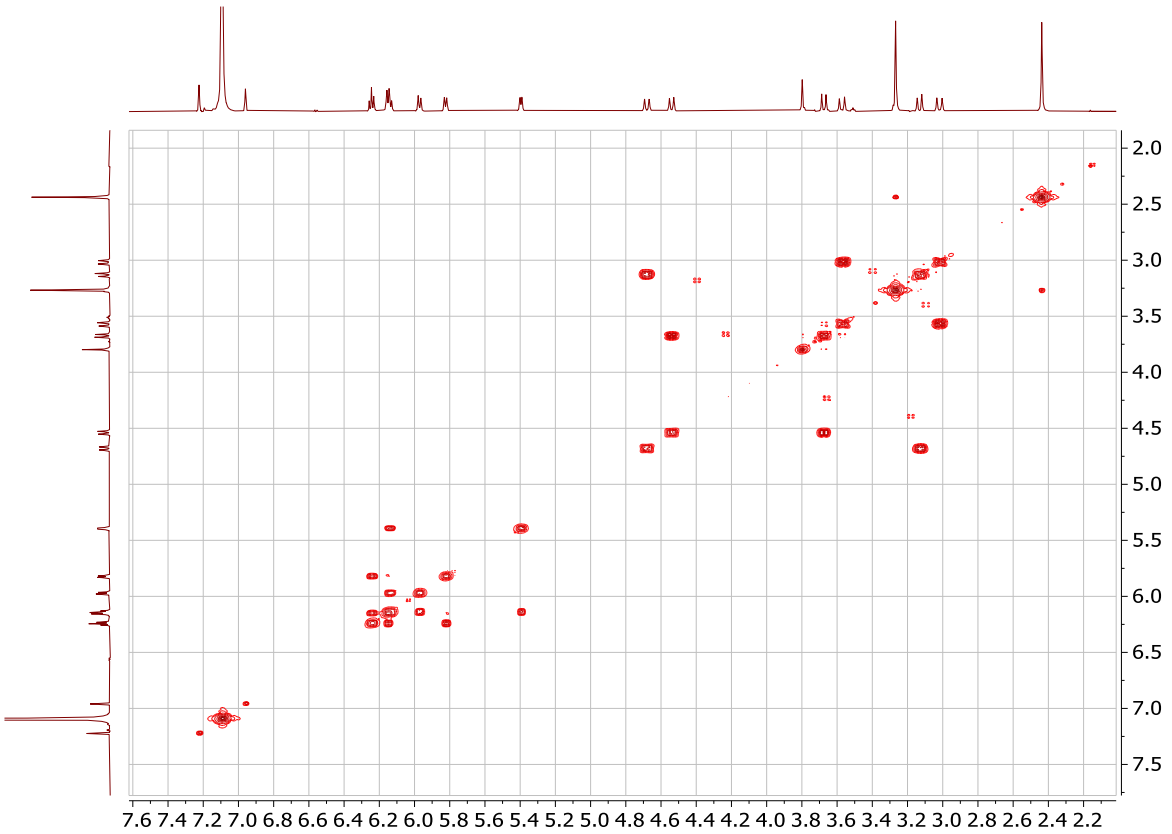

Figure S56. ^{1}H-^{1}H COSY spectrum of **3a** in benzene-d_6 at 23 °C.

NMR yield determination for the formation of 3a

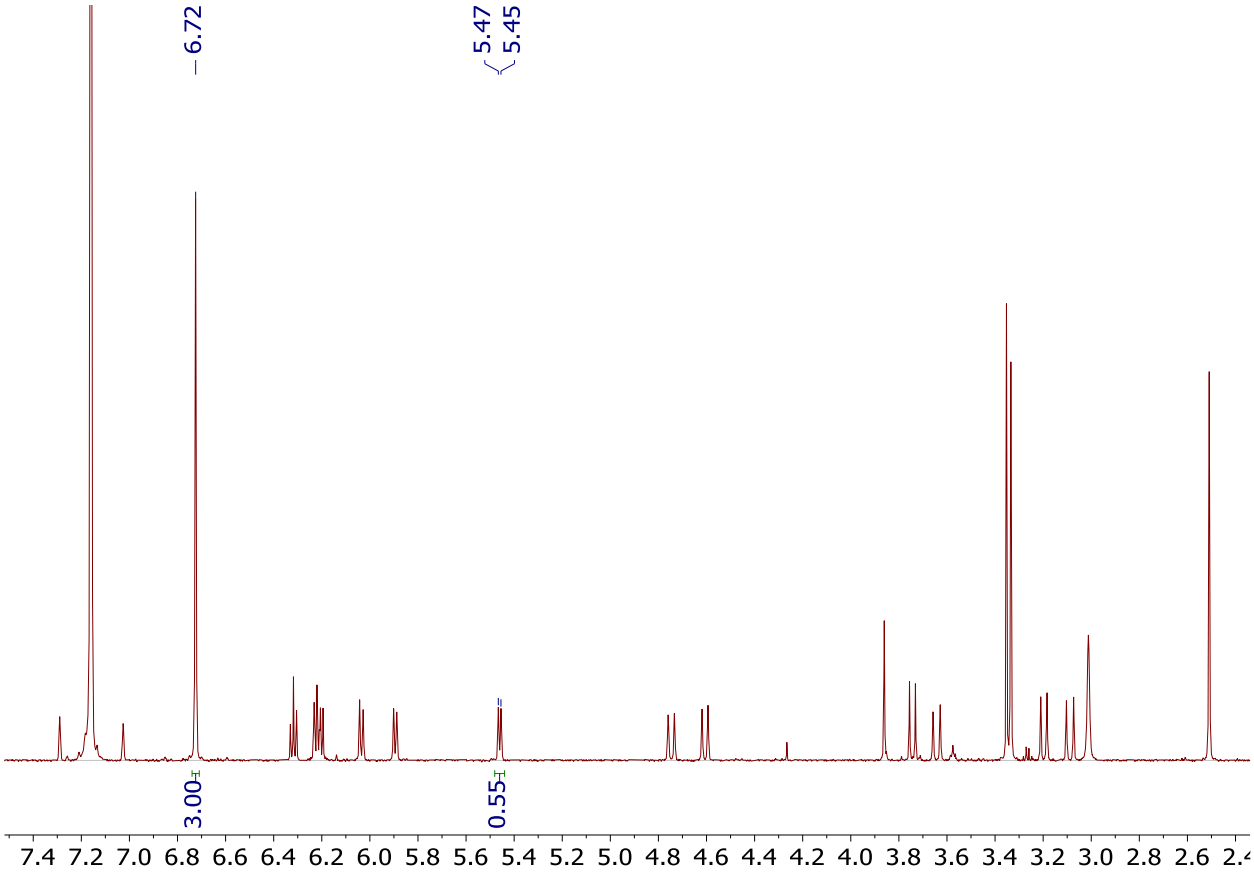

Figure S57. ^{1}H NMR spectrum of **3a** obtained by reacting **3** with 1.1 equivalents of KO^{t}Bu in benzene-d_6 after 60 min.

Protonation of 3a

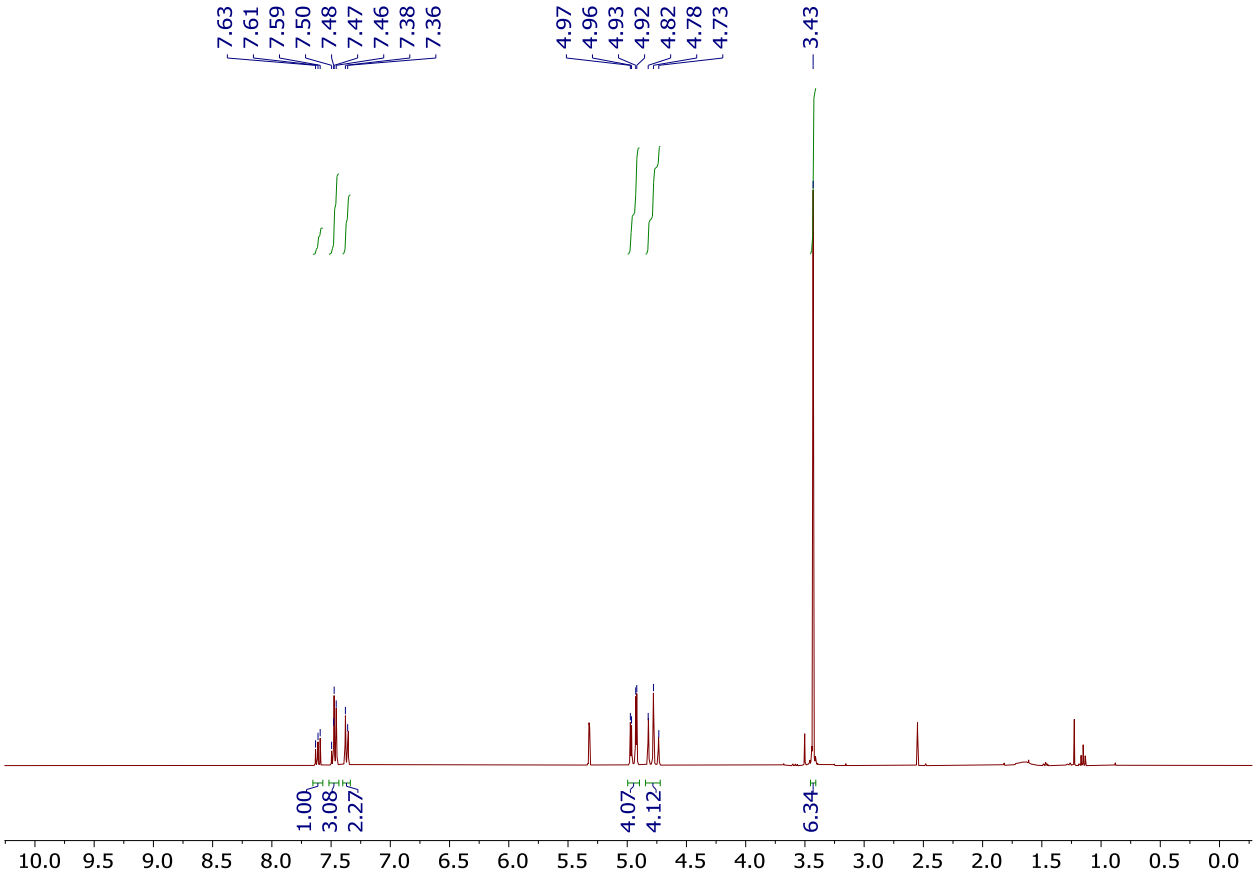

Figure S58. ^{1}H NMR spectrum of the product of protonation of **3a** with 1.1 equiv. of HBF_4*Et_2O.

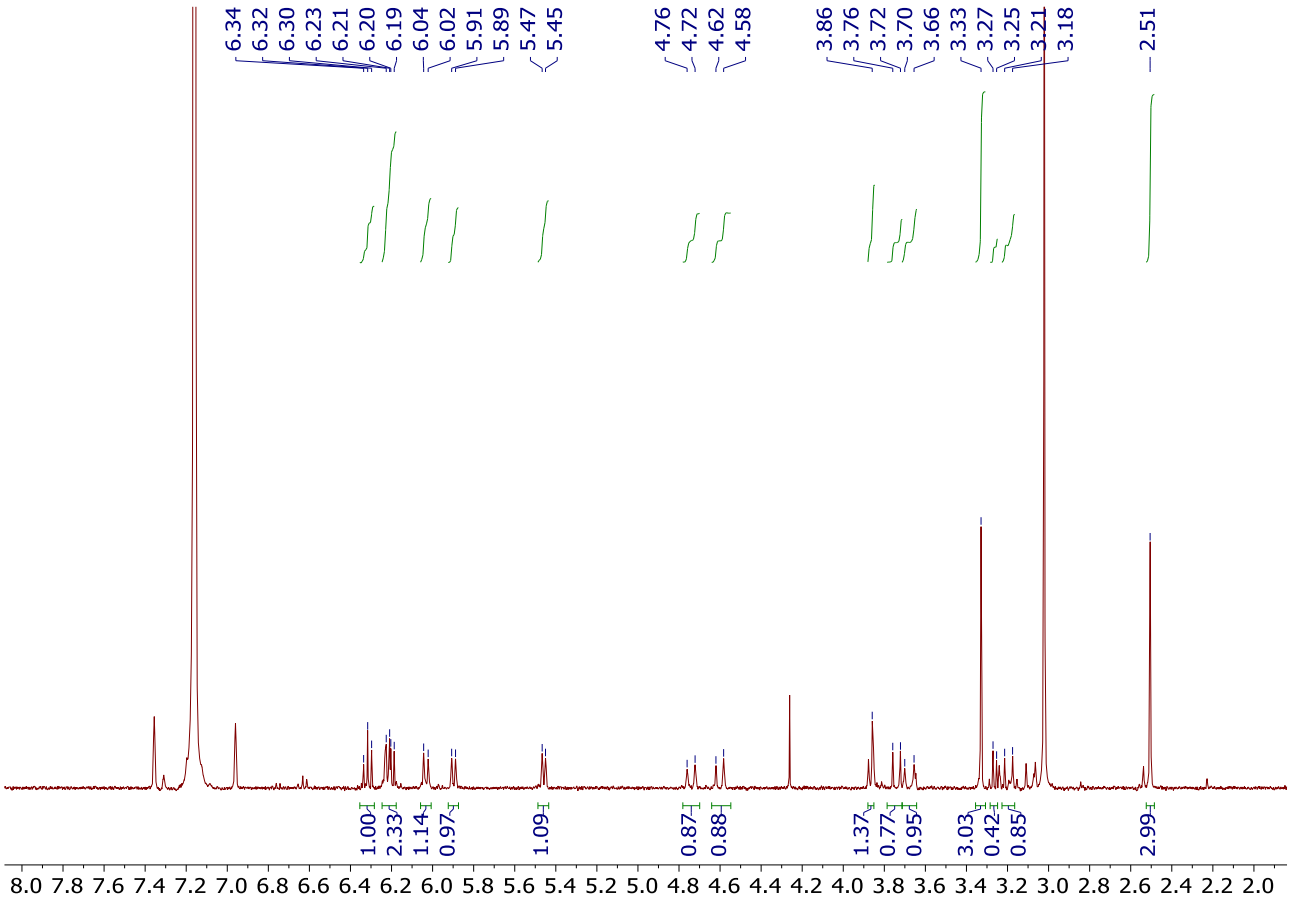

Figure S59. ^{1}H NMR spectrum of **3a** in benzene-d_6, with the presence of 1.1 equiv. of methanol-d_4.

Deprotonation of complex 4

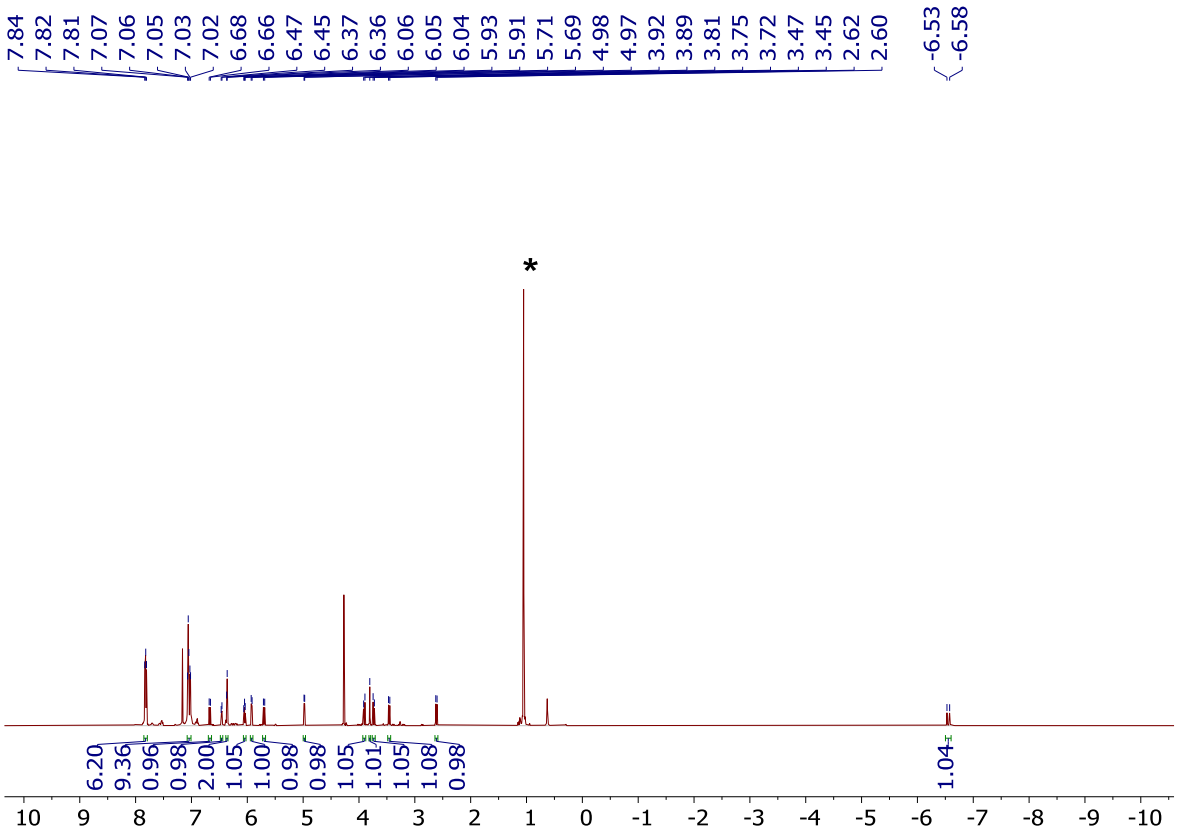

Figure S60. ^{1}H NMR spectrum of **4a** obtained by reacting **4** with 1.1 equivalents of KO^{t}Bu in C_6D_6 at 23 °C. Peak of ^{t}BuOH is marked with an asterisk.

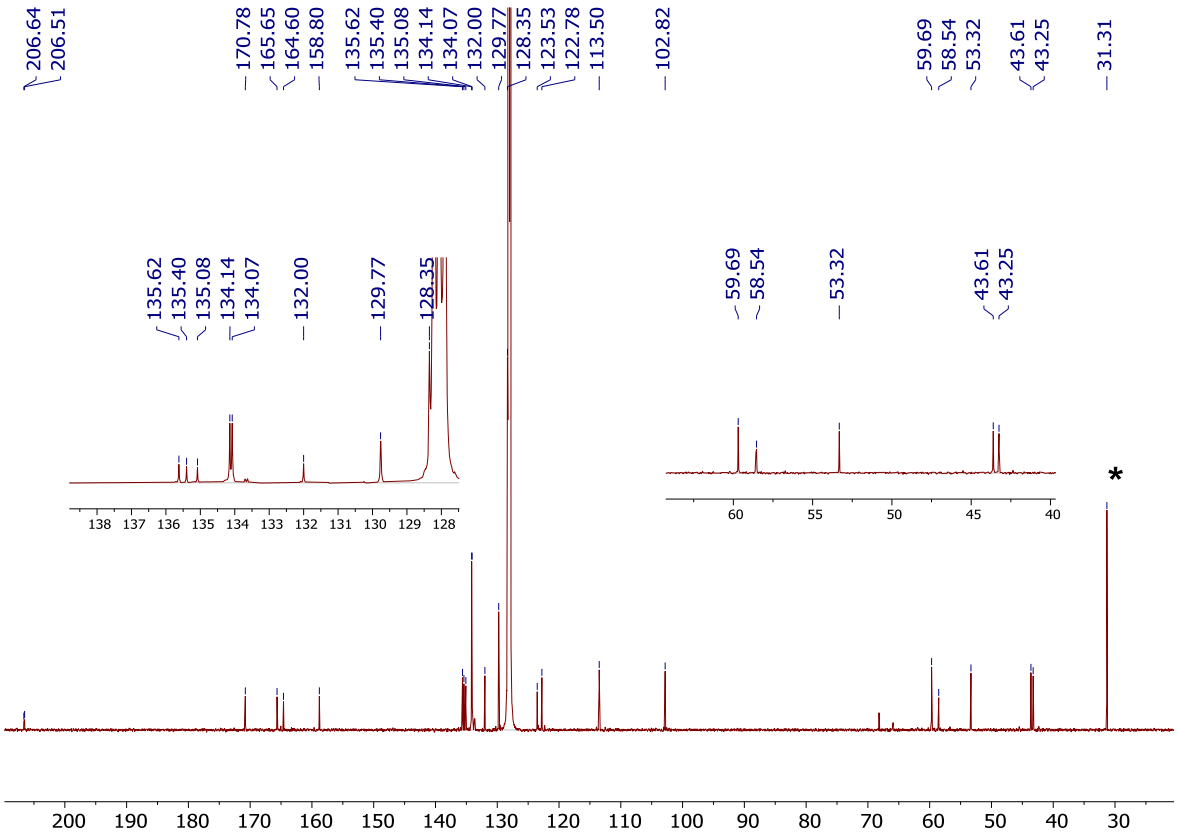

Figure S61. ^{13}C{^{1}H} NMR spectrum of **4a** obtained by reacting **4** with 1.1 equivalents of KO^{t}Bu in C_6D_6 at 23 °C. Peaks of residual ^{t}BuOH are marked with an asterisk.

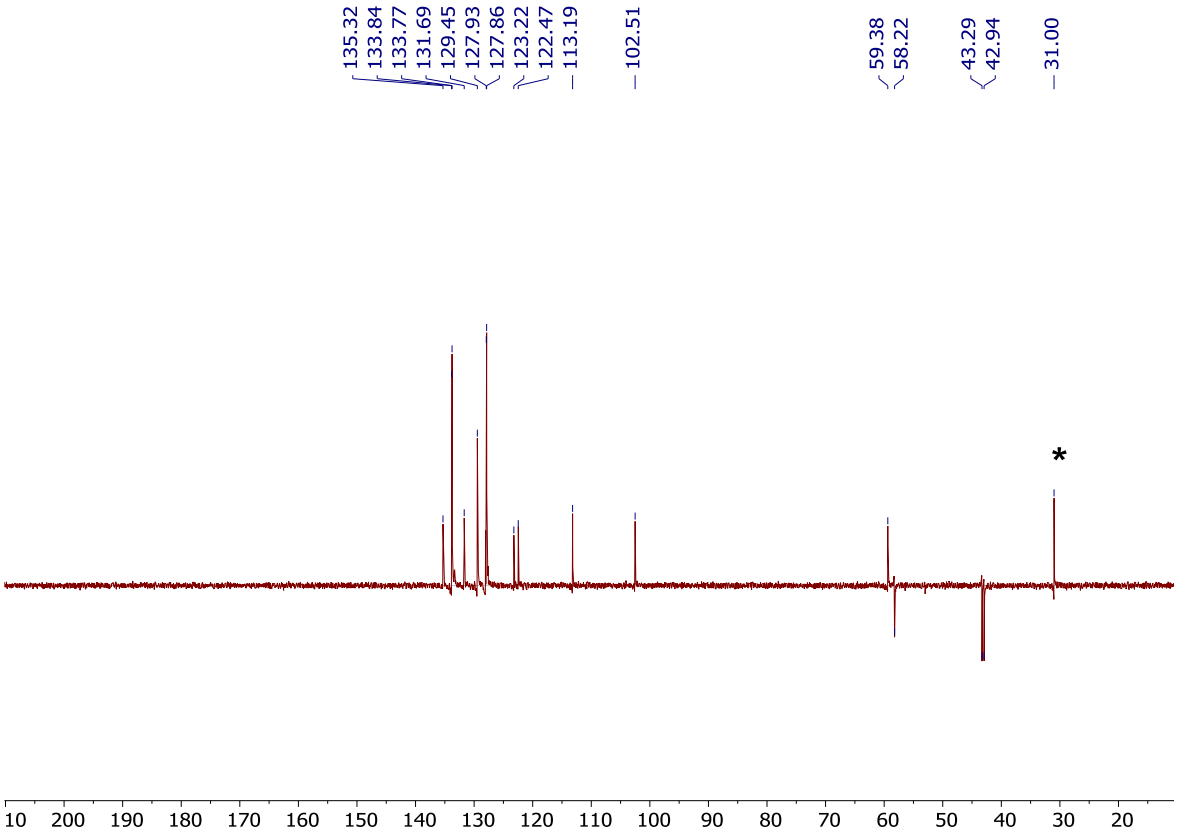

Figure S62. DEPT-135 NMR spectrum of **4a** obtained by reacting **4** with 1.1 equivalents of KO^{t}Bu in C_6D_6 at 23 °C. Peak of residual ^{t}BuOH is marked with an asterisk.

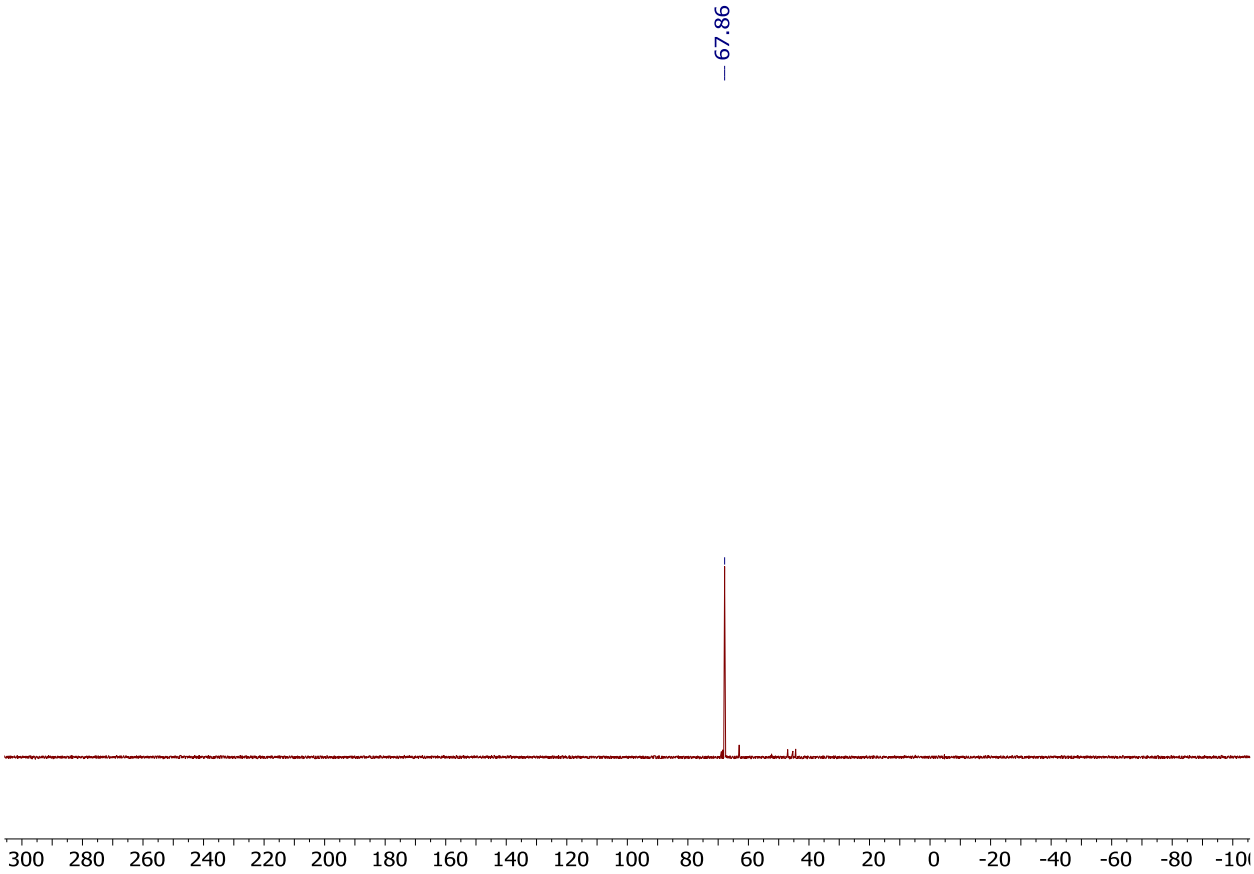

Figure S63. $^{31}P\{^1H\}$ NMR spectrum of **4a** obtained by reacting **4** with 1.1 equivalents of KO^{t}Bu in C_6D_6 at 23 °C.

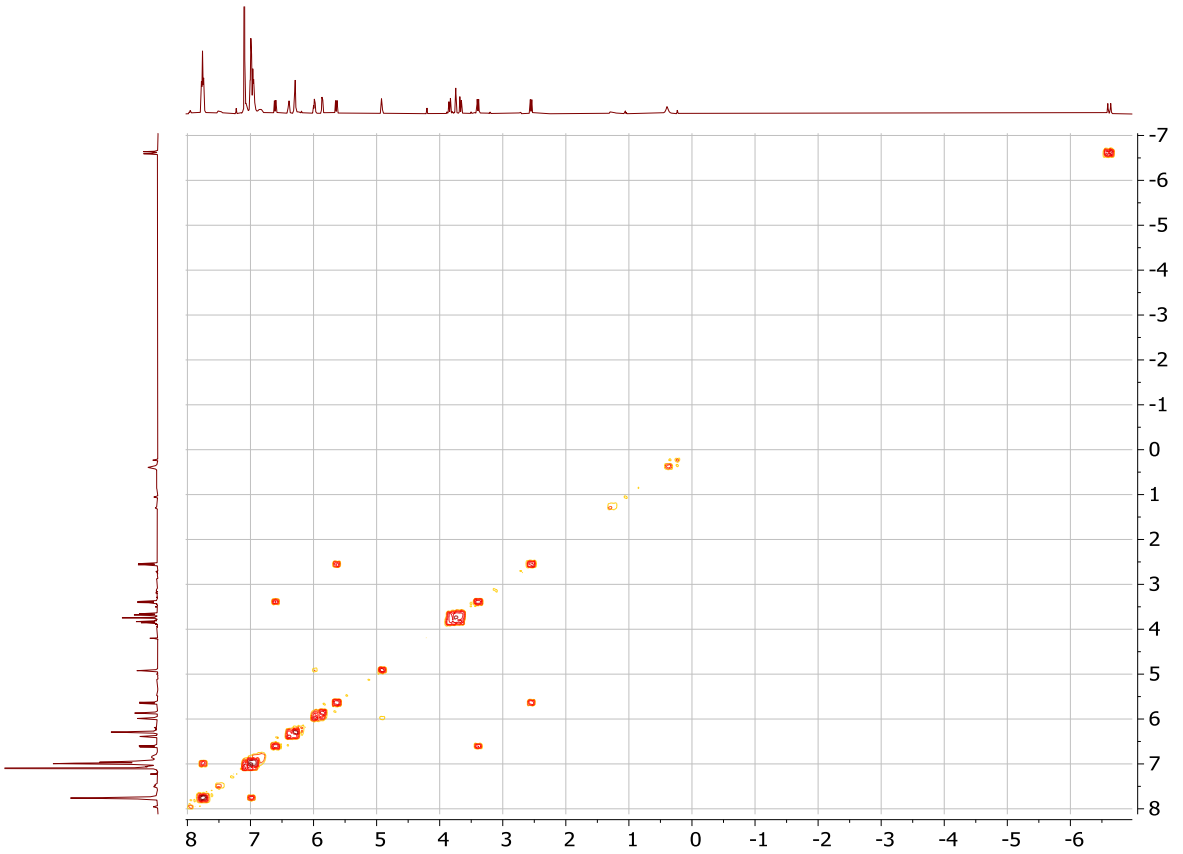

Figure S64. ^{1}H-^{1}H COSY spectrum of **4a** obtained by reacting **4** with 1.1 equivalents of KO^{t}Bu in C_6D_6 at 23 °C.

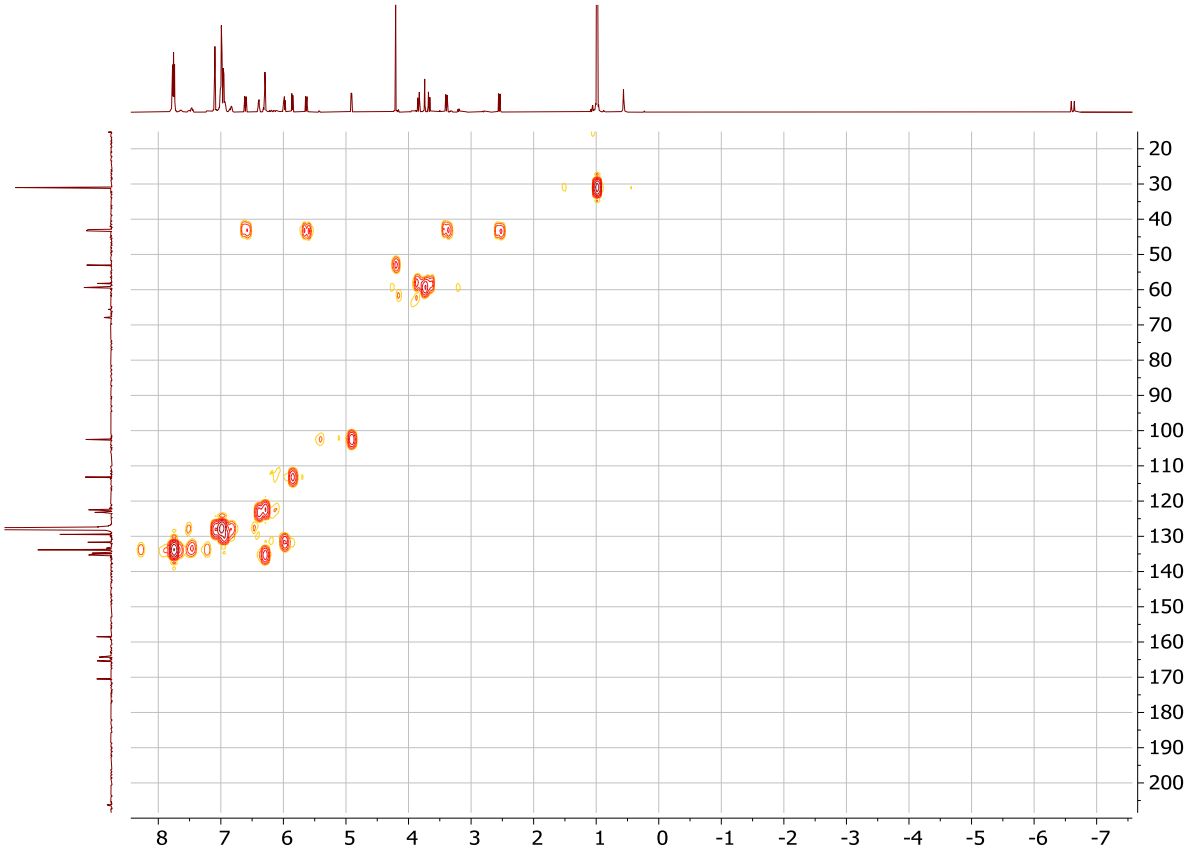

Figure S65. ^{1}H-^{13}C HMQC spectrum of **4a** obtained by reacting **4** with 1.1 equivalents of KO^{t}Bu in C_6D_6 at 23 °C.

NMR yield determination for the deprotonation reaction of 4

Table S1. The NMR yield of **4a** in the presence of variable amounts of KO^{t}Bu.

Entry	Equiv of KO^{t}Bu	NMR yield after 60 min (%)
1	1.1	99
2	2.0	96
3	3.0	99
4	4.0	77

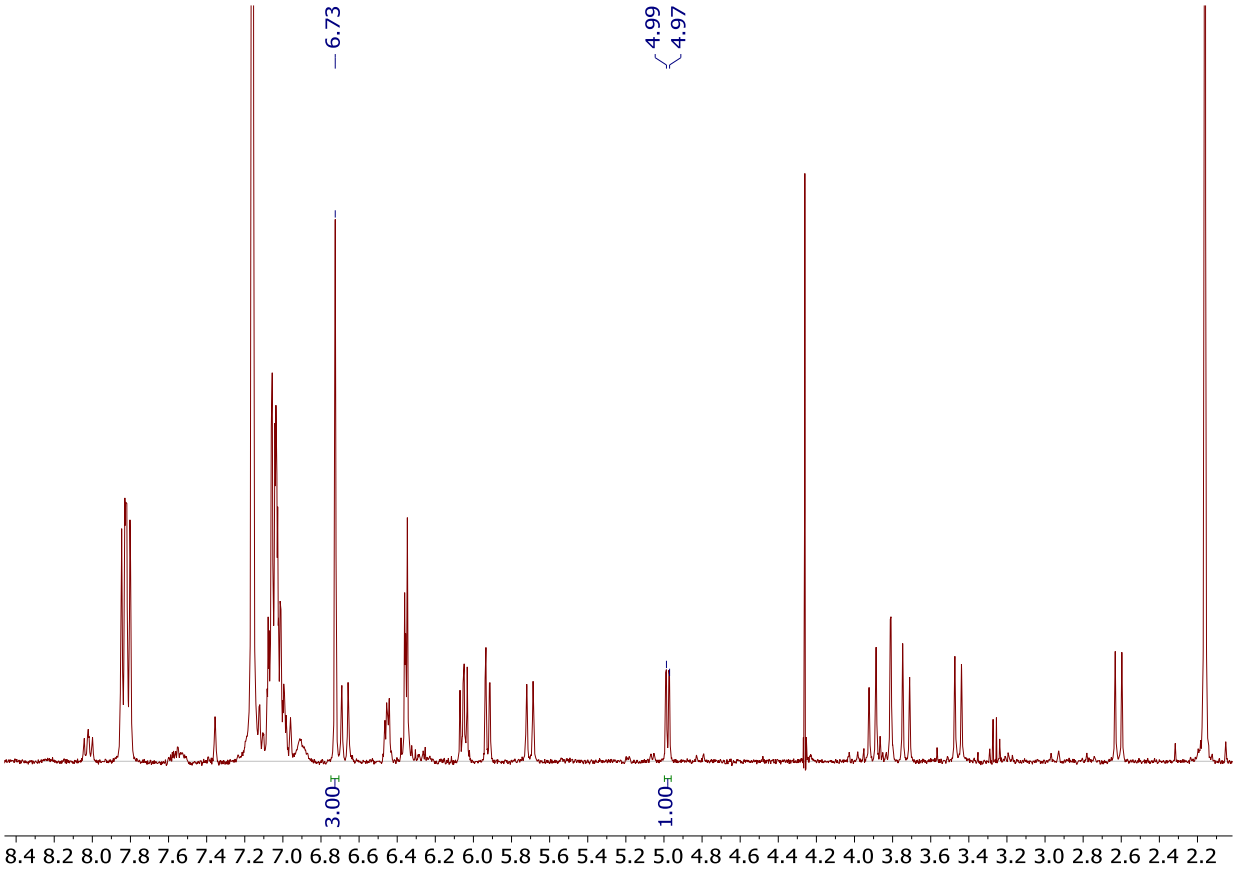

Figure S66. ^{1}H NMR spectrum of **4a** obtained by reacting **4** with 1.1 equiv. of KO^{t}Bu after 60 min.

Protonation of 4a

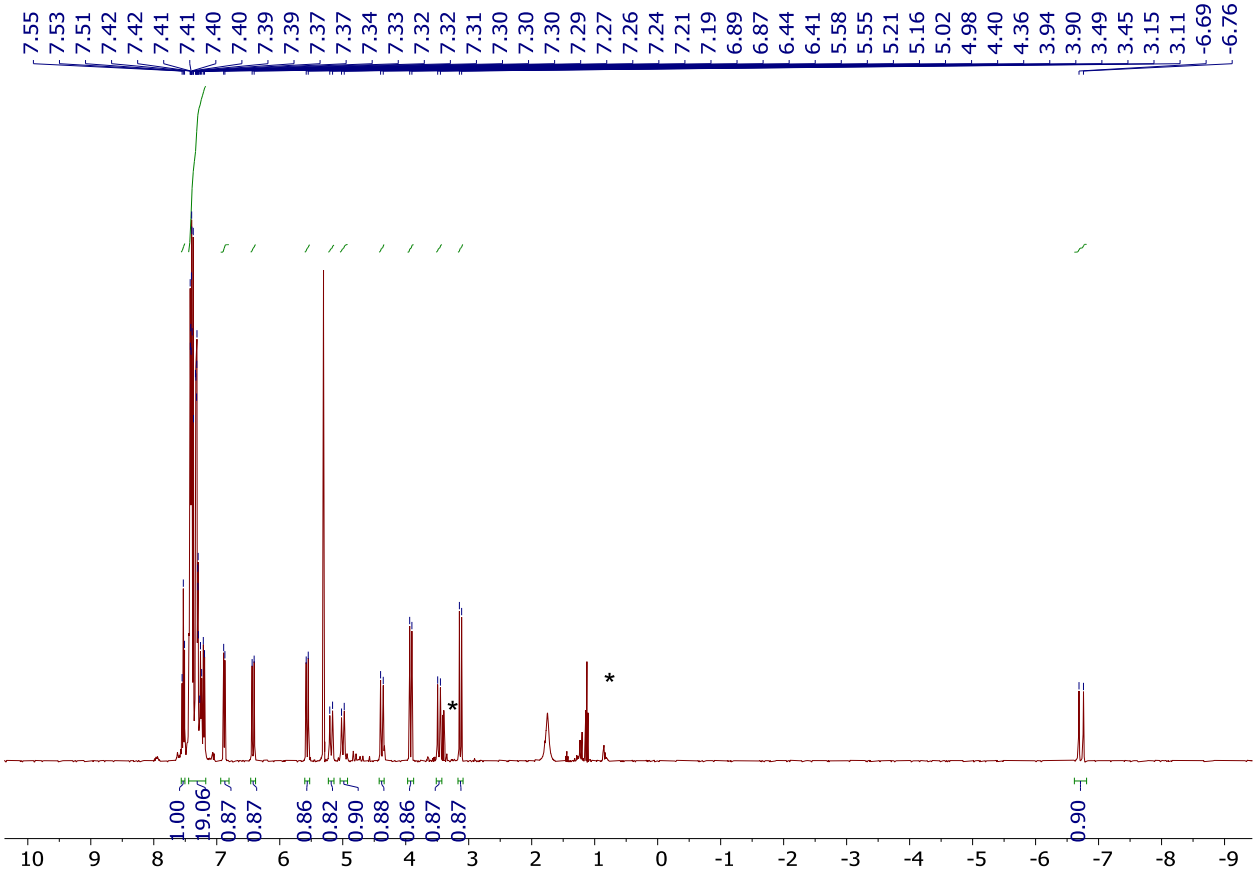

Figure S67. ^{1}H NMR spectrum of the product of protonation of **4a** with 1.1 equiv. of HBF_4*Et_2O. Peaks of residue Et_2O are marked by an asterisk. (Complex **4a** was obtained by treatment of **4** with 1.1 equiv o KO^{t}Bu *in situ*).

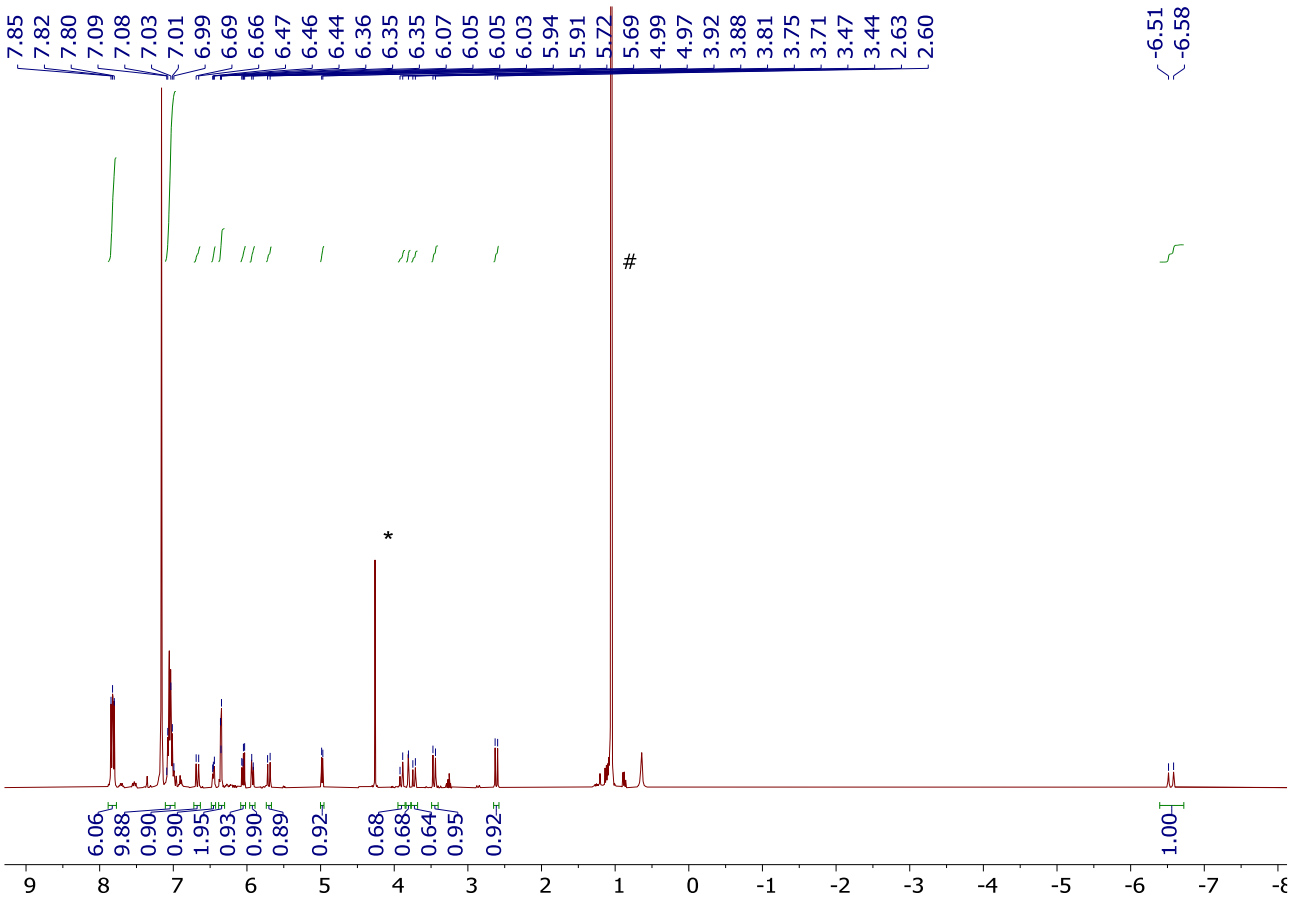

Figure S68. ^{1}H NMR spectrum of **4a** in benzene-d_6, with the presence of 1.1 equiv. of methanol-d_4. Peaks of residue dichloromethane and ^{t}BuOH are maked with an asterisk and a hash, respectively.

Complex 5

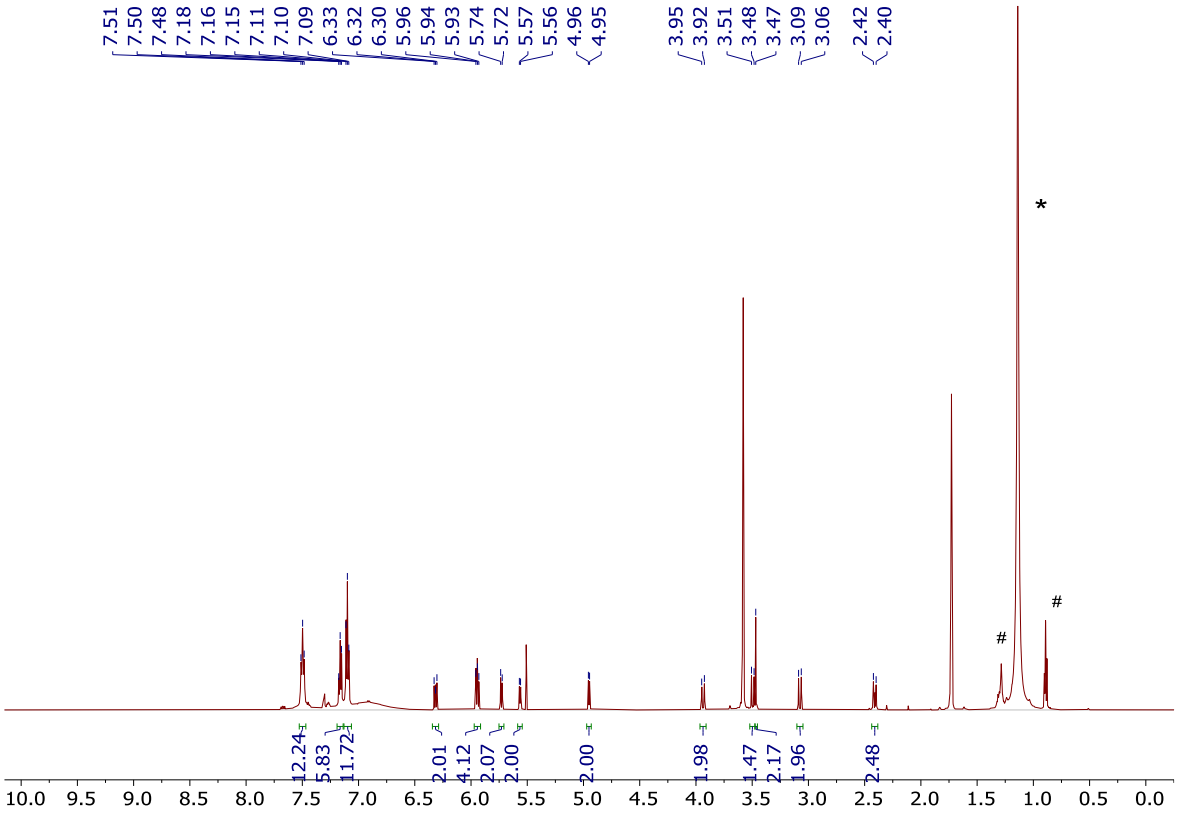

Figure S69. ^{1}H NMR spectrum of **5** in THF-d_8 at 23 °C. Peaks of residual ^{t}BuOH and pentane are marked with an asterisk and a hash, respectively.

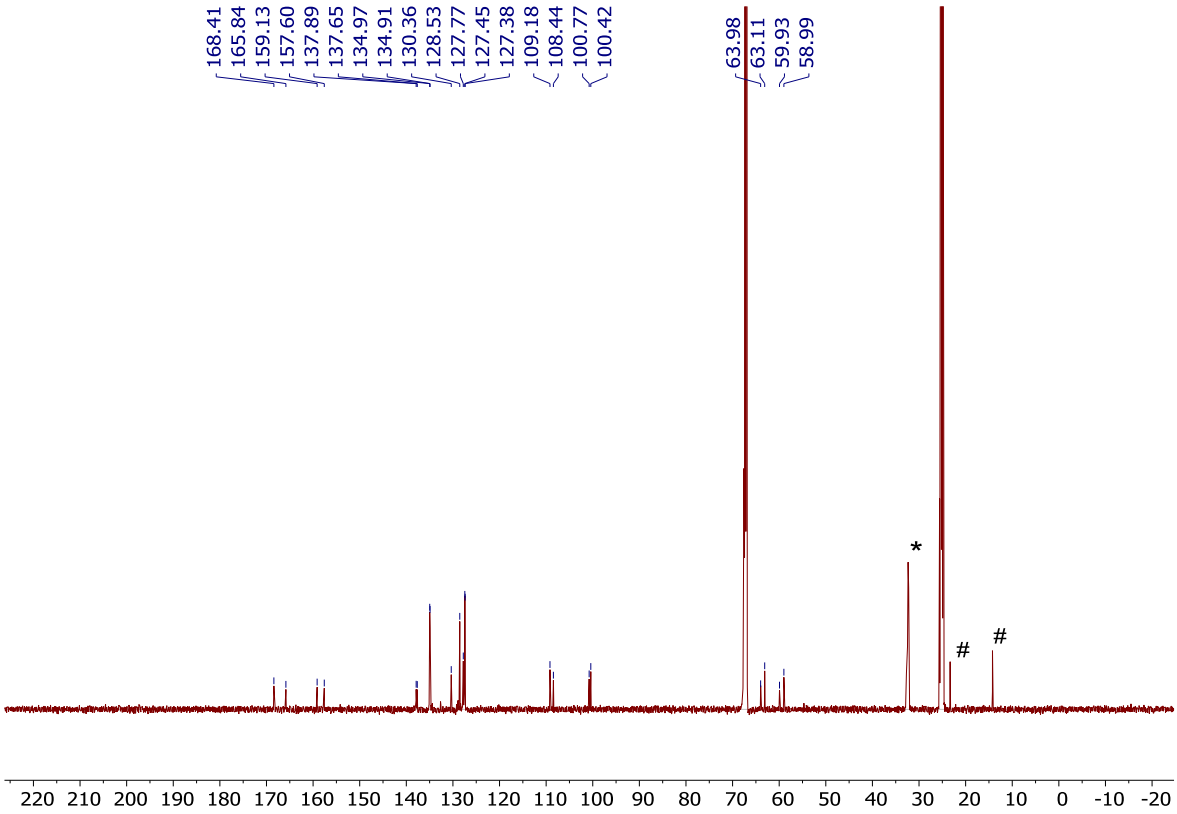

Figure S70. ^{13}C{^{1}H} NMR spectrum of **5** in THF-d_8 at 23 °C. Peaks of residual ^{t}BuOH and pentane are marked with an asterisk and a hash, respectively.

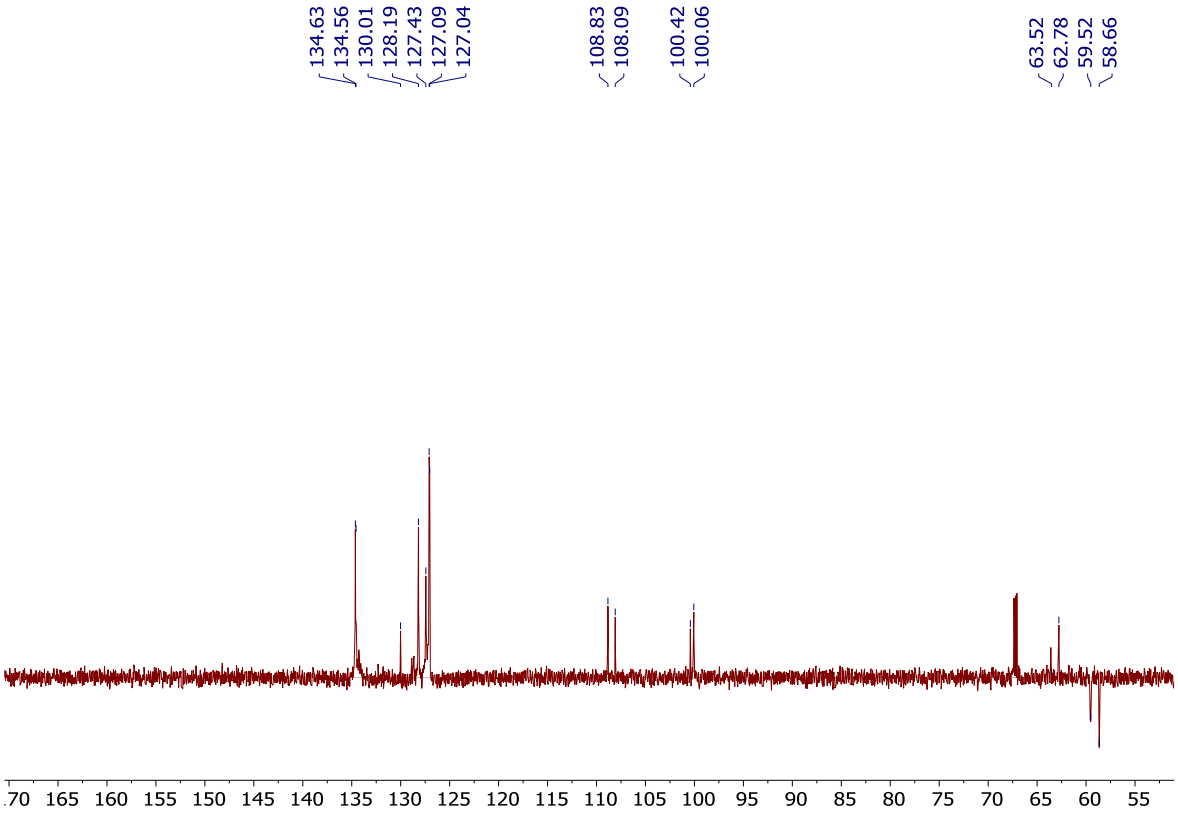

Figure S71. DEPT-135 NMR spectrum of **5** in THF-d_8 at 23 °C.

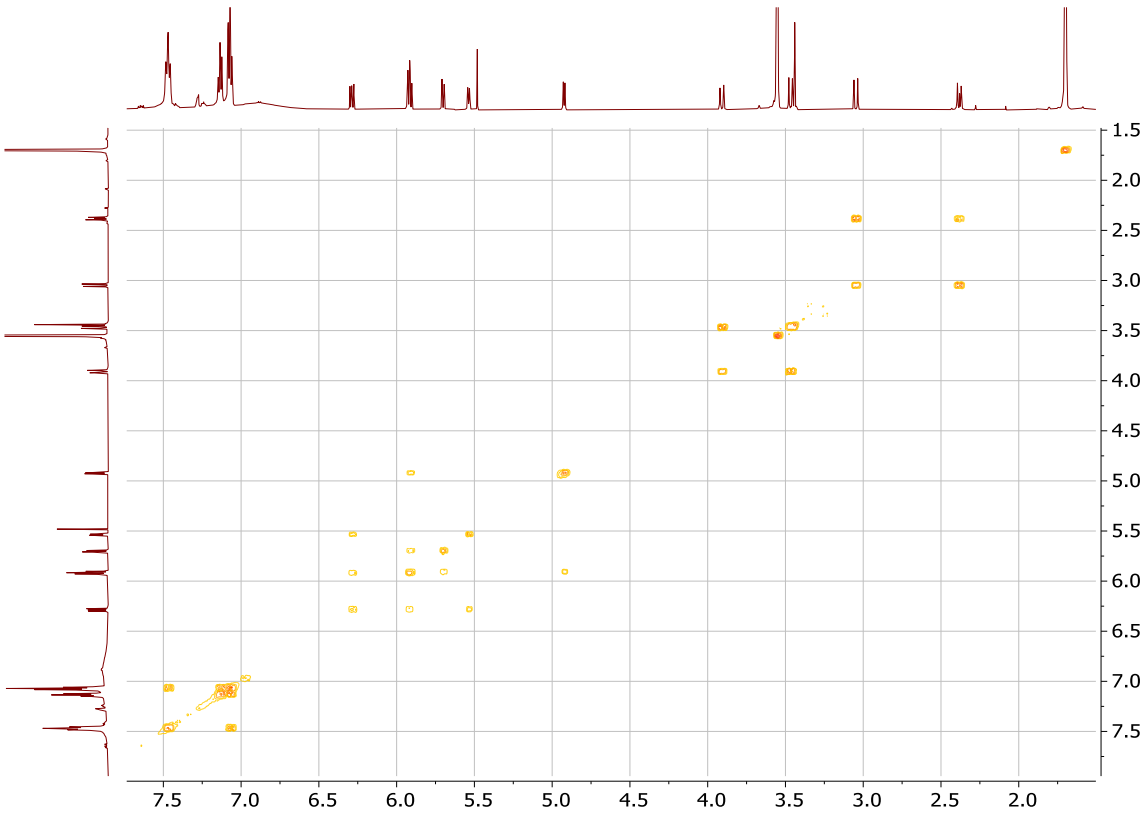

Figure S72. ^{1}H-^{1}H COSY NMR spectrum of **5** in THF-d_8 at 23 °C.

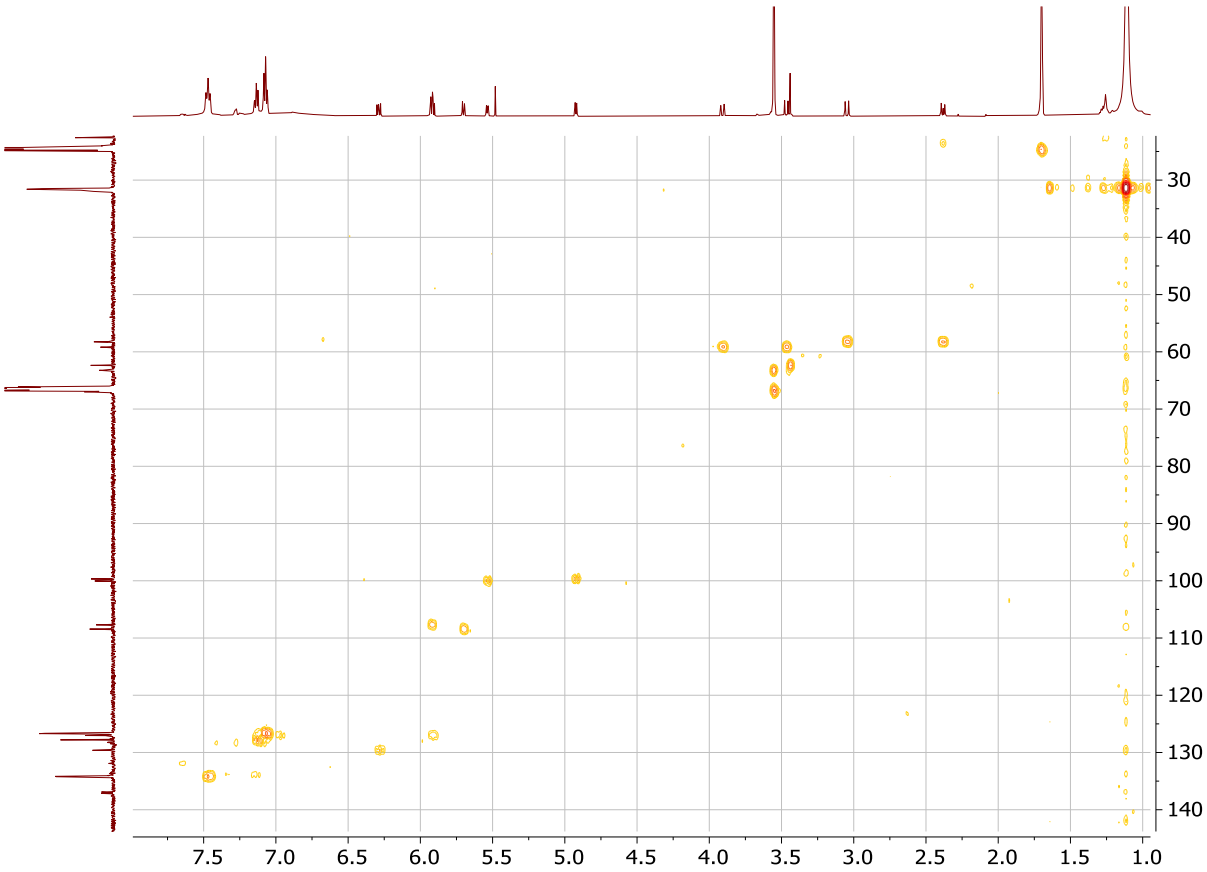

Figure S73. ^{1}H-^{13}C HMQC NMR spectrum of **5** in THF-d_8 at 23 °C.

3. Reactivity tests

Attempted reactivity with H_2, CO_2, CS_2 and phenylacetylene

The solution of **1b** and **2a** was prepared *in situ* and immediately used for reactivity studies.

- Generation of **1b** *in situ*: 5.0 mg (0.0065 mmol) of **1** was mixed with 1.5 mg (0.013 mmol – 2 equivalents) of KO^{t}Bu in 0.7 mL of toluene-d_8. The mixture was allowed to stir for 20 min, at which time the color gradually changed to yellowish-orange. The mixture was then filtered through celite to generate **1b.**

- Generation of **2a** *in situ*: 5.0 mg (0.007 mmol) of **2** was mixed with 0.9 (0.008 mmol – 1.1 equiv) of KO^{t}Bu in 0.7 mL of benzene-d_6. The mixture was vigorously stirred in RT for 20 min to generate **2a**, at which time the solution color changed to orange.

a. Reactivity of **1b** and **2a** with H_2

The solution of pre-generated **1b** in a J. Young NMR tube was degassed by three freeze-pump-thaw cycles and then recharged with 1 atm of H_2 gas. No color change was found after charging with H_2. The mixture was analyzed by ^{1}H NMR, which showed no evidence of hydride complex formation/complex reprotonation.

Similarly, reaction of in-situ **2a** with 1 atm H_2 gas showed no evidence of any new product formation.

c. Reactivity of **1b** and **2a** with CO_2

The solution of **1b** in a J. Young NMR tube was degassed by three freeze-pump-thaw cycles and then recharged with 1 atm of CO_2 gas. The solution color was rapidly changed to colorless and the yellow precipitate was formed. The precipitate was collected and dissolved in methanol-d_4, which was showed a complexed mixture of products in ^{1}H NMR spectroscopy, which could not be recrystallized. Attempted dissolution in CH_2Cl_2 and acetonitrile produced black precipitate.

Reaction of **2a** with 1 atm of CO_2 resulted in a rapid formation of yellow precipitation, while the solution became colorless. The yellow precipitate was then collected and dissolved in CD_2Cl_2, which was showed a complex mixture of products by ^{1}H NMR spectroscopy, which could not be recrystallized.

d. Reactivity of **1b** and **2a** with CS_2

To the solution of **1b**, 4 µL (0.065 mmol – 10 equivalents) of CS_2 was added. The mixture was allowed to stir for 1 hour, and the dark red precipitation was formed. The red residue was dissolved in acetone-d_6, which showed a mixture of unidentified products, which could not be recrystallized.

Similarly, 4 µL (0.065 mmol – 10 equivalents) of CS_2 was added to the *in-situ* solution of **2a**, and the mixture was vigorously stirred for 1 hour. Orange precipitate was formed during the reaction, which was then dissolved in CD_2Cl_2. ^{1}H NMR spectroscopy showed a complex mixture of products, which was also failed to give single crystals.

e. Reactivity of **1b** and **2a** with phenylacetylene.

To a solution of **1b**, 0.7 µL (0.007 mmol – 1 equivalent) of phenylacetylene was added and the mixture was stirred at room temperature for 1 hour. The mixture was then analyzed by ^{1}H NMR spectroscopy, which showed only peaks of starting material without any evidence of phenylacetylene activation. Similarity, **2a** was unreactive with 1 equivalent of phenylacetylene.

Attempted catalytic reactivity

a. Attempted nitrile hydration of acetonitrile

In a glovebox, 5.8 mg (0.0075 mmol – 3 mol%) of complex **1** and 1.7 mg (0.015 mmol – 6 mol%) of KO^{t}Bu were added to 0.5 mL tert-butyl alcohol. The mixture was stirred for 20 min to yield **1b** *in situ*, then 13 µL (0.25 mL – 1 equiv.) of acetonitrile and 23 µL (1.25 mmol – 5 equiv.) were added to the solution. The mixture was transferred to an 11 mL screw-cap vial and sealed with electrical tape (to prevent gas exchange). The

reaction mixture was taken out of the glovebox and stirred for 24 h at RT or 80 °C. After heating, the reaction mixture was exposed to air, and the solvent was removed under vacuum. The residue gave no signal of amide formation which was confirmed by GC-MS and ^{1}H NMR spectroscopy.

b. Attempted dehydrogenation of benzyl alcohol

Complex **1** (20.7 mg, 0.0274 mmol) was suspended in 8.0 mL of toluene in a 25 mL Schlenk tube equipped with a stirrer bar. ^{t}BuOK (3.5 mg, 0.030 mmol, 1.1 equiv.) was added and the reaction mixture was stirred for 3 min. To the mixture, 40 µL (0.388 mmol, 14.2 equiv.) of benzyl alcohol was added. The Schlenk tube was taken out of the glovebox and heated at 110 °C. Heating caused rapid change of the solution into a suspension of dark brown solid and colorless supernatant. Small amount of the suspension was taken, the solvent was evaporated and the remaining solid was dissolved in DMSO-d_6 and $CDCl_3$ to check NMR spectroscopy. In both cases only peaks of benzyl alcohol were observed.

c. Attempted hydrogenation of benzyl benzoate

In a glove box, 10.4 mg (0.0274 mmol – 1.4 mol%) of **1** and 1.7 mg (0.028 mmol – 1.4 mol%) of KO^{t}Bu were mixed in 5 mL of toluene. The mixture was allowed to stir for 3 min, and 190 µL benzyl benzoate (190 µL, 1.00 mmol) was added. The reaction mixture was transferred into a 50 mL autoclave, sealed and filled with 3.0 M Pa of H_2, then stirred for 24 hours with heating at 60 °C. After cooling down, the suspension was filtered, and the filtrate was injected to GC-MS. No evidence of benzyl alcohol formation was found.

d. Attempted hydrogenation of benzonitrile

In a glove box, 10.4 mg (0.0274 mmol – 1.4 mol%) of **1** and 1.7 mg (0.028 mmol – 1.4 mol%) of KO^{t}Bu were mixed in 5 mL of toluene. The mixture was allowed to stir for 3 min, and 101 µL benzyl benzoate (1 mmol) was added. The reaction mixture was transferred into a 50 mL autoclave, sealed and filled with 3.0 MPa of H_2, then stirred for 24 hours with heating at 60 °C. After cooling down, the suspension of dark brown solid in a colorless supernatant was filtered, and the supernatant was checked by GC-MS. Only benzonitrile was found and no hydrogenation products were present.

d. Attempted transfer hydrogenation

In a glovebox, 0.01 mmol (1 mol%) of complex **1-4** and 0.02 mmol (2 mol%) of KO^{t}Bu were added to 1 mL 2-propanol. The mixture was allowed to stir for 20 min, and then 1 mL of propan-2-ol containing 117 µL (1 mmol) of acetophenone was added to the mixture. The resulting mixture was transferred to an 11 mL screw-cap vial which was closed tightly and wrapped by electrical tape. The vial was taken outside the glovebox and heated at 60 °C for 24 h. The mixture was cooled down and analyzed by GC-MS, which was showed no signal of 1-phenylethan-2-ol formation.

4. X-ray determination details

The X-ray diffraction data for the single crystals **1**-**5**, **1b**, **2a** and, **3a** were collected on a Rigaku XtaLab PRO instrument (κ-goniometer) with a PILATUS3 R 200K hybrid pixel array detector using Mo *K*α (0.71073 Å) [for **1** and **3**] or Cu *K*α (1.54184 Å) [for **2**, **4**, **5**, **1b**, **2a**, and **3a**] radiation monochromated by means of multilayer optics. The performance mode of MicroMax^{TM}-003 microfocus sealed X-ray tube was 50 kV, 0.60 mA. The diffractometer was equipped with a Rigaku GN2 system for low temperature experiments. Suitable crystals of appropriate dimensions were mounted on MiTeGen loops in random orientations. Preliminary unit cell parameters were determined with three sets of a total of 10 narrow frame scans in the case of a Mo-source and six sets of a total of 10 narrow frame scans at two different 2θ positions in the case of a Cu-source. The data were collected according to recommended strategies in an ω scan mode. Final cell constants were determined by global refinement of reflections from the complete data sets using the Lattice wizard module. Images were indexed and integrated with "smart" background evaluation using the *CrysAlisPro* data reduction package (Rigaku Oxford Diffraction). Analysis of the integrated data did not show any decay. The data were corrected for systematic errors and absorption using the *ABSPACK* module: Numerical absorption correction based on Gaussian integration over a multifaceted crystal model and empirical absorption correction based on spherical harmonics according to the point group symmetry using equivalent reflections. The *GRAL* module and the *ASSIGN SPACEGROUP* routine of the *WinGX* suite were used for analysis of systematic absences and space group determination.

The structures were solved by intrinsic phasing approach using *SHELXT*-2018/2[1] and refined by the full-matrix least-squares on F^2 using *SHELXL*-2018/3,[2] which uses a model of atomic scattering based on spherical atoms. Calculations were mainly performed using the *WinGX*-2021.3 suite of programs.[3] Non-hydrogen atoms were refined anisotropically. The positions of the hydrogen atom [O]H1 of methanol in the crystal of **3**, the hydrogen atom [Ru]H1 in **4**, the hydrogen atoms [C]H17A, [C]H17B, [C]H21A, and [C]H21B of doubly dearomatized complex **1b**, and the hydrogen atoms [C]H21 of mono-deprotonated complex **2a** were determined by difference Fourier maps, and these atoms were refined isotropically. The positions of hydrogen atoms of methyl groups were found using rotating group refinement with idealized tetrahedral angles. The other hydrogen atoms were inserted at the calculated positions and refined as riding atoms. The disorder, if present, was resolved using free variables and reasonable restraints on geometry and anisotropic displacement parameters. **4** was refined as a 2-component twin against a combined set of diffraction indices (HKLF 5): The second component with a contribution of 0.217(1) rotated by 179.9408° around [–0.00 0.00 1.00] (reciprocal) or [–0.25 -0.40 0.88] (direct). The unit cell of **2** contains highly disordered solvent molecules of diethyl ether and dichloromethane, which were treated as a diffuse contribution to the

overall scattering without specific atom positions by PLATON/SQUEEZE-30118.[4] The unit cell of **5** contains highly disordered solvent molecules of hexane and/or toluene, which were treated as a diffuse contribution to the overall scattering without specific atom positions by PLATON/SQUEEZE-230318. Squeezed solvent info is not included in the formulae and related items such as molecular weights and calculated densities. The compounds studied have no unusual bond lengths and angles.

Deposition numbers CCDC 2183590 (**1**), 2183591 (**2**), 2183592 (**3**), 2183593 (**4**), 2183594 (**1b**), 2183595 (**2a**), 2183596 (**3a**), and 2183597 (**5**) contain the supplementary crystallographic data for this paper. These data are provided free of charge by the joint Cambridge Crystallographic Data Centre and Fachinformationszentrum Karlsruhe Access Structures service www.ccdc.cam.ac.uk/structures.

Crystallographic data for **1**.

$C_{20}H_{20}F_6N_4O_6RuS_4$, yellow prism (0.099 × 0.078 × 0.069 mm^3), formula weight 755.71 g mol^{-1}; monoclinic, $P2_1/n$ (No. 14), a = 11.1327(11) Å, b = 22.4258(17) Å, c = 11.9189(12) Å, β = 113.247(12)°, V = 2734.1(5) Å^3, Z = 4, Z' = 1, T = 93(2) K, d_{calc} = 1.836 g cm^{-3}, μ(Mo $K\alpha$) = 0.965 mm^{-1}, $F(000)$ = 1512; $T_{max/min}$ = 1.000/0.809; 40887 reflections were collected (2.600° ≤ θ ≤ 27.100°, index ranges: –14 ≤ h ≤ 14, –28 ≤ k ≤ 28 and –15 ≤ l ≤ 15), 6002 of which were unique, R_{int} = 0.1142, R_σ = 0.0552; completeness to θ of 27.100° 99.5 %. The refinement of 372 parameters with no restraints converged to $R1$ = 0.0654 and $wR2$ = 0.1575 for 5114 reflections with $I > 2\sigma(I)$ and $R1$ = 0.0718 and $wR2$ = 0.1611 for all data with goodness-of-fit S = 1.034 and residual electron density $\rho_{max/min}$ = 2.484 and –1.585 e Å^{-3}, rms 0.202; max shift/e.s.d. in the last cycle 0.000.

Crystallographic data for **2**.

The unit cell contains highly disordered solvent molecules of diethyl ether and dichloromethane, which were treated as a diffuse contribution to the overall scattering without specific atom positions by PLATON/SQUEEZE. Squeezed solvent info is not included in the formulae and related items such as molecular weights and calculated densities. $C_{32.50}H_{30}Cl_3N_2PRuS_2$, yellow needle (0.210 × 0.036 × 0.030 mm^3), formula weight 751.09 g mol^{-1}; monoclinic, $P2_1/n$ (No. 14), a = 9.24161(5) Å, b = 32.47117(13) Å, c = 23.43790(9) Å, β = 95.3008(4)°, V = 7003.30(6) Å^3, Z = 8, Z' = 2, T = 93(2) K, d_{calc} = 1.425 g cm^{-3}, μ(Cu $K\alpha$) = 7.462 mm^{-1}, $F(000)$ = 3048; $T_{max/min}$ = 1.000/0.306; 134446 reflections were collected (2.331° ≤ θ ≤ 68.249°, index ranges: –10 ≤ h ≤ 11, –39 ≤ k ≤ 39 and –28 ≤ l ≤ 28), 12815 of which were unique, R_{int} = 0.0515, R_σ = 0.0211; completeness to θ of 68.249° 100.0 %. The refinement of 786 parameters with 79 restraints converged to $R1$ = 0.0361 and $wR2$ = 0.1007 for 12037 reflections with $I > 2\sigma(I)$ and $R1$ = 0.0381 and $wR2$ = 0.1028 for all data with goodness-of-fit S = 1.041 and residual electron density $\rho_{max/min}$ = 0.816 and –1.494 e Å^{-3}, rms 0.089; max shift/e.s.d. in the last cycle 0.002.

Crystallographic data for **3**.

$C_{17}H_{24}Cl_2N_2O_2RuS_3$, yellow plate (0.319 × 0.143 × 0.060 mm^3), formula weight 556.53 g mol^{-1}; monoclinic, $P2_1/c$ (No. 14), a = 13.2578(2) Å, b = 15.5195(2) Å, c = 10.17680(16) Å, β = 93.6059(14)°, V = 2089.77(6) Å^3, Z = 4, Z' = 1, T = 95(2) K, d_{calc} = 1.769 g cm^{-3}, μ(Mo $K\alpha$) = 1.322 mm^{-1}, F(000) = 1128; $T_{max/min}$ = 1.000/0.457; 65478 reflections were collected (2.397° ≤ θ ≤ 32.266°, index ranges: –18 ≤ h ≤ 19, –22 ≤ k ≤ 22 and –15 ≤ l ≤ 14), 7041 of which were unique, R_{int} = 0.0444, R_σ = 0.0223; completeness to θ of 32.266° 94.8 %. The refinement of 251 parameters with no restraints converged to $R1$ = 0.0198 and $wR2$ = 0.0476 for 6445 reflections with $I > 2\sigma(I)$ and $R1$ = 0.0231 and $wR2$ = 0.0486 for all data with goodness-of-fit S = 1.039 and residual electron density $\rho_{max/min}$ = 0.766 and –0.740 e Å^{-3}, rms 0.076; max shift/e.s.d. in the last cycle 0.001.

Crystallographic data for **4**.

The investigated crystal of **4** demonstrated non-merohedral twinning. $C_{34}H_{32}Cl_3N_2OPRuS_2$, yellow plank (0.148 × 0.063 × 0.047 mm^3), formula weight 787.12 g mol^{-1}; triclinic, $P\overline{1}$ (No. 2), a = 9.26627(12) Å, b = 10.6232(2) Å, c = 17.6628(3) Å, α = 73.7661(17)°, β = 81.0311(14)°, γ = 88.0351(13)°, V = 1648.87(5) Å^3, Z = 2, Z' = 1, T = 95(2) K, d_{calc} = 1.585 g cm^{-3}, μ(Cu $K\alpha$) = 7.977 mm^{-1}, F(000) = 800; $T_{max/min}$ = 1.00000/0.68185; 12222 reflections were collected (2.636° ≤ θ ≤ 74.485°, index ranges: –11 ≤ h ≤ 11, –13 ≤ k ≤ 13 and –22 ≤ l ≤ 22), 12222 of which were unique, R_σ = 0.0209; completeness to θ of 74.485° 99.3 %. The refinement of 402 parameters with 1 restraint converged to $R1$ = 0.0760 and $wR2$ = 0.2167 for 11594 reflections with $I > 2\sigma(I)$ and $R1$ = 0.0780 and $wR2$ = 0.2211 for all data with goodness-of-fit S = 1.079 and residual electron density $\rho_{max/min}$ = 2.212 and –1.949 e Å^{-3}, rms 0.171; max shift/e.s.d. in the last cycle 0.001.

Crystallographic data for **1b**.

$C_{25}H_{26}N_4RuS_2$, orange plate (0.137 × 0.104 × 0.025 mm^3), formula weight 547.69 g mol^{-1}; monoclinic, $P2_1/c$ (No. 14), a = 14.10525(5) Å, b = 15.03284(6) Å, c = 23.47074(8) Å, β = 104.0386(4)°, V = 4828.14(3) Å^3, Z = 8, Z' = 2, T = 98(2) K, d_{calc} = 1.507 g cm^{-3}, μ(Cu $K\alpha$) = 7.025 mm^{-1}, F(000) = 2240; $T_{max/min}$ = 1.000/0.500; 108602 reflections were collected (3.230° ≤ θ ≤ 71.100°, index ranges: –17 ≤ h ≤ 17, –18 ≤ k ≤ 18 and –28 ≤ l ≤ 28), 9360 of which were unique, R_{int} = 0.0608, R_σ = 0.0217; completeness to θ of 71.100° 100.0 %. The refinement of 730 parameters with 766 restraints converged to $R1$ = 0.0324 and $wR2$ = 0.0924 for 9076 reflections with $I > 2\sigma(I)$ and $R1$ = 0.0330 and $wR2$ = 0.0930 for all data with goodness-of-fit S = 1.030 and residual electron density $\rho_{max/min}$ = 0.792 and –0.867 e Å^{-3}, rms 0.097; max shift/e.s.d. in the last cycle 0.004.

Crystallographic data for **2a**.

$C_{41}H_{37}ClN_2PRuS_2$, orange prism (0.124 × 0.041 × 0.031 mm^3), formula weight 789.33 g mol^{-1}; monoclinic, $P2_1/n$ (No. 14), a = 13.28954(11) Å, b = 8.79277(9) Å, c = 30.6796(3) Å, β = 95.1615(9)°, V = 3570.43(6) Å^3, Z = 4, Z' = 1, T = 94(2) K, d_{calc} = 1.468 g cm^{-3}, μ(Cu $K\alpha$) = 6.007 mm^{-1}, F(000)

= 1620; $T_{max/min}$ = 1.000/0.667; 31467 reflections were collected (3.518° ≤ θ ≤ 72.123°, index ranges: –16 ≤ *h* ≤ 16, –10 ≤ *k* ≤ 9 and –34 ≤ *l* ≤ 37), 6974 of which were unique, R_{int} = 0.0384, R_σ = 0.0320; completeness to θ of 72.123° 99.0 %. The refinement of 437 parameters with 11 restraints converged to *R*1 = 0.0332 and *wR*2 = 0.0834 for 6254 reflections with $I > 2\sigma(I)$ and *R*1 = 0.0376 and *wR*2 = 0.0857 for all data with goodness-of-fit *S* = 1.081 and residual electron density $\rho_{max/min}$ = 0.947 and –0.728 e Å^{-3}, rms 0.075; max shift/e.s.d. in the last cycle 0.004.

Crystallographic data for **3a**.

$C_{16}H_{19}ClN_2ORuS_3$, orange plate (0.209 × 0.031 × 0.022 mm^3), formula weight 488.03 g mol^{-1}; monoclinic, $P2_1/c$ (No. 14), *a* = 13.5064(3) Å, *b* = 14.3080(3) Å, *c* = 9.18732(16) Å, β = 91.3511(18)°, *V* = 1774.95(6) Å^3, *Z* = 4, *Z*' = 1, *T* = 95(2) K, d_{calc} = 1.826 g cm^{-3}, μ(Cu *K*α) = 11.888 mm^{-1}, *F*(000) = 984; $T_{max/min}$ = 1.000/0.229; 14005 reflections were collected (4.503° ≤ θ ≤ 68.245°, index ranges: –16 ≤ *h* ≤ 15, –14 ≤ *k* ≤ 17 and –11 ≤ *l* ≤ 11), 3205 of which were unique, R_{int} = 0.0612, R_σ = 0.0419; completeness to θ of 68.245° 98.6 %. The refinement of 258 parameters with 167 restraints converged to *R*1 = 0.0761 and *wR*2 = 0.2110 for 2771 reflections with $I > 2\sigma(I)$ and *R*1 = 0.0830 and *wR*2 = 0.2177 for all data with goodness-of-fit *S* = 1.081 and residual electron density $\rho_{max/min}$ = 2.569 and –0.839 e Å^{-3}, rms 0.209; max shift/e.s.d. in the last cycle 0.000.

Crystallographic data for **5**.

The unit cell contains highly disordered solvent molecules of hexane and/or toluene, which were treated as a diffuse contribution to the overall scattering without specific atom positions by PLATON/SQUEEZE. Squeezed solvent info is not included in the formulae and related items such as molecular weights and calculated densities. $C_{64}H_{54}N_4P_2Ru_2S_4$, dark red plate (0.176 × 0.035 × 0.016 mm^3), formula weight 1271.43 g mol^{-1}; trigonal, $R\bar{3}$ (No. 148), *a* = 34.2817(3) Å, *c* = 13.16739(12) Å, *V* = 13401.6(2) Å^3, *Z* = 9, *Z*' = 0.5, *T* = 94(2) K, d_{calc} = 1.418 g cm^{-3}, μ(Cu *K*α) = 6.254 mm^{-1}, *F*(000) = 5832; $T_{max/min}$ = 1.000/0.376; 42303 reflections were collected (3.672° ≤ θ ≤ 67.731°, index ranges: –41 ≤ *h* ≤ 41, –39 ≤ *k* ≤ 41 and –15 ≤ *l* ≤ 15), 5382 of which were unique, R_{int} = 0.0496, R_σ = 0.0227; completeness to θ of 67.731° 99.9 %. The refinement of 508 parameters with 673 restraints converged to *R*1 = 0.0475 and *wR*2 = 0.1275 for 4783 reflections with $I > 2\sigma(I)$ and *R*1 = 0.0519 and *wR*2 = 0.1336 for all data with goodness-of-fit *S* = 1.046 and residual electron density $\rho_{max/min}$ = 0.997 and –0.547 e Å^{-3}, rms 0.109; max shift/e.s.d. in the last cycle 0.002.

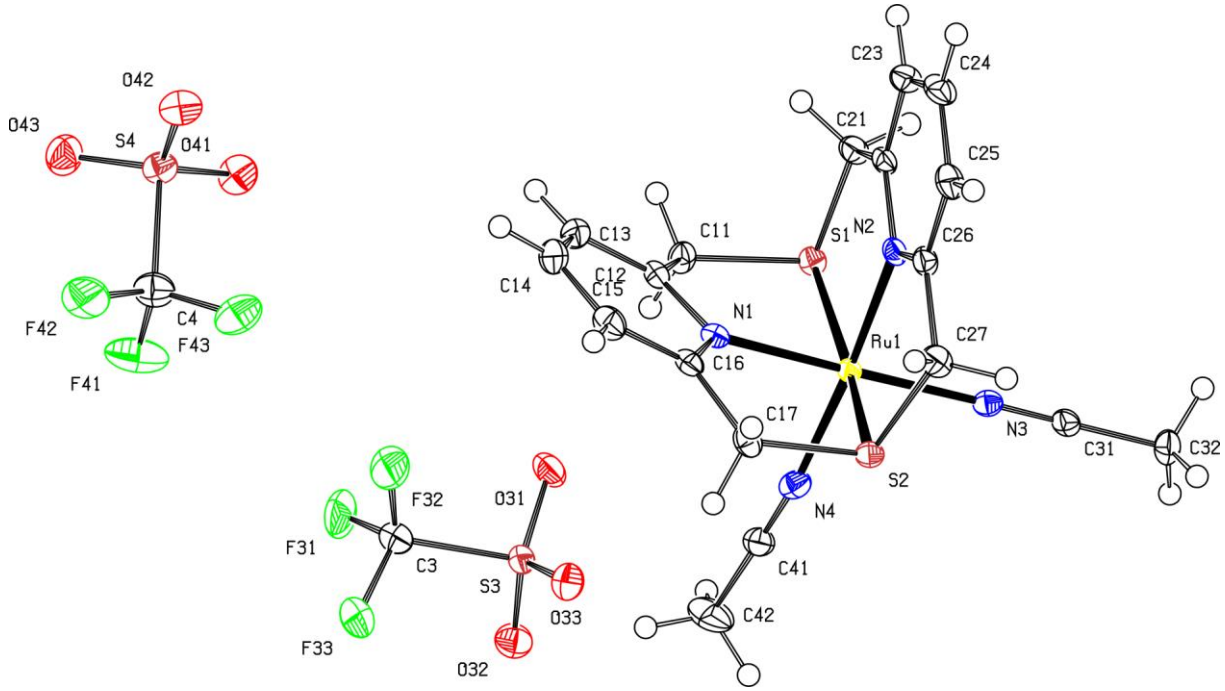

Figure S74. ORTEP at 50 % probability anisotropic displacement ellipsoids of non-hydrogen atoms for compound **1** according to SC-XRD.

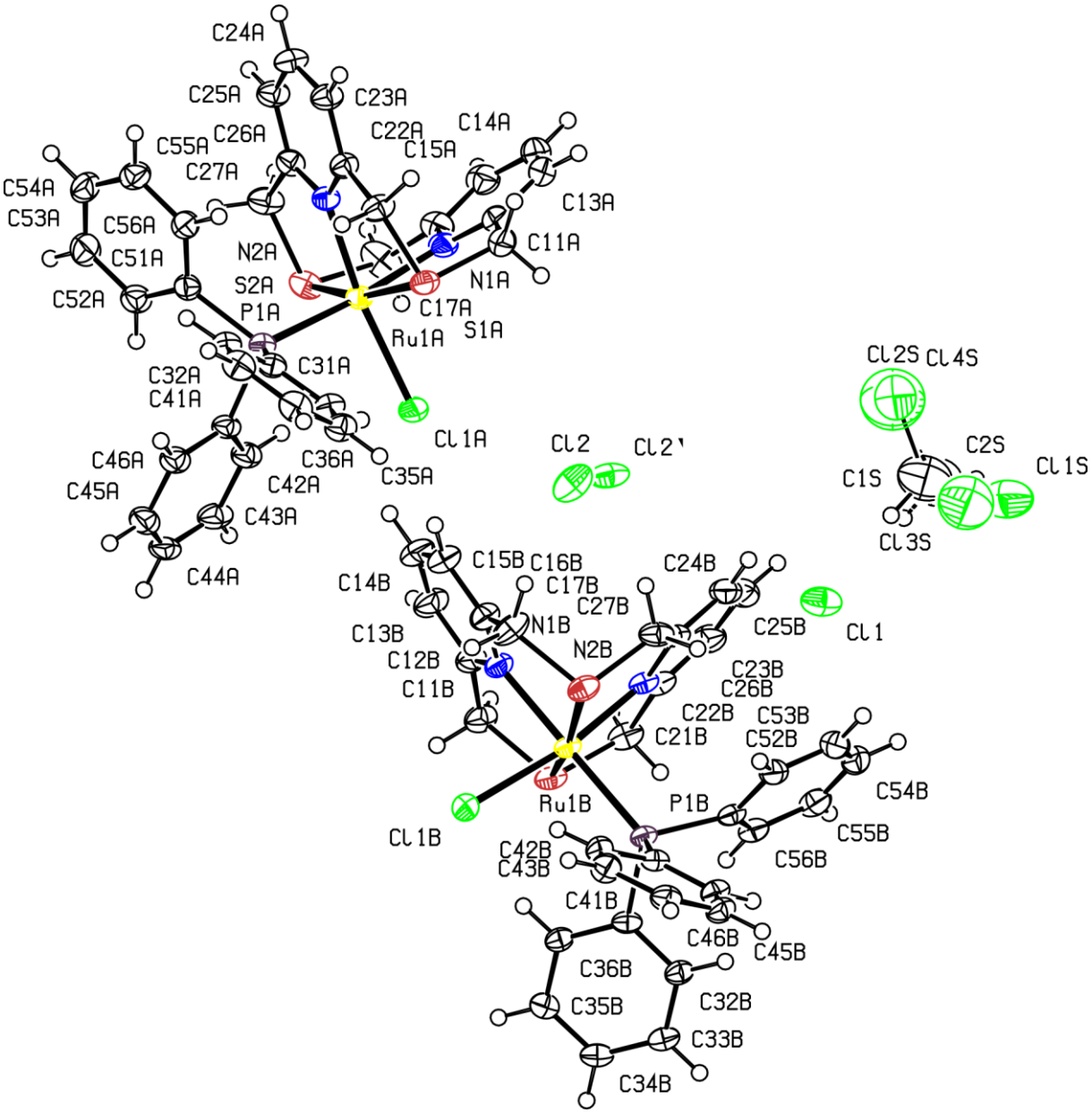

Figure S75. ORTEP at 50 % probability anisotropic displacement ellipsoids of non-hydrogen atoms for compound **2** according to SC-XRD. The minor disorder component is shown by dashed lines.

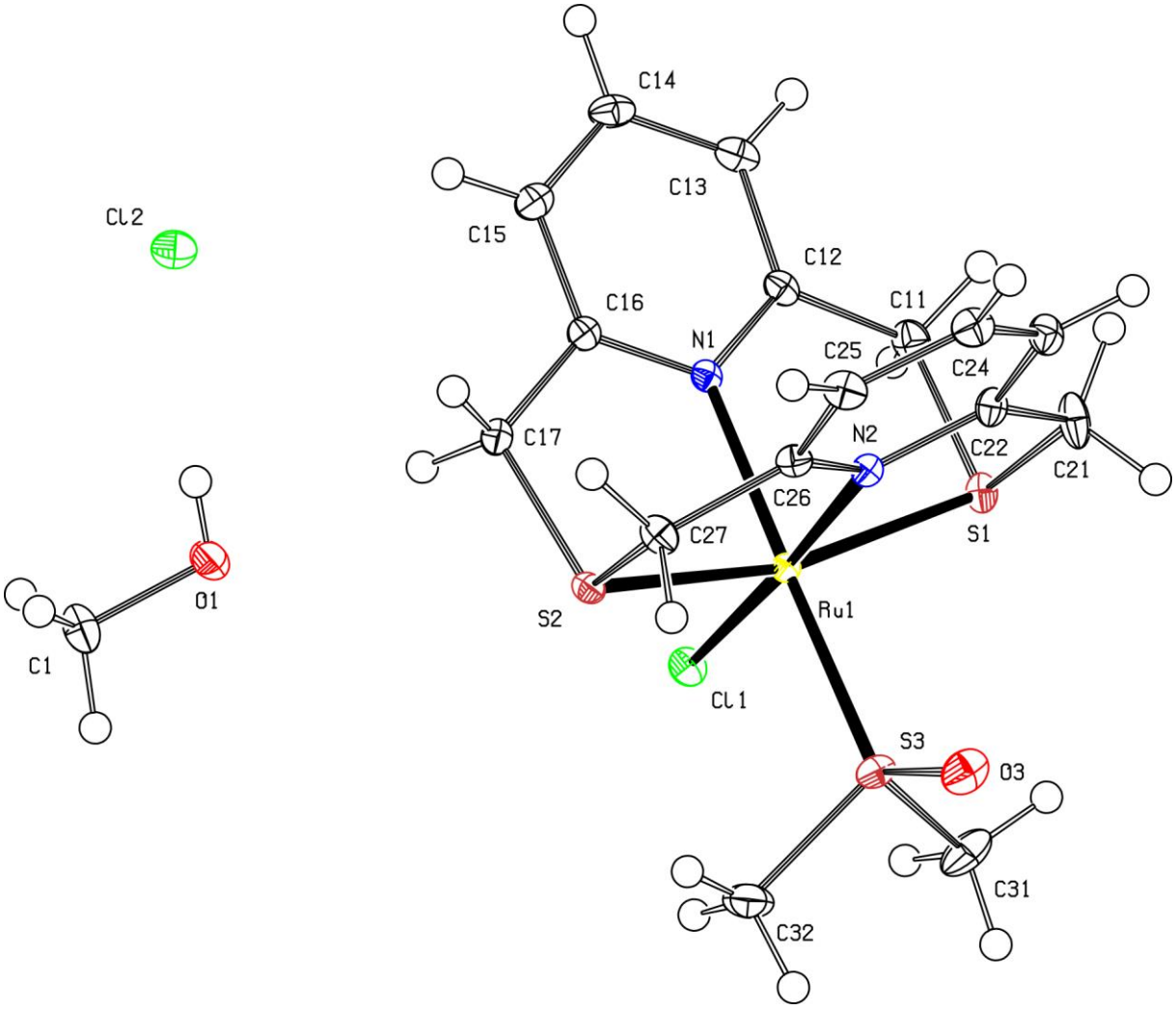

Figure S76. ORTEP at 50 % probability anisotropic displacement ellipsoids of non-hydrogen atoms for compound **3** according to SC-XRD.

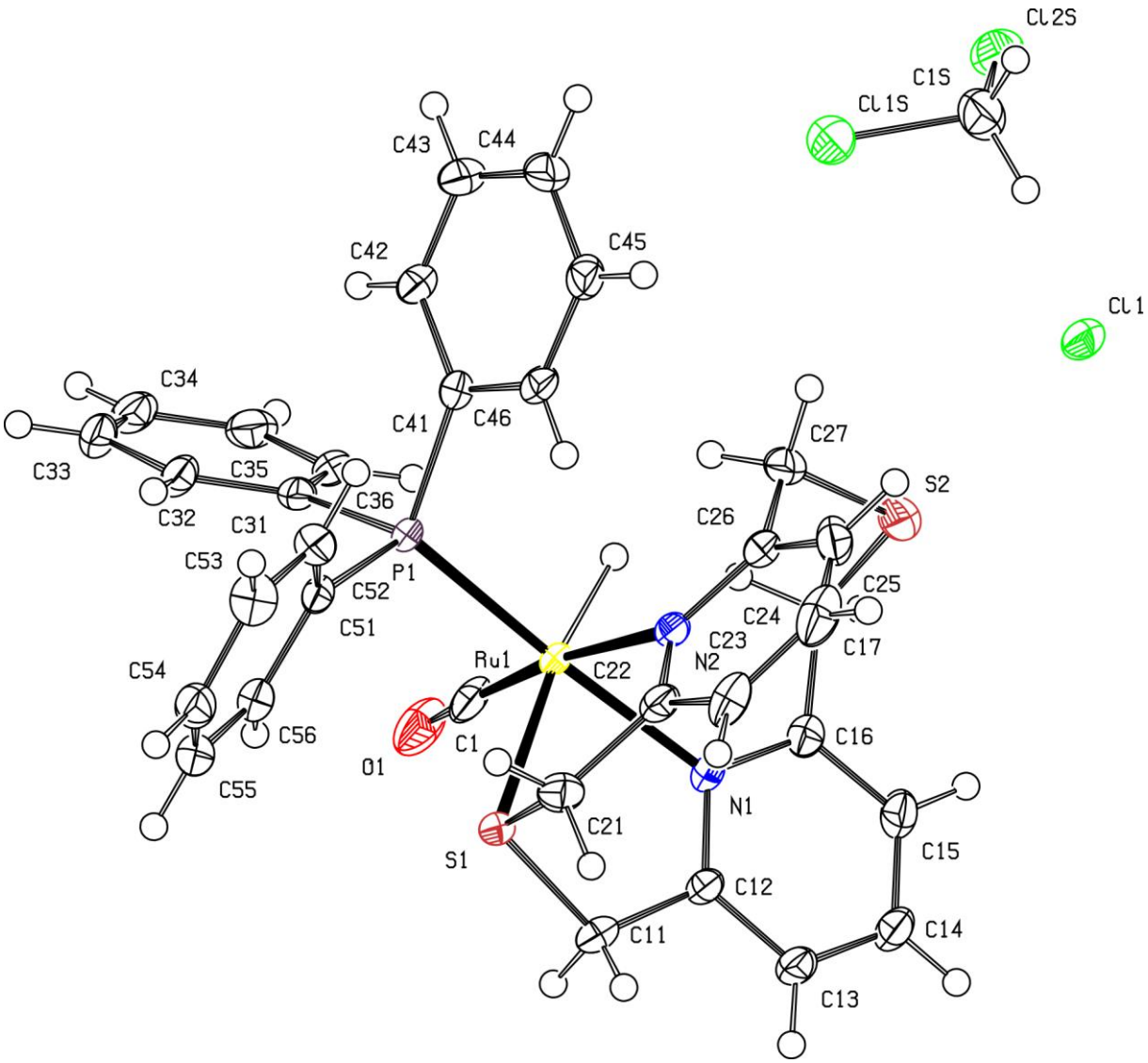

Figure S77. ORTEP at 50 % probability anisotropic displacement ellipsoids of non-hydrogen atoms for compound **4** according to SC-XRD.

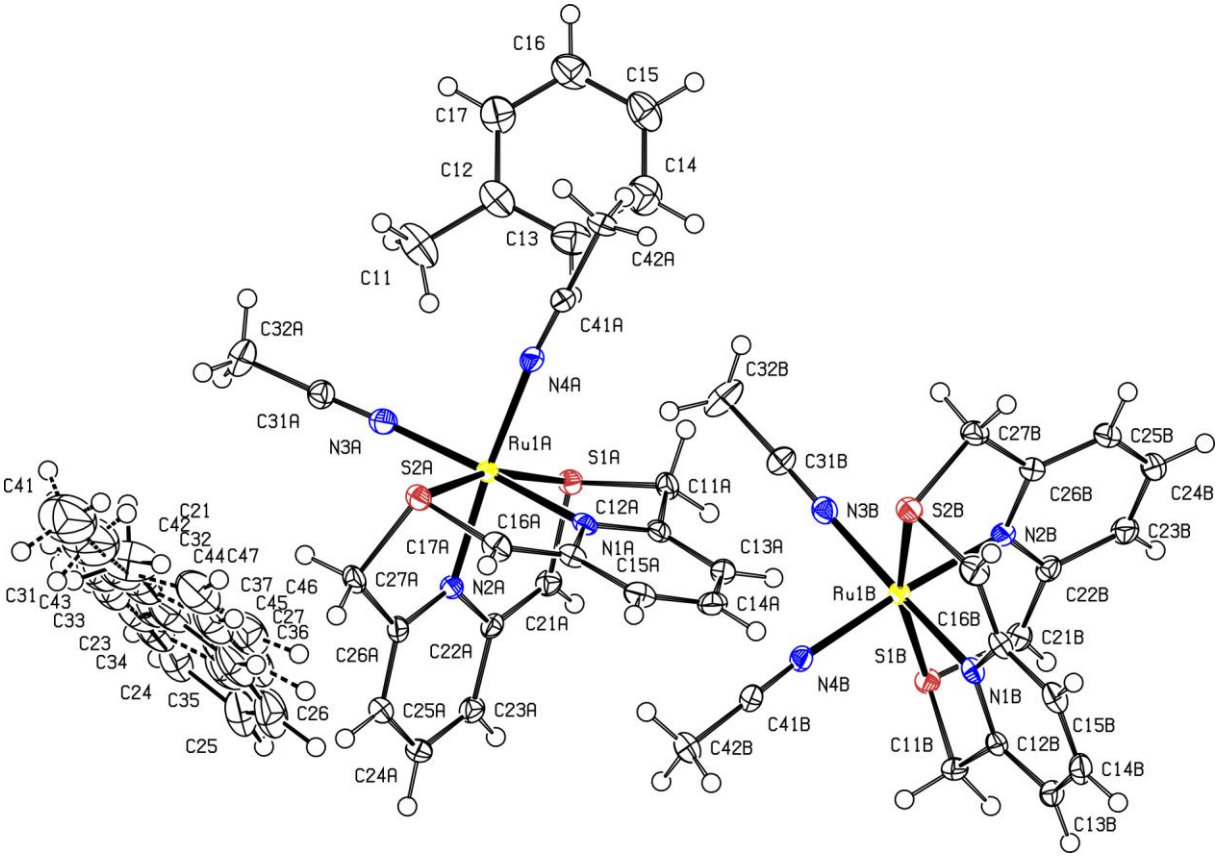

Figure S78. ORTEP at 50 % probability anisotropic displacement ellipsoids of non-hydrogen atoms for compound **1b** according to SC-XRD. The minor disorder component is shown by dashed lines.

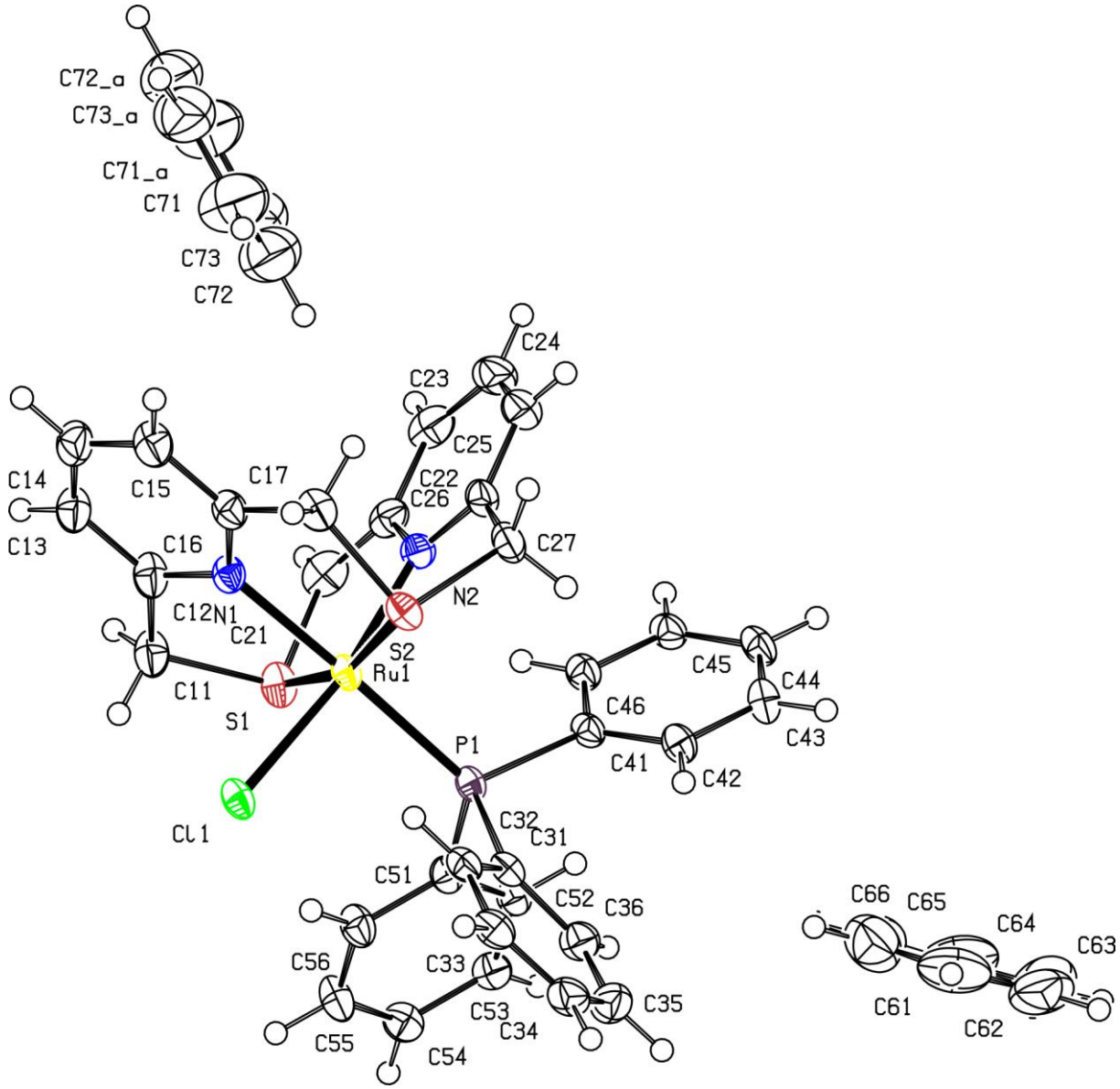

Figure S79. ORTEP at 50 % probability anisotropic displacement ellipsoids of non-hydrogen atoms for compound **2a** according to SC-XRD.

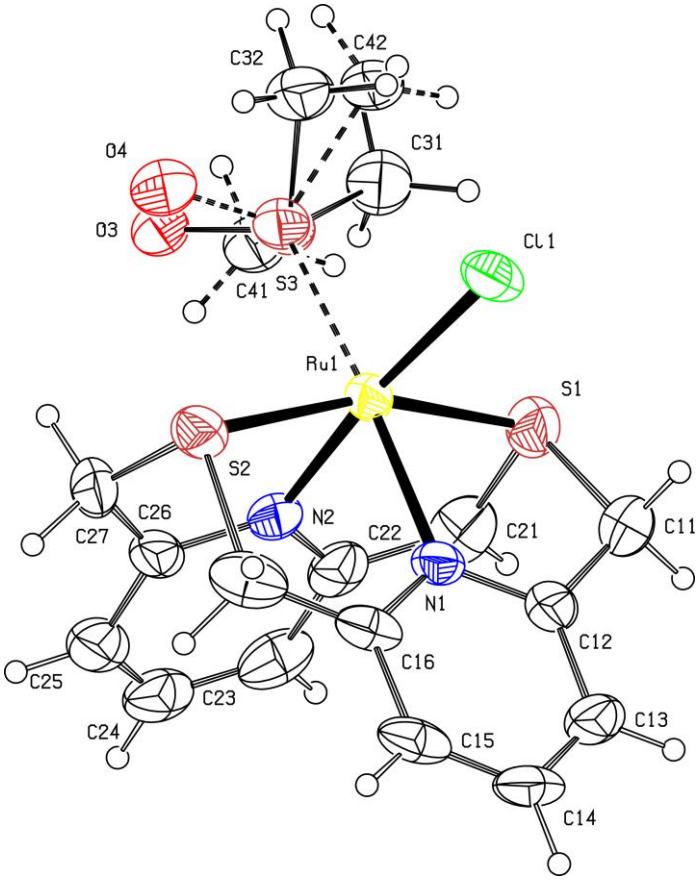

Figure S80. ORTEP at 30 % probability anisotropic displacement ellipsoids of non-hydrogen atoms for compound **3a** according to SC-XRD. The minor disorder component is shown by dashed lines.

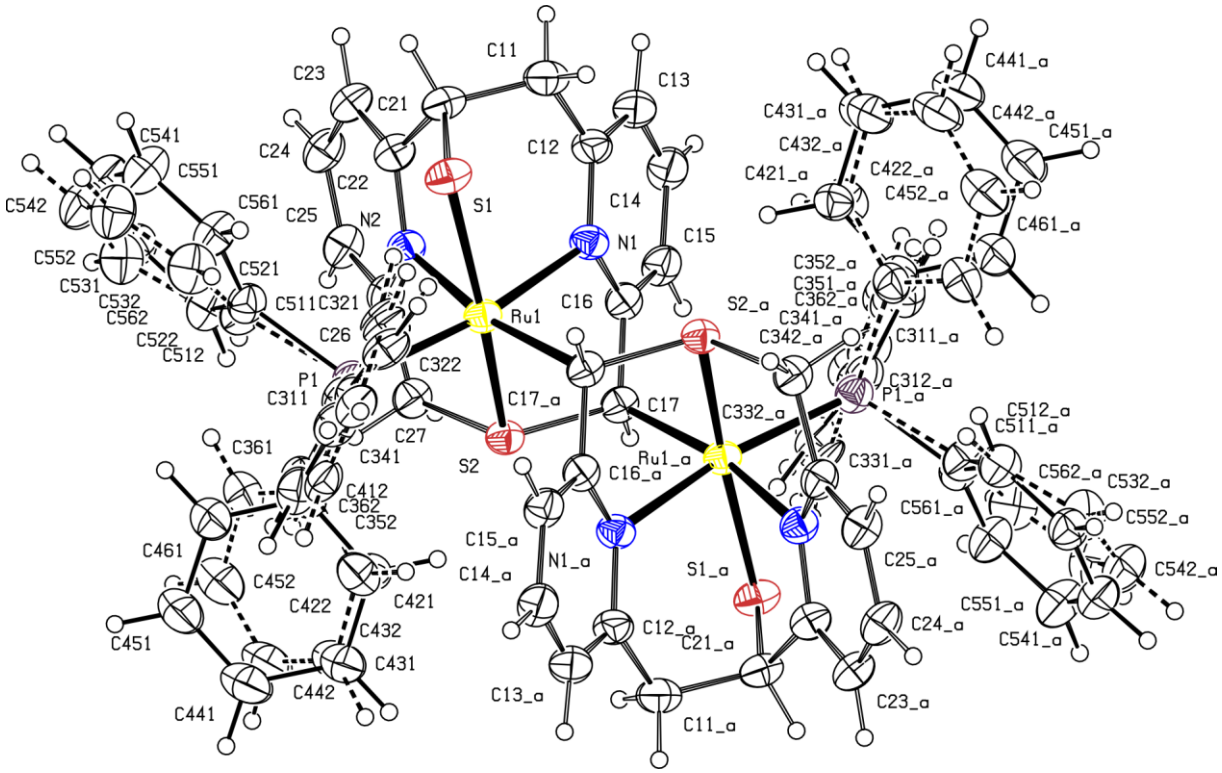

Figure S81. ORTEP at 30 % probability anisotropic displacement ellipsoids of non-hydrogen atoms for compound **5** according to SC-XRD. The minor disorder component is shown by dashed lines.

5. Computational details

For comparison of the relative stability of several isomers of complex **4a**, a combination of several different functional and basis sets was used, in the gas phase or taking into account solvent effect via SMD model.[5] In cases, similar trends and relative values were obtained (Table S2).

Table S2. Relative Gibbs free energies for isomers of **4a**, kcal mol^{-1}.

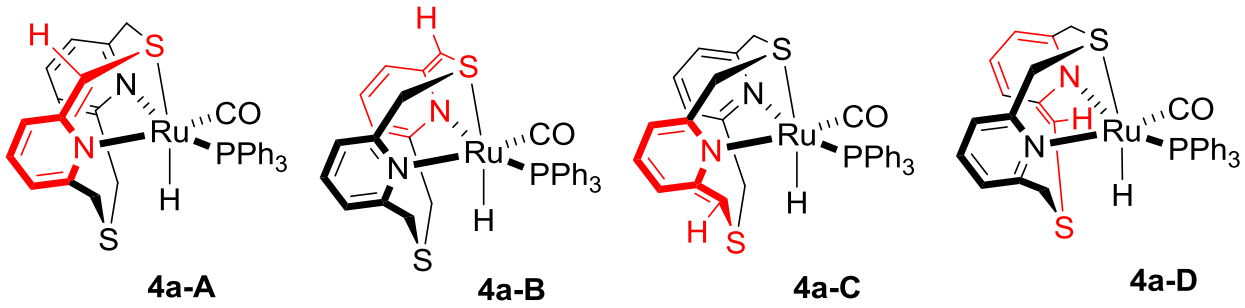

Functional	Basis set	Solvent	**4a-A**	**4a-B**	**4a-C**	**4a-D**
M06[6]	SDD(Ru)[7], 6-311g(d,p) (other elements)[8-13]	Gas phase	0	2.64	22.4	23.0
M06[6]	SDD(Ru)[7], 6-311+g(d,p) (other elements)[9, 11, 14-19]	Gas phase	0	2.33	22.3	22.9
M06[6]	SDD(Ru)[7], 6-311+g(d,p) (other elements)[9, 11, 14-19]	SMD, benzene	0	1.78	20.8	20.5
M06L[20]	SDD(Ru)[7], 6-311+g(d,p) (other elements)[9, 11, 14-19]	SMD, benzene	0	1.65	19.0	19.2
M06L[20]	def2tzvp[21]	SMD, benzene	0	1.89	19.3	20.4
ωB97XD[22]	SDD(Ru)[7], 6-311+g(d,p) (other elements)[9, 11, 14-19]	SMD, benzene	0	0.90	22.0	21.7

Table S3. The comparison of selected bond distances in the geometry-optimized structures (in gas phase) and SC-XRD parameters for **1b**.

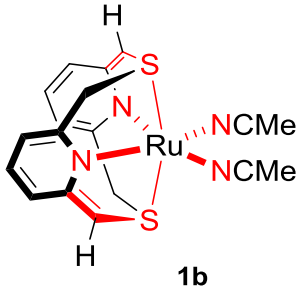

1b

	Bond distance (Å)				
Method:	Ru–S	Ru–N_{py}	Ru–$N_{(MeCN)}$	C_{py}=CH	CH–S
SC-XRD[a]	2.3441(5), 2.3280(5); 2.3414(5), 2.3282(5)	2.0416(18), 2.0425(17); 2.0412(18), 2.0474(18)	2.0473(19), 2.0461(19); 2.0512(19), 2.0435(18)	1.382(3), 1.387(3); 1.386(3), 1.388(3)	1.733(2), 1.730(2); 1.735(2), 1.731(2)
M06/6-311g(d,p),SDD(Ru)	2.38628	2.06672	2.03886; 2.03887	1.38519	1.73961
M06/6-311+g(d,p),SDD(Ru)	2.38584	2.06569	2.03834	1.38562	1.74095
M06L/6-311+g(d,p),SDD(Ru)	2.38989	2.07180	2.02964	1.39079	1.73094
M06L/def2tzvp	2.37000	2.06600	2.00996; 2.00995	1.38781	1.71598
ωB97XD/6-311+g(d,p),SDD(Ru)	2.37124	2.06608	2.05015	1.38510	1.73943

[a]For two symmetry independent molecules in the unit cell.

6. References

1. G. Sheldrick, *Acta Crystallogr., Sect. A*, 2015, **71**, 3-8.
2. G. Sheldrick, *Acta Crystallogr., Sect. C*, 2015, **71**, 3-8.
3. L. J. Farrugia, *J. Appl. Crystallogr.*, 2012, **45**, 849-854.
4. A. Spek, *Acta Crystallogr., Sect. C*, 2015, **71**, 9-18.
5. A. V. Marenich, C. J. Cramer and D. G. Truhlar, *J. Phys. Chem. B*, 2009, **113**, 6378-6396.
6. Y. Zhao and D. G. Truhlar, *Theor. Chem. Acc.*, 2008, **120**, 215-241.
7. D. Andrae, U. Häußermann, M. Dolg, H. Stoll and H. Preuß, *Theor. Chim. Acta*, 1990, **77**, 123-141.
8. B. P. Pritchard, D. Altarawy, B. Didier, T. D. Gibsom and T. L. Windus, *J. Chem. Inf. Model.*, 2019, **59**, 4814-4820.
9. D. Feller, *J. Comput. Chem.*, 1996, **17**, 1571-1586.
10. K. L. Schuchardt, B. T. Didier, T. Elsethagen, L. Sun, V. Gurumoorthi, J. Chase, J. Li and T. L. Windus, *J. Chem. Inf. Model.*, 2007, **47**, 1045-1052.
11. M. M. Francl, W. J. Pietro, W. J. Hehre, J. S. Binkley, M. S. Gordon, D. J. DeFrees and J. A. Pople, *J. Chem. Phys.*, 1982, **77**, 3654-3665.
12. R. Krishnan, J. S. Binkley, R. Seeger and J. A. Pople, *J. Chem. Phys.*, 1980, **72**, 650-654.
13. A. D. McLean and G. S. Chandler, *J. Chem. Phys.*, 1980, **72**, 5639-5648.
14. B. P. Pritchard, D. Altarawy, B. Didier, T. D. Gibsom and T. L. Windus, *J. Chem. Inf. Model.*, 2019, **59**, 4814-4820.
15. K. L. Schuchardt, B. T. Didier, T. Elsethagen, L. Sun, V. Gurumoorthi, J. Chase, J. Li and T. L. Windus, *J. Chem. Inf. Model.*, 2007, **47**, 1045-1052.
16. T. Clark, J. Chandrasekhar, G. W. Spitznagel and P. V. R. Schleyer, *J. Comput. Chem.*, 1983, **4**, 294-301.
17. R. Krishnan, J. S. Binkley, R. Seeger and J. A. Pople, *J. Chem. Phys.*, 1980, **72**, 650-654.
18. A. D. McLean and G. S. Chandler, *J. Chem. Phys.*, 1980, **72**, 5639-5648.
19. G. W. Spitznagel, T. Clark, P. v. R. Schleyer and W. J. Hehre, *J. Comput. Chem.*, 1987, **8**, 1109-1116.
20. Y. Zhao and D. G. Truhlar, *J. Chem. Phys.*, 2006, **125**, 194101.
21. F. Weigend and R. Ahlrichs, *Phys. Chem. Chem. Phys.*, 2005, **7**, 3297-3305.
22. J.-D. Chai and M. Head-Gordon, *Phys. Chem. Chem. Phys.*, 2008, **10**, 6615-6620.